Groundwater Chemistry Changes as a Result of CO_2 Injection at the ZERT Field Site in Bozeman, Montana

Project Report

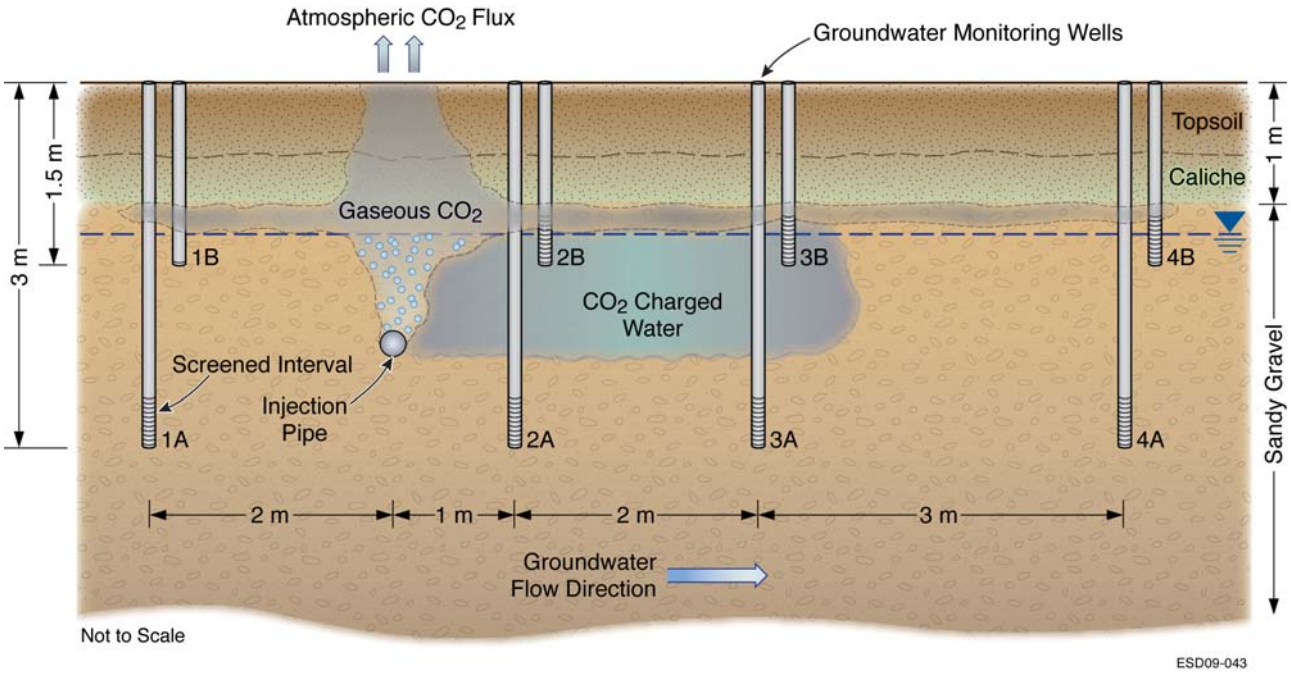

Contributors in Alphabetical Order:

Lawrence Berkeley National Laboratory:
John A. Apps, Jens T. Birkholzer, Nicolas Spycher, Liange Zheng

U.S. Geological Survey:
Gil Ambats, William N. Herkelrath, Yousif, K. Kharaka, James J. Thordsen, Evangelos Kakouros, Sarah Beers

Montana State University:
Kadie S. Gullickson, Lee H. Spangler

TABLE OF CONTENTS

List of Figures

List of Tables

1. INTRODUCTION

1.1. Understanding the Problem

Combustion of fossil fuels produces CO_2, a common greenhouse gas linked to global climate change. Separation of CO_2 from emissions produced by large industrial point sources like power plants, cement kilns and refineries, and injection deep underground into geologic formations is one method of preventing CO_2 releases into the atmosphere. This process is referred to as Carbon Capture and Storage (CCS). CCS is one of several solutions being considered to mitigate global climate change. Other solutions include increased energy efficiency, renewables, nuclear power, advanced coal, and plug-in hybrid electric vehicles.

Injection of CO_2 into deep geologic reservoirs is one solution, but this method of sequestering carbon is not without its own unique set of environmental risks, summarized by the United States Environmental Protection Agency (US EPA) in its draft rules governing underground injection of CO_2 (US EPA, 2008). The US EPA designates potable groundwater aquifers as those underground sources of drinking water (USDW) worthy of protection under the Safe Drinking Water Act (US EPA, 2004). Many municipalities, businesses, and private individuals across the United States rely on these USDW as their primary source of drinking water, or for process water used in manufacturing, power production, etc.

Compressed CO_2 (as a free phase liquid or supercritical fluid) is less dense than water under most conditions, causing it to float (like oil on water) and move upward if unconstrained by fine-grained, low permeability rocks or sediments (such as shale, mudstone, clay or salt). Therefore, if not properly capped (analogous to a soda bottle), CO_2 has the potential to leak from the storage formation where it was injected and move as a buoyant fluid into overlying USDW. Once CO_2 enters a USDW, it readily dissolves in the groundwater, forming a weak acid (i.e., carbonic acid), which lowers the pH of the groundwater and increases its dissolved carbonate content, according to the following overall reaction:

$$CO_{2(g)} + H_2O \Longrightarrow H^+ + HCO3^- \qquad (1\text{-}1)$$

The magnitude and extent of acidification and alkalinity increase is expected to depend on the degree of buffering by aquifer materials (such as carbonate minerals found in many aquifers) and could result in the release of trace metals by dissolution and/or desorption and ion exchange reactions. Both of these processes could mobilize heavy metals including lead (Pb), cadmium (Cd) and arsenic (As) into groundwater (e.g., Wang and Jaffe, 2004; Kharaka et al., 2006; Birkholzer et al., 2008; Kharaka et al., 2009b). The solvent properties exhibited by supercritical CO_2 may also leach organic compounds including benzene, toluene, ethylbenzene and xylenes (BTEX), phenols, polynuclear aromatic hydrocarbons (PAHs) and other compounds, from organic matter present in the aquifer. The release of these constituents at levels exceeding US EPA maximum contaminant levels (MCL) could become a potential health hazard. Therefore, even though the risk of CO_2 migration from the storage reservoir is considered to be small with proper site selection and a regulatory framework designed to oversee, monitor and control risk (IPCC, 2007), the potential impact the CO_2 can have on potable groundwater resources warrants further study.

1.2. Scope and Objective

In this report, we describe the geochemical and hydrological results of a shallow CO_2-injection test performed during July and August 2008 at a field site created by the Zero Emission Research and Technology Center (ZERT), located on Montana State University (MSU) property near Bozeman, Montana. From July 9 to August 7, 2008, approximately 300 kg/day of food-grade CO_2 was injected through a perforated pipe placed approximately 1.1–2.5 m below ground surface, and about 0.5–1 m below the water table. The objective of this study was to investigate, using a small-scale field experiment, whether sequestered CO_2 released from a hypothetical geologic storage reservoir would have an adverse impact on USDW. The objective was accomplished by collecting approximately 80 shallow groundwater samples before, during, and after CO_2 gas injection and analyzing these samples for their concentrations of major, minor, and trace inorganic and organic compounds. The scope of the study was limited to the potential impact of gaseous CO_2 on potable groundwater and did not consider or evaluate the impact of displaced saline groundwater on shallow freshwater aquifers. The study was undertaken as a collaborative project between the Earth Sciences Division at Lawrence Berkeley National Laboratory (LBNL) and the U.S. Geological Survey (USGS), in part funded by the Electronic Power Research Institute (EPRI).

2. DESCRIPTION OF THE ZERT FIELD SITE

ZERT was initially created as a collaboration involving two universities and six DOE national laboratories. ZERT started in 2006 to develop a field test site where controlled, shallow subsurface release of CO_2 would be possible over a significant spatial extent. The primary purpose of the ZERT field site, located on MSU property near Bozeman, Montana, was to allow controlled studies of near-surface CO_2 transport and detection technologies. A slotted horizontal well of about 70 m length divided into six zones was installed into the shallow subsurface (Figure 2.1). The average depth of the slotted section of the horizontal well is on average about 1.8 m below ground surface, varying from up to 2.5 m at the southwestern end (Zone V and VI) to 1.1 m at the northwestern end (Zone I). On average, the horizontal well is about 0.5–1 m below the water table (also see Section 5.1). The scale and CO_2 release rates were chosen to be representative of possible leakage rates from large-scale CO_2 storage projects. Controlled releases of CO_2 were performed in the summers of 2007 and 2008. A wide variety of detection techniques were deployed by various collaborators to determine the efficacy of monitoring strategies, and to better understand transport from the saturated zone to the vadose zone and ultimately to the atmosphere (Spangler et al., 2009). This report focuses primarily on the geochemical and hydrological results of shallow CO_2 injection into the groundwater at the ZERT site, based on the groundwater samples and other relevant data obtained in the 2008 release experiment (Kharaka et al., 2009a). Details on other aspects of the project can be found in Spangler et al. (2009).

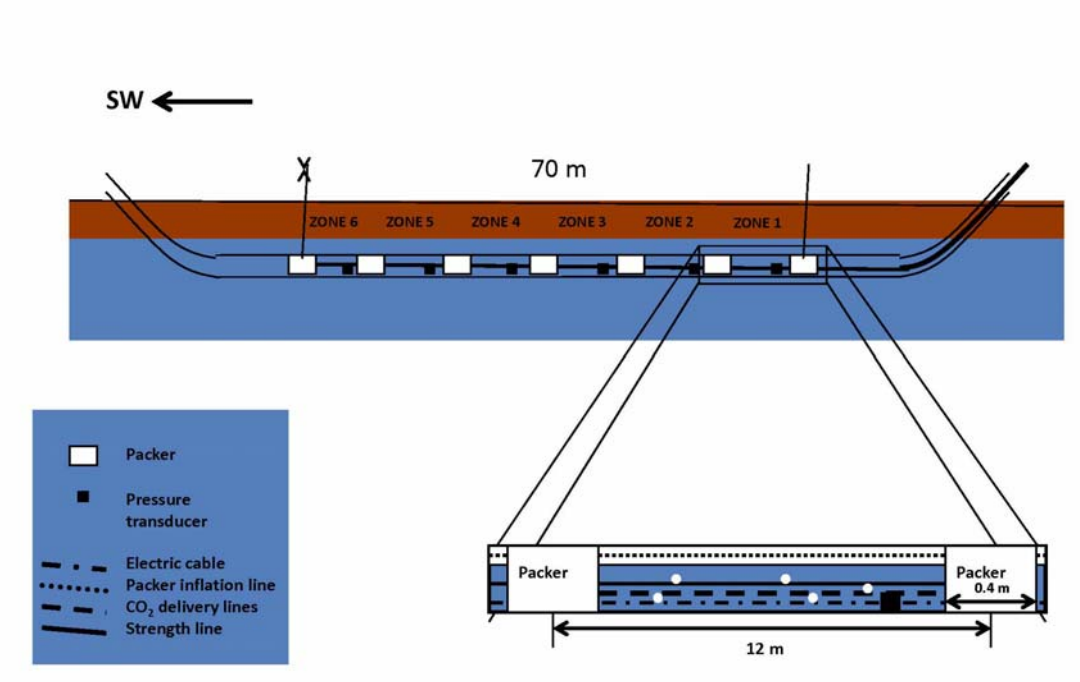

Figure 2.1. *Packer system installed in horizontal well (from Spangler et al., 2009).*

2.1. Regional and local setting

The ZERT field site is located on a relatively flat 12 hectare agricultural plot at the western edge of the MSU-Bozeman campus in Bozeman, Montana, USA (see Spangler et al., 2009, for description of regional setting, and the various investigations completed or currently ongoing at this site). Plant coverage is about 70% grasses with the remainder being alfalfa, clover, dandelion, and thistle.

The ZERT site is located at an elevation of 1,495 m near the southeastern boundary of the Gallatin Valley, which is a north-south-trending intermontane basin of about 1,350 km^2 in area (Kendy and Tresch, 1996). Structurally, the Gallatin Valley is an eastward tilted graben, a broad alluvial plain filled with up to 1,800 m of poorly consolidated Cenozoic sandy gravel deposits. At the ZERT site, about a meter of silts and clays with a top soil layer of variable thickness overlie the sandy gravel. Test pits and cores collected from several locations on the field consistently revealed two distinct soil zones. The topsoil of organic silt and clay with some sand ranges in thickness from 0.2 to 1.2 m. A caliche layer, high in calcite and clay, is observed at depths of ~50–80 cm, but only small traces of carbonate are observed in fines above 2.5 m and in megascopic detrital carbonate. Beneath the topsoil layer is a cohesionless deposit of sandy gravel extending to 5 m, the maximum depth investigated (Spangler et al., 2009). More information on core analysis and local mineralogy is given in Section 4.

2.2. Geology

The Gallatin Valley basement and surrounding mountains consist of complexly folded and faulted Tertiary through Archean bedrock.The eastern boundary of this valley is a series of steep normal faults along the fronts of the Bridger and Gallatin Ranges. The Gallatin Range, which borders the south margin and crests above 3,000 m elevation, provides source material to the basin-fill deposits in the portion of the Gallatin Valley which includes the ZERT field site.

The basin-fill deposits are subdivided by Kendy (2001) into three hydrogeologic units: Quaternary alluvium (Qal), Quaternary and Tertiary undifferentiated deposits (QTd), and Tertiary Bozeman group (Tb). The Tertiary Bozeman Group is considered to underlie the entire Gallatin Valley; it outcrops as pediments on the Madison Plateau and benches east of Bozeman, but it is mostly covered by a veneer of Quaternary and/or Tertiary alluvium. Quaternary and Tertiary undifferentiated deposits consists of unconsolidated Quaternary alluvial-fan deposits overlying Tertiary sedimentary pediments. Alluvial fan deposits extend into the Gallatin Valley from the Bridger and Gallatin Range fronts and consist of a heterogeneous mixture of unconsolidated poorly sorted rock fragments in a sand, silt and clay matrix with some carbonate cement (Kendy and Tresch, 1996; Lonn and English, 2002). The largest of these alluvial fans, extends northwards from the Gallatin Range front into the alluvial plain between Hyalite and Bozeman Creeks. The city of Bozeman and much of the surrounding land, including the ZERT field site, is located on this alluvial fan and is mapped, in Kendy (2001) as Quaternary and Tertiary undifferentiated deposit (Qtd).

The Gallatin Range provides the source material for the alluvial fan deposits in and around the ZERT site. The bedrock geology for the Gallatin Range is grouped by Kendy (2001) into four hydrogeologic units: (1) Tertiary (Eocene) volcanic rocks (Tv), which include andesite and basalt flows, breccia, agglomerate, and tuff of the Gallatin-Absaroka Volcanics; (2) Tertiary through Middle Proterozoic sedimentary bedrock (Tysaq), which include a number of sandstone and limestone formations, and the Middle Proterozoic Belt Supergroup. Sandstone, conglomerate, and limestone predominate the lithologies; (3) Cretaceous through Cambrian sedimentary bedrock (KCscu), in which fine-grained sandstone, shale, mudstone, siltstone, and chert predominate the lithologies; (4) Archean metamorphic rocks (Am), which consists of crystalline rocks, mainly biotite gneiss, with some schist, quartzite, and marble. Tertiary volcanic rocks (Tv) and Archean metamorphic rocks (Am) predominate in the Gallatin Range and appear to be the major rock lithologies in poorly to moderately sorted sand and gravel at the ZERT field site.

2.3. Test Configuration and Groundwater Flow

Five pairs of polyvinyl chloride (PVC) groundwater monitoring wells, 5 cm in diameter and extending to depths of about 1.5 m (B-wells) and about 3.0 m (A-wells) below ground surface, were installed in the summer of 2007. These were emplaced at the southwestern end of the slotted section of the horizontal CO_2 injection pipe (zone 6) to measure changes in the chemical composition of shallow groundwater and head-space gas, following CO_2 injection (Figure 2.2). The wells are screened at the bottom 0.76 cm, and are located at distances ranging from 1 to 6 m from the horizontal CO_2 injection well. Comparison of the elevation of the horizontal injection well in zone 6 with the screening depth of the groundwater wells reveals that the CO_2 injection occurs

approximately 0.26 to 0.33 m above the top of the screening interval in the deep A-wells, and about 0.50 to 0.60 m below the bottom of the screening interval in the shallow B-wells (see schematic in Figure 5.1).

The groundwater hydraulic gradient and flow direction were estimated to be 17 degrees west of north (Figure 2.2). Four of the monitoring well pairs were installed north of the horizontal injection well (2A/B, 3A/B, 4A/B, and 5A/B) in the downgradient groundwater flow direction; one pair (1A/B) was installed south or hydraulically upgradient (Figure 2.2) from the horizontal well. In December 2008, three additional monitoring wells were installed (W6, W7, and W8), primarily to obtain core for mineral characterization and laboratory experiments. Well W6 is 2.6 m deep with the bottom 0.76 m screened. Wells W7 and W8 are 3 m deep with the bottom 1.5 m screened. Four additional water wells in the area have been used to estimate groundwater flow gradients and direction (MW1 through MW4); however, these wells are too far away from the injection well to be affected by CO_2 injection.

The depth of the water table at the ZERT field site is close to the ground surface, but varies seasonally. Spangler et al. (2009) report a variation of about 1 m in the depth of the water table over the last two and a half years. In the summers of 2007 and 2008, the depth of the water table measured in the water monitoring wells in zone 6 ranged from approximately 1.35 m to slightly more than 1.5 below ground surface, indicating that the shallow wells were just deep enough to collect water samples. Percolation tests made in 2006 yielded hydraulic conductivity values approximately 0.76 and 1.4 m/day in the upper soil (sandy silt) layer and in the sand-gravel aquifer, respectively. Results of tracer tests conducted in 2009 showed the lateral groundwater flow is high at about 2 m/day, and higher than previously estimated (Spangler et al., 2009). Calculated rates of CO_2 diffusion and advection in the unsaturated zone are at least an order of magnitude higher than the groundwater flow rate (Lewicki et al., 2007; Lewicki et al., 2009). Also, analyses of gas samples obtained from the head space of the wells yielded $P(CO_2)$ values as high as 0.95 bar relatively rapidly (Strazisar, 2009; Strazisar et al., 2009). These data indicate that the rapid and systematic changes observed in the chemical composition of groundwater are likely driven by both fast spreading of gaseous CO_2 in the sand-gravel unsaturated zone under the upper soil layer, accompanied by re-dissolution into the groundwater, as well as by the transport of dissolved CO_2 in the groundwater (see also Section 5.1).

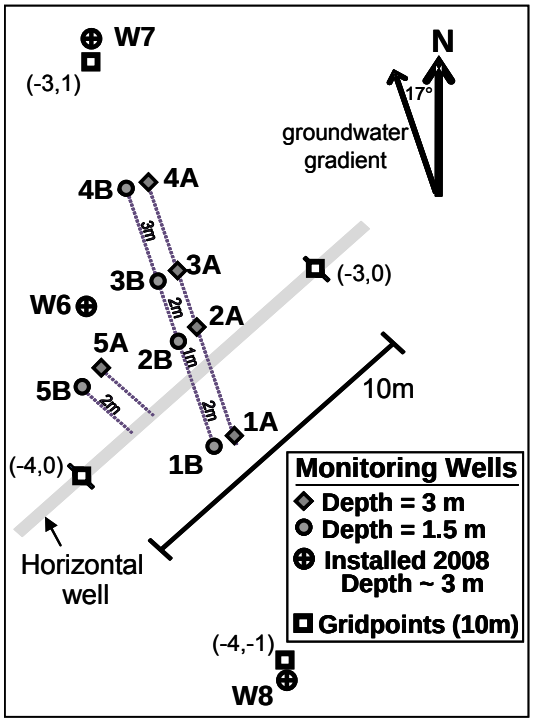

Figure 2.2. *Location of water monitoring wells in relation to the surface trace of the slotted horizontal CO_2 injection pipe in zone 6 of the ZERT site. The gridpoints in the figure refer to a grid with 10 m spacing that was established to provide a common reference system for researchers.*

2.4. Water Sampling and Analysis

Most of the water samples for this study were obtained from the shallow groundwater wells (1.5 m deep). The water from the deeper wells was not significantly impacted by the injected CO_2, likely because these are screened between 0.26 and 0.33 m below the level of the injection pipe. Sample collection, preservation, and field and laboratory chemical analyses of water and some relevant isotopes were carried out by methods described in Kharaka and Hanor (2007). Groundwater samples were collected using a peristaltic pump after purging the well by collecting 0.5–1 L aliquot that was used for rinsing the sampling containers. On-site chemical analyses of groundwater samples, carried out in a USGS mobile laboratory, included measurements of pH, Eh, conductivity, alkalinity, dissolved oxygen (DO) and temperature. Sample filtration, acidification, and preservation were also carried out in the USGS field laboratory. Groundwater samples for metal analysis were filtered using a 0.1 micron filter, then acidified using ultrex HNO_3 and kept in a refrigerator and shipped on ice to the USGS laboratory in Menlo Park, California.

Laboratory analyses for cations and metals were evaluated by comprehensive inductively coupled plasma mass spectrometry (ICP-MS), with focus on concentrations of various trace elements, including As, B, Cd, Cr, Cu, Fe, Hg, Mn, Pb, Se, U, and Zn. Sophisticated ICP-MS equipment was necessary because these elements of interest have very low background concentrations in the site groundwater, often close to the detection limits. Major and minor anions were determined in USGS laboratory by ion chromatography (IC). Benzene, toluene, ethyl-benzene, m-, p- and o-xylene (BTEX) were analyzed using an SRI-8610C gas chromatograph as described in EPA Method

5030C, a purge-and-trap procedure for the analysis of low levels of volatile organic compounds (VOCs) in aqueous samples and water miscible liquid samples. The gas chromatographic determinative steps are found in EPA methods 8015 and 8021 (US EPA, 2003).

3. WATER SAMPLING RESULTS

Detailed chemical analyses of over 60 groundwater samples collected from the ZERT wells in July–August 2008 have been completed. Most of the samples analyzed are from four of the five shallow 1.5 m deep "B" wells; results from Well 3B are incomplete because we were unable to obtain adequate volumes of water for our analytical requirements, as water recovery in this well was generally slow. The chemical data obtained for the samples are listed in Appendix A. The chemical composition of water obtained from the 3 m-deep "A" wells are similar to those listed for sample Z-109 (Table A1), collected prior to CO_2 injection in Well 2B, and remained relatively unchanged following CO_2 injection primarily because their perforations are located below the CO_2 injection pipe.

The major cations and anions listed in Appendix A and plotted in the included figures carry analytical uncertainties of approximately ±3%. The uncertainties are ±5% for trace metals, and these may be more than ±10% for trace metals that are close to their detection limits. For sample collection, preservation, analysis, and uncertainties applicable to these results, see Kharaka and Hanor (2007) and references therein.

Sample collection started in July 7, 2008, before the CO_2 injection, which began at 15:45 on July 9, 2008. Injection was continuous, except for a few short intervals when it was interrupted for various reasons. CO_2 injection ended on August 7, 2008, but water sample-collection continued through August 14, 2008. During the sampling period, there were several relatively large rainfall events that impacted the chemical composition of the groundwater and raised the groundwater levels in the wells (Figure 3.1). On the other hand, groundwater levels fell as a result of either drainage or evapo-transpiration and water sampling (Figure 3.1).

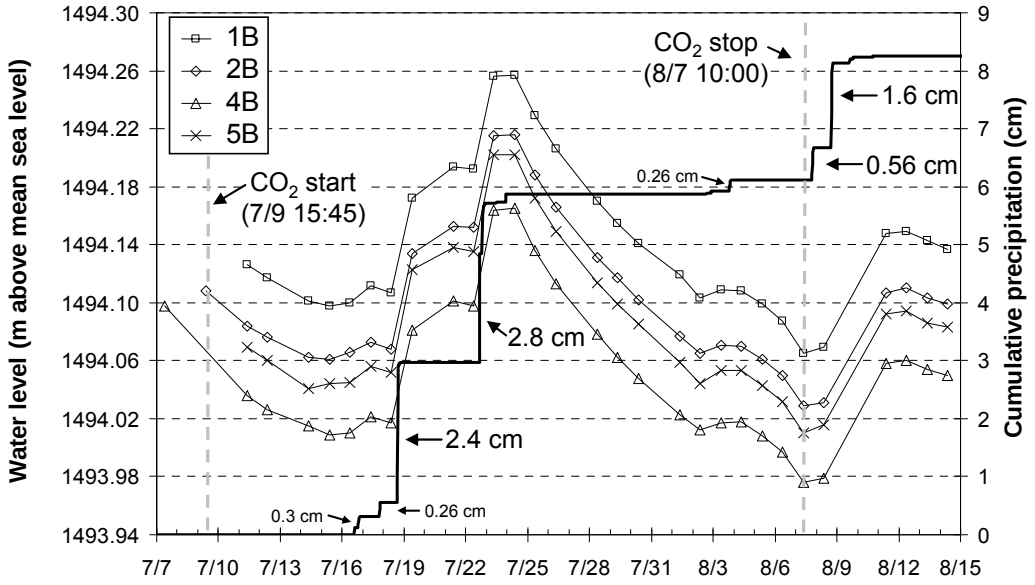

Figure 3.1. *Cumulative precipitation and groundwater levels in selected ZERT wells during the sampling period in 2008.*

3.1. Dissolved Inorganic Chemicals

The chemical data obtained for samples from shallow and deep wells prior to CO_2 injection show that the groundwater in the area is a Ca-Mg-Na-HCO_3 type water, with a fresh water salinity of about 600 mg/L TDS (Figure 3.2; Sample Z- 109 in Table A1). The groundwater has a pH of approximately 7, and HCO_3 is the dominant anion. The concentrations of Cl and SO_4 are relatively low. The initial concentrations of Fe, Mn, Zn, Pb, and other trace metals are at ppb levels, which is typical of shallow groundwaters in regions of moderate precipitation.

Following CO_2 injection, the pH of groundwater decreased systematically to values around 6.0 at wells 1B, 2B, and 5B, all in close proximity to the injection pipe, strongly responding within one day. The strongest early response occurred in Well 2B, only 1 m from the injection pipe and in the direction of groundwater flow, decreasing to a pH of 5.7 (Figure 3.3a). The pH of water for samples from Well 4B (6 m from pipe) started decreasing only after three days following CO_2 injection, but pH values remained above pH 6.0 (Figure 3.3a). The pH in all wells started increasing towards 6.5 after CO_2 injection was terminated on August 7, 2008. The measured pH values of groundwater were controlled primarily by $P(CO_2)$, which was measured by Strazisar et al. (2009) in capped wells, and was computed with SOLMINEQ (Kharaka et al., 1988) using the measured temperature, pH, alkalinity, and other chemical parameters. The $P(CO_2)$ values measured and computed for the ZERT samples were 0.035 bar before CO_2 injection; they increased to values close to 1.0 bar following CO_2 injection. It is evident from these results that pH is an excellent early indicator for detection of CO_2 intrusion into groundwater.

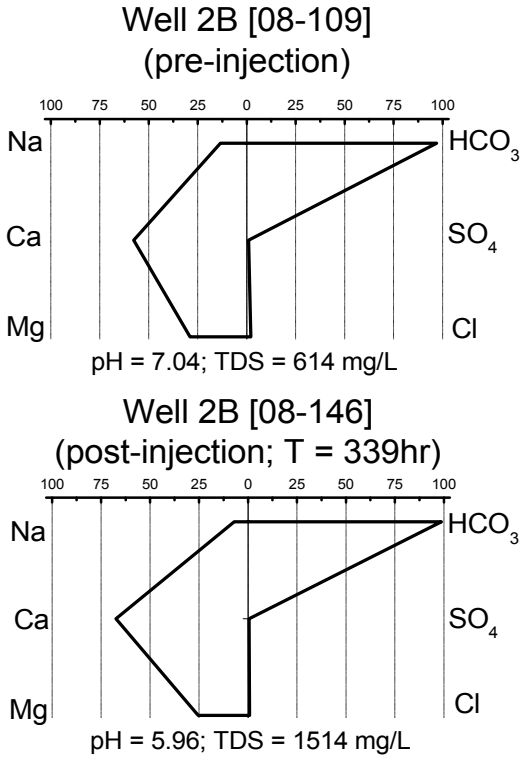

Figure 3.2. *Modified Stiff diagrams showing concentrations (equivalent units normalized to 100%) of major cations and anions, together with salinity and pH of groundwater from well 2B before and during CO_2 injection.*

The alkalinity of groundwater increased from about 400 mg/L as HCO_3 to values higher than 1,300 mg/L, following CO_2 injection (Figure 3.3b). Alkalinity values for different wells, as with the pH values, show variable trends reflecting distance from the CO_2 injection pipe, impacts from precipitation events, and possibly local variations in the mineral composition of soils and sediments. Given the reasonable assumption that the initial groundwater composition for Well 5B was similar to the average background composition at the site, the alkalinity values for this well and Well 2B increase first and show the highest alkalinities (up to 1330 mg/L). The alkalinity values in Well 4B, which is furthest away from the injection well, increase more slowly and only to about 700 mg/L. The alkalinities in all wells decrease to values approaching 400 mg/L after termination of CO_2 injection (Figure 3.3b).

Values for the electrical conductance, also measured at the site, show similar trends to alkalinity, increasing from ~600 µS/cm before CO_2 injection to approximately 1800 µS/cm following CO_2 injection (Figure 3.3c). Assuming that the electrical conductivity of the groundwater in Well 5B was initially similar to the average background value at the site, the conductance values for wells 1B, 2B, and 5B increase first and show the highest conductance. Conductance values for Well 4B increase more slowly and only to about 1,100 µS/cm. All conductance measurements decrease to values approaching 600 µS/cm after termination of CO_2 injection on August 7, 2008 (Figure 3.3c).

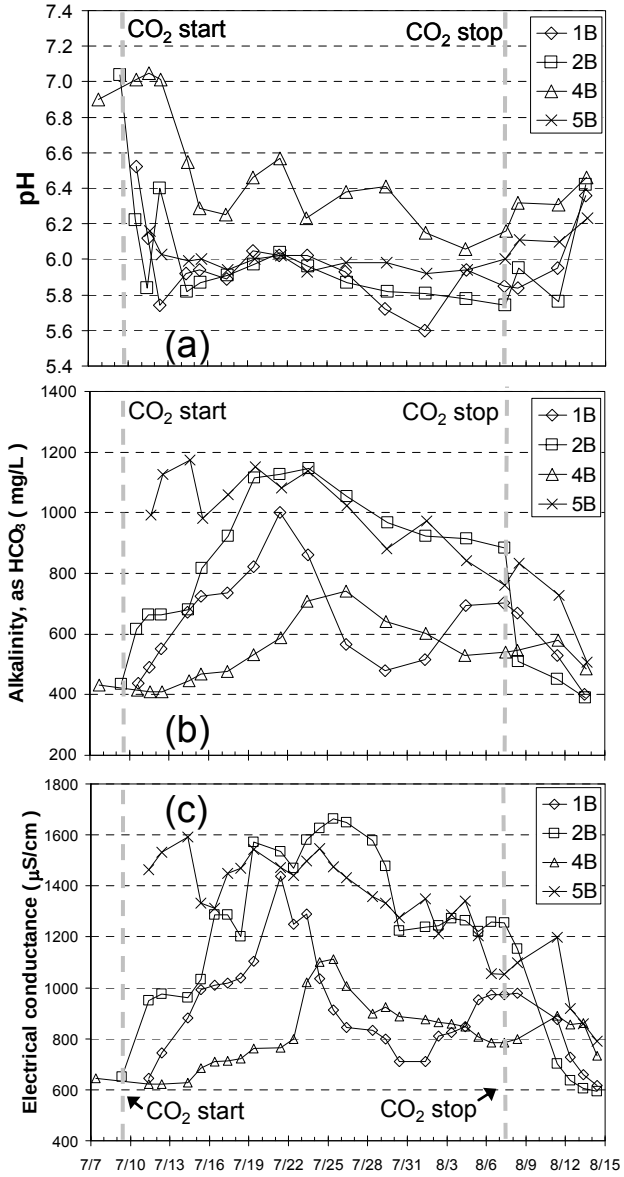

Figure 3.3. *Field- measured groundwater pH values (a), alkalinities (b), and electrical conductance (c), obtained from selected ZERT wells as a function of time of sampling. Note the systematic decrease in pH values from ~7.0 before CO_2 injection to values as low as 5.6 during injection, and subsequent pH increases after CO_2 injection ended. Alkalinities increased from about 400 mg/L before CO_2 injection to values close to 1200 mg/L as HCO_3, and electrical conductance also increased from about 600 µS/cm before CO_2 injection to values higher than 1,600 µS/cm during injection.*

The alkalinity increases following CO_2 injection are balanced primarily by increases in the concentrations of Ca and Mg, whereas the concentrations of Na (10 ±2 mg/L) are relatively constant (Figure 3.4). The molar and atomic concentrations of Ca increase the most, with atomic values for Ca increasing from about 80 mg/L to up to 240 mg/L, and those for Mg increasing from about 25 mg/L to up to 70 mg/L (Figure 3.4). In Section 4.2, we report the presence of calcite throughout the sampled sediment column, as well as a small fraction of detrital limestone and dolomite. The presence of these carbonate minerals could explain increases of Ca and Mg upon dissolution. However, atomic Ca/Mg ratios obtained initially and following CO_2 injection (Figure 3.5) cannot be

explained by dissolution of dolomite alone; the values, increasing from 3.2 to 6.1 for Well 2B, indicate that dissolution of calcite is dominant, but that dissolution of both calcite and dolomite (or Mg-rich calcite) are required to explain the changes in alkalinity and concentrations of Ca and Mg (Figure 3.5, Table A1). Dissolution of calcite (reaction 3-1) and dolomite (reaction 3-2) can be represented by the following reactions:

$$CO_{2(g)} + H_2O + CaCO_{3(s)} = Ca^{2+} + 2HCO_3^- \quad (3\text{-}1)$$

$$2H^+ + CaMg(CO_3)_{2(s)} = Ca^{2+} + Mg^{2+} + 2HCO_3^- \quad (3\text{-}2)$$

These conclusions are supported by the initial characterization of minerals in core samples that show that calcite is abundant in a caliche layer observed at depths of ~50-80 cm. Small amounts of carbonates (~2% detrital limestone and calcite coatings on grains) were also observed in gravels below the caliche layer (Section 4.2). Results of geochemical modeling with an updated SOLMINEQ (Kharaka et al., 1988) support dissolution of calcite and disordered dolomite as possible reactions at all pH values; also, groundwater is undersaturated with respect to dolomite at the lowered pH values obtained following CO_2 injection, allowing for its dissolution. Desorption-ion exchange reactions on clay minerals with H^+ are also suggested as an alternative and/or additional mechanism leading to increases in the concentrations of Ca, Mg, and other dissolved species, as discussed further in Sections 5.2 and 5.3

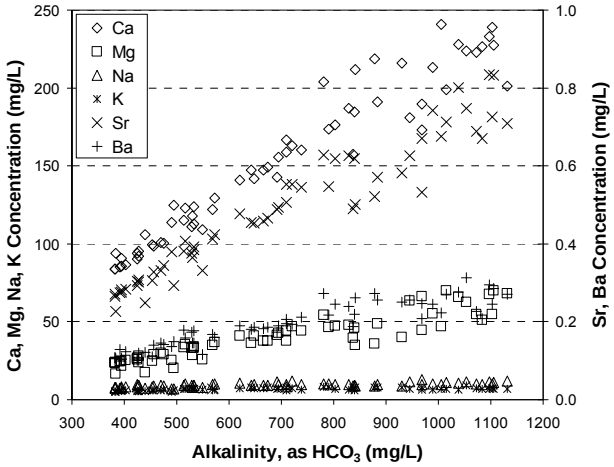

Figure 3.4 *Concentrations of major cations in groundwater from the ZERT wells plotted as a function of water alkalinities. Note the relatively constant concentrations of Na and K, but the general increases in the concentrations of divalent cations with water alkalinities, possibly indicating dissolution of carbonate minerals.*

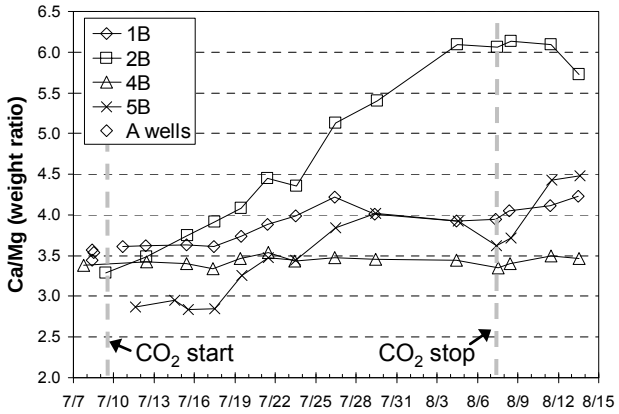

Figure 3.5 *Ca/Mg weight ratios plotted as a function of time of sampling. Note that the ratios are higher than the value expected from dissolution of dolomite (1.6), and are relatively constant for well 4B, but continue to increase for well 2B until CO_2 injection was terminated, possibly indicating dissolution of calcite.*

The concentrations of Fe and Mn, the two most abundant trace metals in groundwater, also increase following CO_2 injection (Figure 3.6). The concentrations of Fe in groundwater could increase from dissolution of Fe(II) and Fe(III) minerals. These potentially include Fe (hydr)oxides such as ferrihydite and green rust (see Section 5.2), which are likely to be present from the oxidation of primary phases such as magnetite and biotite, observed in the sediments (Section 4.2). Dissolution of siderite would also result in increased Fe concentrations. However, thermodynamic evaluations (Section 5.2) indicate the groundwater to be quite undersaturated with respect to this mineral, suggesting it is not likely to be present, except potentially as a detrital phase. Example dissolution reactions include:

$$Fe(OH)_{3(s)} + 3H^+ = Fe^{3+} + 3H_2O \quad (3\text{-}3)$$

$$4FeOOH_{(s)} + 8H^+ = 4Fe^{2+} + 6H_2O + O_2 \quad (3\text{-}4)$$

$$4Fe(OH)_3 + CH_2O + 8H+ \Longrightarrow H_2CO_3 + 4Fe^{+2} + 10H_2O \quad (3\text{-}5)$$

$$Fe(CO_3)_{(s)} + H^+ = Fe^{2+} + HCO_3^- \ , \quad (3\text{-}6)$$

where CH_2O is a generic representation of dissolved (and particulate) organic matter. The concentrations of Fe in groundwater are a strong function of Eh, which could only be measured in water from the deep wells that were not impacted by CO_2 injection, because shallow wells did not yield enough water volume. The Eh values obtained (150 to 200 mV; pe ~ 2.5–3.5) indicate suboxic conditions that account for the low concentration of dissolved Fe; much higher Fe values are possible under more reducing conditions because of the higher solubility of Fe(II) minerals (Hem, 1985). Note that Eh measurements may be of limited use, as discussed in Section 5.2. The Fe concentrations (Figure 3.6a) increase from 5 to 1200 ppb, but show very low values during July 20 to July 26 following significant rainfall events (Figure 3.1) even when pH values were low. Dilution alone cannot explain the low Fe concentrations during July 20 to July 26, but the low values could be attributed to more oxic conditions, possibly caused by increased dissolved O_2 content in

groundwater transported with percolating water from rainfall events. Ion exchange reactions on clays with H^+ and major dissolved cations, such as Ca, Mg, and Na, are other possible controls on Fe concentrations, as discussed in Sections 5.2 and 5.3.

The concentrations of Mn show similar trends to those of Fe, increasing from 5 to 1400 ppb following CO_2 injection, but also show low values during July 20 to July 26 (Figure 3.6b). Dissolution and redox reactions can be written for Mn as for Fe above. It should be noted that Mn concentrations are higher for Well 4B than for 2B and 5B, and this may be controlled by local mineral compositions.

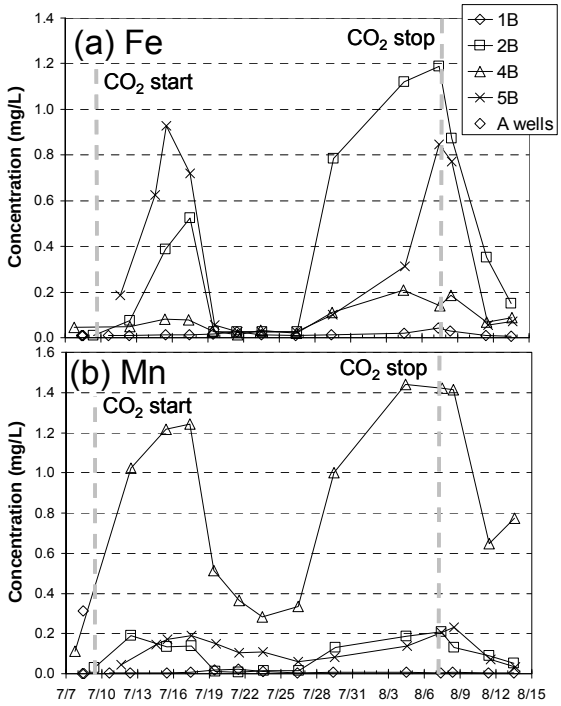

Figure 3.6 *Concentrations of Fe (a) and Mn (b) in groundwater from selected ZERT wells plotted as a function of time of sampling. Note the low Fe and Mn concentrations during July 20 to July 26, which we are attributing to the oxidizing conditions possibly caused by percolating oxygenated water from rainfall events (see Figure 3.1).*

The concentrations of Pb, As, Zn, and other trace metals (Table A1 and Figure 3.7) generally show an increase with increasing alkalinity (lower pH value) following CO_2 injection. The values reported, however, carry high uncertainties (10–50% analytical error) as they are, in some cases, close to the analytical detection limits, especially with the required dilutions (up to 5 fold) prior to analyses. The concentration increases are likely caused by desorption-ion exchange reactions with H^+, Ca, and Mg resulting from lowered pH values (see Section 5). Because measured H_2S values were below our detection limit (0.2 mg/L), we are unable to use geochemical modeling to check for solubility of sulfide minerals as controls on metal concentrations. The concentrations, it should be noted, are all significantly below the maximum contaminant levels (MCLs) for the respective trace metals (e.g., 15 ppb for Pb, 6 ppb for As). The initial values and the increases in concentrations of these trace metals, although small, are readily measured by the sampling and analytical methods

used in this study. These results highlight the role of geochemical tools for early detection of CO_2 leakage into groundwater.

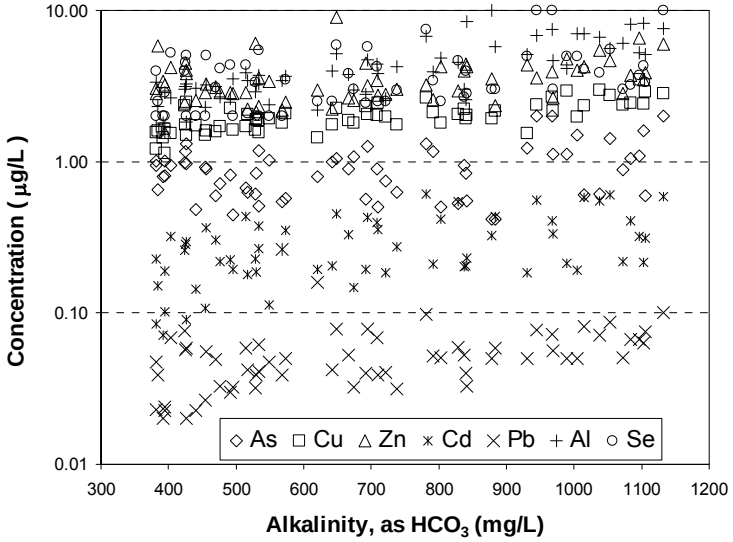

Figure 3.7 *Trace metal concentrations in groundwater from selected ZERT wells plotted as a function of water alkalinities. Some of the scatter shown probably results because the reported values in some cases are close to the detection limits.*

The chemical changes observed in the ZERT groundwater are similar in trends, though much lower in concentrations, to the changes observed in the Frio Brine Pilot test, near Houston, where 1600 t of CO_2 were injected at 1500 m depth into a 24 m thick "C" sandstone unit of the Frio Formation (Freifeld et al., 2005; Hovorka et al., 2006; Kharaka et al., 2006). Following CO_2 breakthrough, 51 hours after injection, Frio samples showed sharp drops in pH (6.5 to 5.5 measured at ground surface), pronounced increases in alkalinity (100 to 3000 mg/L as HCO_3) and in Fe (30 to 1100 mg/L), a slug of very high DOC values, and significant shifts in the isotopic compositions of H_2O, DIC, and CH_4. These data, coupled with geochemical modeling, indicated rapid dissolution of minerals, especially calcite and iron oxyhydroxides, both caused by lowered pH (initially ~3.0 at subsurface conditions) of the brine in contact with supercritical CO_2 (Kharaka et al., 2009b). The differences between results from Frio and ZERT tests are related to several geochemical parameters, but the most important reason relates to the difference in subsurface $P(CO_2)$ value, which was approximately 150 bar at Frio (Kharaka et al., 2009b), while $P(CO_2)$ values at ZERT measured (Strazisar, 2009; Strazisar et al., 2009) and computed with SOLMINEQ (Kharaka et al., 1988) ranged from 0.035 to ~1 bar. The amount of CO_2 dissolved in water is a function of fluid pressure, temperature and salinity. The CO_2 solubility increases at higher pressures, but decreases at higher (moderate) temperatures and salinities. In the present case, the large difference in pressure between the ZERT and Frio sites has a stronger effect than differences in temperature and salinity between the two sites. Thus, in a shallow aquifer such as that at the ZERT site, much less CO_2 can dissolve in the groundwater compared to the amount that can dissolve in deep pressurized formation waters such as at the Frio site. Therefore, the CO_2-induced decrease in groundwater pH will be less pronounced, and thus the corresponding change in dissolved groundwater constituents will also be less. Consequently, trace metal mobilization from solids is expected to be less pronounced at shallow sites such as ZERT.

3.2. Dissolved Organic Chemicals

Dissolved organic carbon (DOC) values obtained in this study are generally about 4 mg/L, with a variation range from 2.6 to 6.9 mg/L, and these variations do not seem related to CO_2 injection. Concentrations of benzene, toluene, ethyl-benzene, m-, p- and o-xylene (BTEX) were determined in a relatively large number of samples collected when it became clear that the injection of CO_2 was likely responsible for very small but systematic increases in the concentrations of dissolved BTEX compounds (up to ~1.6 µg/L for m-, p-xylene), as depicted in Figure 3.8. It should be noted that the concentrations are all below the maximum contaminant levels (MCLs) for the respective BTEX compounds (5 ppb for benzene). There is some scatter in the results, but the concentrations are about 0.2 µg/L before CO_2 injection, increasing to values greater than 1.0 µg/L for m-, p-xylene and o-xylene, and to about 1.0 and 0.8 µg/L for toluene and benzene, respectively. The measured values are higher in water from Wells 1B (Figure 3.8a) and 2B (Figure 3.8b) relative to Well 4B, which is farther away from the injection pipe (Figure 3.8c). All the measured BTEX values decrease to a value approaching pre-injection (~0.2 µg/L) after termination of CO_2 injection on August 7, 2008 (Figure 3.8d).

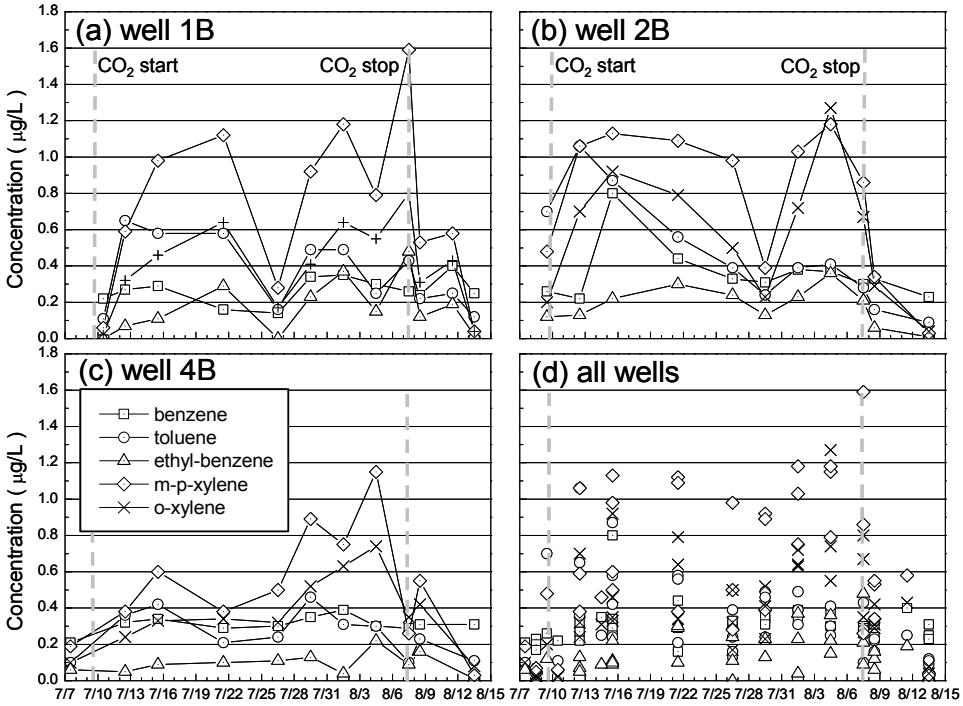

Figure 3.8 *Concentrations of BTEX compounds detected in groundwater from selected ZERT wells plotted as a function of time of sampling. The BTEX concentrations are all significantly below the maximum contaminant levels (MCLs) (e.g., 5 ppb for benzene).*

The origin of the low amounts of BTEX compounds detected in groundwater following CO_2 injection was investigated during 2008, and more recently in 2009. Three main possible sources were examined: (1) A natural source from deep organic matter or a petroleum source; (2)

contamination from a surface source or when installing the injection pipe and groundwater wells; or (3) contamination with trace amounts of BTEX in the injected CO_2, although the gas used was food-grade quality. Our initial results obtained in 2008 were inconclusive with regard to the injected CO_2 being the source of the observed BTEX. We analyzed core samples obtained from wells drilled in December 2008 for BTEX. Though progress was slow because results obtained were close to the detection limits of available analytical methods, results showed that BTEX concentrations were below detection limits. Thus, natural sources were eliminated as a possibility for the observed concentration increases. Purge-and-trap analysis of CO_2 samples collected from the injection source tank in 2009 showed conclusively that the injected CO_2 (though food-grade) contained a very small amount of organic chemicals and thus was identified as the source of the trace concentrations of detected BTEX (Kharaka et al., 2009b). Our results indicate that BTEX compounds can be detected in groundwater at extremely low concentrations, below MCL levels.

4. MINERALOGICAL DATA

4.1. Core Analysis and Methods

Three wells were installed in December 2008 to obtain core for mineral characterization and laboratory experiments. Well W6 is 2.6 m deep with the bottom 0.76 m screened. Wells W7 and W8 are 3 m deep with the bottom 1.5 m of the wells screened (Figure 2.2). Cores from these wells have been logged and sampled at different intervals for detailed mineralogical analysis. Approximately 20 samples have been collected from the cores for rock, mineral, and grain-size analysis, and 17 samples of these have been dry-sieved to 3 size fractions with grain-size diameters of (1) >9.5 mm (medium gravel +); (2) 9.5–2.0 mm (fine to very fine gravel), and (3) < 2 mm (coarse sand to clay/colloid). X-ray diffraction (XRD) work was completed with the primary goal of identifying carbonates and clays. Short exploratory sessions were conducted with a scanning electronic microscope (SEM), including some semi-quantitative chemical analysis using the Energy-Dispersive X-Ray (EDX) system on the SEM. The short summary given below focuses on ZERT Well W6, which is located in the main well field (Figure 2.2). A log for well W6 is given in Table B.1 in Appendix B. The grain size fraction for different zones in Well W6 is shown in Figure 4.1.

It should be noted that the cores were obtained by a “direct-push” geoprobe, using a 3-inch geoprobe system. The direct-push methodology creates a bias in the true grain-size distribution because the larger cobbles, which are abundant throughout the cored interval (even the top “A” soil horizon), are simply pushed out of the way. Large well-rounded cobbles exceeding 10 cm diameter exist in abundance throughout the cored interval.

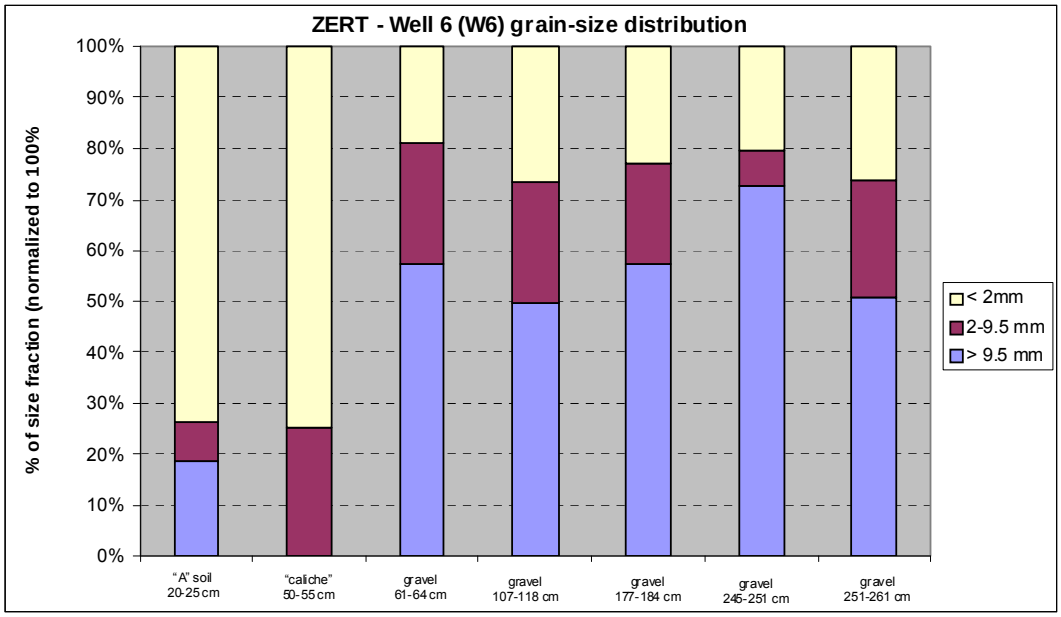

Figure 4.1 *Grain size fractions for different zones in Well W6.*

4.2. Mineralogical Results

The cores have an organic-rich dark soil zone at the top (0 to ~40 cm), which grades into a light to medium gray "caliche" zone. The caliche zone is high in carbonate and clay, with lesser fine sand to fine silt (predominantly quartz, feldspar and white mica, and very minor volcanic rock fragments). Clay extracts from the caliche zone of W6 appear to be smectite. The carbonate mineral is calcite; however, the XRD pattern shows it is poorly crystallized, with a peak shift towards Mg-rich calcite.

"A" soil horizon

The top 30-40 cm of each core consists of clay and organic-rich soil. The soil is generally brown, plastic, and matrix supported with some fine sand. The topsoil zone grades into a caliche layer that is ~20-40 cm thick. The mineralogy has not been studied in detail. XRD analysis performed on the clays from earlier auger core samples indicated chlorite; however, our study indicates the caliche clay is dominantly smectite. Some well-rounded pebbles, possibly volcanic andesite, are found in the top soil.

Caliche or high carbonate zone

The caliche zone begins at ~40 cm, graded gently in color from dark brown topsoil to medium and light gray. The caliche zone is very fine-grained, with most material passing easily through 2 mm sieve (Figure 4.1). Unlike the caliche from a hand-augered core taken previously from other nearby wells (located at gridpoint -5,-3 on the reference grid), which was predominantly carbonate with lesser amounts of clay and fine sand, the caliche zone at Well 6 appears to be more clay and quartz-dominated fine sand and silt, and less carbonate. The XRD scan of a bulk powder sample shows quartz and clay (smectite), with significant calcite and plagioclase, and minor but measureable kaolinite and mica. XRD results suggest that the main clay mineral is smectite (main 001 peak ~14

angstroms, with a shift to ~17 angstroms upon glycolation, and a slightly higher peak shift using glycerol). More work would be needed to describe the clays in more detail. An SEM stub was prepared with the caliche material; however, the carbonate and clay was so fine-grained and co-mingled that it was not possible to resolve the morphology of the crystals or to isolate grains for elemental analysis. Mica is readily identified in sieved samples from the caliche; it is predominantly white (muscovite) and lesser green mica. Mafic rock fragments are a very minor constituent of the caliche zone.

Gravel zone

Below the caliche zone, the core changes rapidly to coarse gravel, with large pebbles up to the full diameter of the core (~6 cm), and gravel (> 2 mm) representing ~75% or more of the core. The gravel continues to the bottom of each 10 ft deep well. Megascopically, there are no obvious distinct zones. A total of 15 samples, ranging from ~150 to 400 grams, were collected from the gravel zones of the three wells (5 samples from W6; 4 samples from W7; 6 samples from W8). Because the gravel was so coarse, the entire diameter of the core was collected for each sample, from core intervals of ~5 to 10 cm. The grain size fractions for all 15 gravel samples analyzed from wells 6, 7, and 8 are plotted in Figure 4.2.

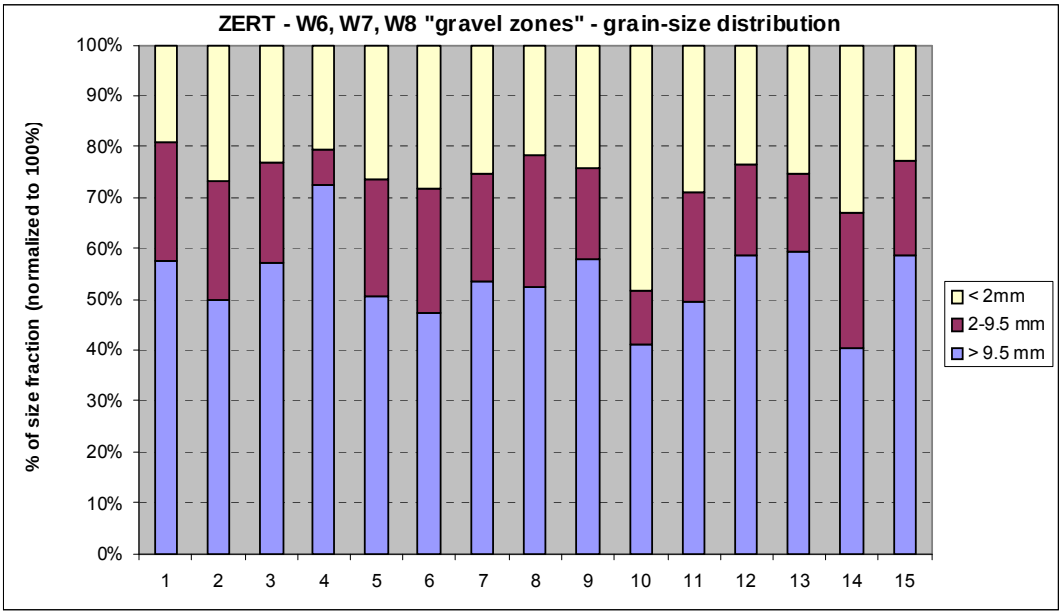

Figure 4.2 *Grain size fractions for 15 gravel samples analyzed from wells 6, 7, and 8.*

Overall, the gravel material can best be described as "extremely heterogeneous," and it would be a significant task to identify all the rock types and minerals in this gravel. An approximate distribution of rock types in the gravel is presented below, with results from W6:

- Approximately 60%–70% mafic/basic volcanic rocks, likely andesite (mostly aphantic, some small plagioclase laths). Usually subangular to subrounded habit, often with broken edges. Some volcanic fragments have a pale blue "oxidized" exterior, but when broken are fresh. XRD shows dominant mineral is Ca-Na plagioclase (albite to anorthite). Semi-

quantitative SEM/EDX "spot scans" of several feldspars showed a wide range of Na to Ca. Include basalt and diabase in this group. Olivine was identified in some rocks using SEM/EDX.

- ~20-30% quartz –biotite-+/-amphibole gneiss. Habit angular to subangular.

- ~10% misc crystalline rocks, such as red granite/gneiss (with dark red potassium feldspar). Sub-angular. Likely rhyolite (pink-orange, subrounded), quartz-mica schist (angular).

- ~2% limestone—described below.

In general, the darker, denser aphanitic volcanic rocks dominate in the larger size fractions, often as well-rounded pebbles (up to 30 grams weight). A wide range plethora of rock types exist in the smaller size fractions (large sand to fine gravel size)—diabase, schists, granites, vesicular volcanics, rhyolite, and many exotic crystalline rocks, ranging from highly altered/weathered to fresh—that will take considerable some effort to identify.

Most of the mafic volcanic rocks are highly magnetic, so that even rock fragments > 2 mm are easily separated with a 1-ounce horseshoe magnet. The XRD pattern of a separate of fine-grained magnetic material was determined to be magnetite. SEM/EDX spectra of several "Fe-rich" minerals in andesite showed iron and titanium (up to 7 atomic %).

Limestone (in gravel)

Detrital limestone (not found in the core-catcher samples) is present in the gravel zone of Well 6, as a very small fraction of the total gravel. Of 97 hand-checked pebbles (~1 cm+ diameter) from the five W6 gravel samples, only 3 pebbles are limestone. Considered by weight, the 3 limestone pebbles total only 10.2 grams, from a total weight of 573 grams of is this size fraction. The limestone has a resemblance in color and texture to the Madison limestone; however, it appears even more fine-grained than the hand specimen we have of Madison Limestone. The conchoidal fracture and XRD pattern shows it to be well-crystallized calcite. Limestone is also present in the 2–9.5 mm size-fraction, again in very small amounts (~2%).

Carbonate

Calcite, primarily as a coating, is a common minor constituent throughout the gravel zone. Calcite also commonly occurs as crusts of secondary calcite on rounded rock surfaces, from small to medium pebbles. An XRD pattern of such a carbonate crust was determined to be well-crystallized calcite. All 94 noncarbonate pebbles from the > 9.5 mm size fraction had a carbonate coating and/or crust and reacted slightly-to-vigorously to dilute HCl. Likewise, all of the matrix samples (sieved and unsaved) reacted to HCl. Calcite also occurs throughout the matrix as very fine rounded grains, which dissolve in a few seconds in dilute HCl. We find no dolomite in the coarse fractions, although the 2–9.5 mm fraction would need further study. The finer size fractions likely contain some dolomite, identified as small rounded grains that fizz very slowly in 10% HCl (as opposed to calcite, which fizzes rapidly. Because the dolomite fractions are too small to appear in bulk XRD powders (generally ~5% by weight is needed), SEM or hand-picked grains would be necessary for positive identification.

Matrix minerals

In the progressively finer size fractions, minerals predominate over rock fragments and lighter minerals predominate over darker minerals. For minerals, quartz is dominant, followed by feldspar. Micas are abundant in all the size fractions, with muscovite more abundant in the finer sizes compared to biotite. Green and brown mica are also present (possibly chlorite, phlogopite). For the darker minerals, amphibole appears most abundant; pyroxene is not easily spotted in matrix, although common in some rock fragments. Magnetite is abundant. Carbonate, as a coating, and calcite as very small rounded grains are found throughout the gravel zone. Fe-oxides, as yet unidentified, are present in the matrix, both as fine coatings on other minerals (often quartz) and as small rounded and powdery grains. Some pistachio green epidote was observed on a pebble surface.

Sulfides

No sulfide minerals have been identified in the matrix. Pyrite is rare in some rock fragments, typically on fresh surfaces. The SEM backscatter system was used on many rock grains to recognize sulfide minerals, but none were found in our samples. High Fe targets were usually found to be oxides, magnetite, or titaniferous magnetite.

5. HYDROGEOLOGICAL AND GEOCHEMICAL INTERPRETATION

The groundwater data collected to study the effect of CO_2 injection on groundwater quality at the ZERT site was presented in Section 3. Here, the groundwater data collected during this study are evaluated in a more quantitative manner, in light of the site hydrogeology, its mineralogical characterization, and the various geochemical processes likely to result from CO_2 dissolution in water.

It should be remembered that this study was conducted in a shallow water-table aquifer, only a couple of meters below ground surface, at essentially atmospheric pressure, and thus under conditions that are not representative of deeper USDW. In addition, because of the thin vadose zone, recharge from rainfall events during the test (Figure 3.1) had a rapid and noticeable effect on groundwater composition trends, complicating data interpretation. Nevertheless, geochemical data collected during this study are quite useful to test some hypotheses regarding the effect of CO_2 dissolution in groundwater, namely that the pH decrease and alkalinity increase accompanying CO_2 dissolution in water are likely to drive dissolution and desorption/exchange reactions that could impact groundwater quality. These reactions would be expected to take place in any aquifer, although to a lesser extent in a shallow site such as ZERT compared to a deep USDW. This is because, as mentioned earlier, less CO_2 can dissolve in water at low pressure than at high pressure, thus limiting the pH decrease and alkalinity increase (e.g., reaction 1-1) accompanying CO_2 injection. Obviously, the geochemical response of an aquifer to CO_2 dissolution also highly depends on the aquifer mineralogy, salinity, redox conditions, and initial (background) pH. Because these data are site-specific, results of analyses presented in this section should not be directly applied to other sites, except for illustrating the general type of reactions (and not their specific effect or magnitude) that could take place at other locations.

Section 5.1 summarizes what is known about CO_2 transport in the subsurface at the ZERT site, to provide context for evaluating the water quality response to CO_2 injection. In Section 5.2, statistical and thermodynamic analyses are presented to determine correlations between the concentrations of various species, and formulate hypotheses on the types of mechanisms likely responsible for observed concentration trends and groupings of certain species. Based in part on this information, geochemical modeling analyses are then presented in Section 5.3. The modeling incorporates processes (i.e., dissolution, sorption/desorption, and ion exchange) that are most likely to affect groundwater quality upon CO_2 injection. Besides providing possible explanations for observed water quality changes at the ZERT site, the modeling also illustrates the types of coupled geochemical mechanisms that could affect groundwater quality in deeper USDW.

5.1. Transport of CO_2 in Gas and Aqueous Phases

The transport of CO_2 in the subsurface at the ZERT site (e.g., as gas phase in the vadose zone and dissolved in groundwater) is assessed in other parallel studies (Lewicki et al., 2007; Strazisar et al., 2009; Oldenburg et al., 2009). As discussed in Section 2.3, groundwater flow velocities at the site may be up to 2 m/d, which is very high, and rates of CO_2 transport in the unsaturated zone are estimated to be at least an order of magnitude higher. Therefore, the rapid and systematic changes observed in the chemical composition of groundwater at ZERT are likely driven by both the fast spreading of CO_2 as gas phase in the sand-gravel unsaturated zone under the upper soil layer, followed by re-dissolution into the groundwater, as well as by transport of groundwater with dissolved CO_2 (see schematic in Figure 5.1). Notice that in both transport scenarios, the deeper A-wells are not significantly affected by the injected CO_2. Redissolution of gaseous CO_2 is limited to a small layer at the soil-groundwater interface, while the flow of CO_2-charged water from the injection well bypasses the A-wells, because the screening interval is too deep.

The fast transport in the gas phase is directly supported by gas samples obtained from the head space of the groundwater wells. CO_2 concentrations in wells 1B, 2B, and 5B increased up to about 90% (by volume) only two days after injection started (Strazisar, 2009). These wells are all less than 2 m away from the injection pipe, with 5B actually located upstream (Strazisar et al., 2009). Well 3B about 3 m downstream arrives at 50% CO_2 after about 5 days; Well 4B about 6 m downstream starts to respond after the same time period. Model results from Oldenburg et al. (2009) also indicate that gaseous CO_2 spreads out fast through the vadose zone under the soil layer. It is thus quite certain that dissolution of CO_2 from the vadose zone back into groundwater is a prominent process triggering the chemical changes measured in the groundwater samples. However, because the groundwater flow velocity is very high (up to 2 m/day), the transport of dissolved CO_2 in groundwater cannot be ruled out as an additional main source of CO_2 responsible for the groundwater quality changes, at least in the shallower wells located downstream from the injection pipe. Because uncertainties remain regarding gas and groundwater flow rates, recharge effects, and subsurface heterogeneity, no attempts were made, here, at modeling the reactive transport of CO_2 in the subsurface. We focus instead solely on geochemical modeling of reactive processes, such that the transport specifics responsible for increased CO_2 levels at monitored locations are not needed.

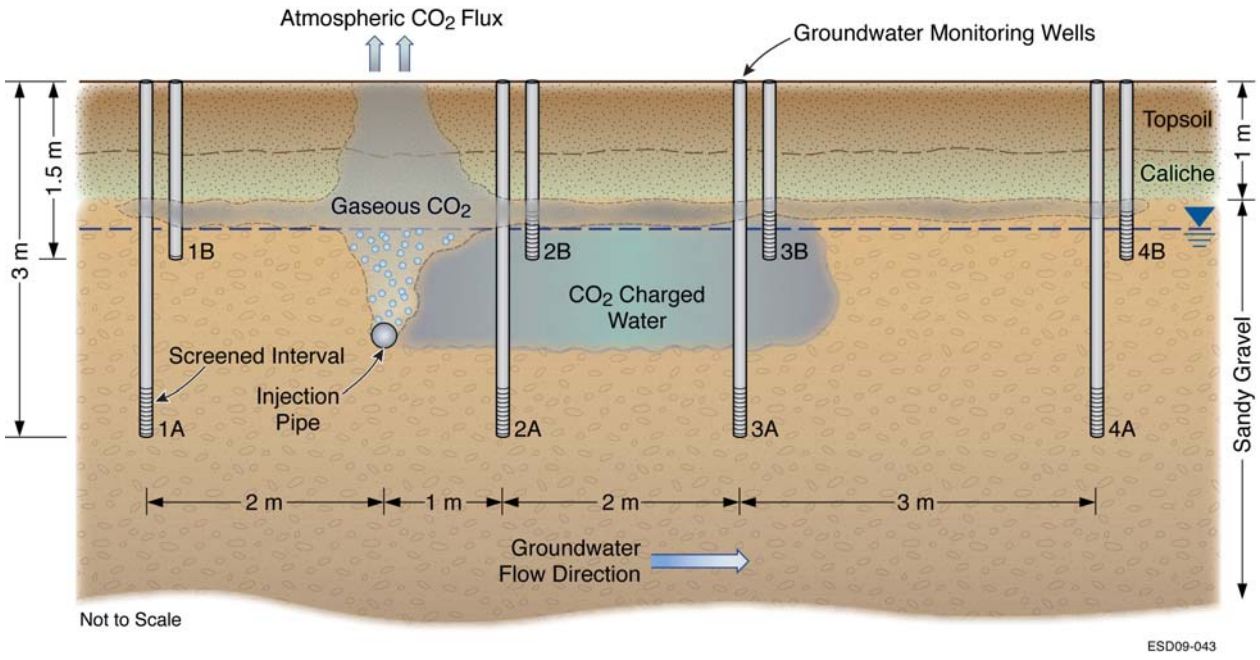

Figure 5.1 *Schematic representation of CO_2 transport in ZERT field site. The cross-section shown is along the axis of well pairs 1A/B, 2A/B, 3A/B, and 4A/B.*

5.2. Geochemical Response to CO_2 Release and Interpretation

The characterization of the geochemical response of groundwaters in the shallow phreatic zone at the ZERT site was undertaken in response to the opportunity afforded by an independent field program to evaluate phenomena associated with the atmospheric leakage of CO_2 from underground storage sites. Both time and funding constraints limited the scope of the study, which was recognized at the outset as being exploratory in nature, and aimed at defining the relevant geochemical processes relating to CO_2 contamination of subsurface potable water sources, rather than their quantification. This section discusses several steps undertaken to interpret chemical analyses of groundwaters from the ZERT site, in an effort to provide a framework for the geochemical modeling conducted in Section 5.3.

The large number of species analyzed in groundwaters from the ZERT site, and their temporal variation, provides a basis for understanding the transient chemical processes operating in the phreatic zone near the water table and the overlying vadose zone. These processes include the following:

- Dissolution of CO_2 in the groundwater
- Evaporative concentration
- Infiltration of rainfall
- Bacterial mineralization of organic matter with generation of CO_2
- Oxidation/reduction
- Ion exchange

- Adsorption
- Mineral precipitation/dissolution

The depression of pH due to CO_2 uptake in the groundwater can induce dissolution of a number of primary and secondary minerals, and drive sorption/desorption and ion exchange reactions. The bicarbonate ion generated during CO_2 dissolution can also compete with other species, such as the arsenate anion for adsorption. Fluctuations in the concentrations of oxidants and reductants, and the potential inhibition of bacterial activity by increasing concentrations of CO_2, can likewise affect precipitation, ion exchange, and adsorption of those species that are subject to changes in oxidation state. The evaporation induced by the bubbling of CO_2 through the groundwater, with concomitant removal of dissolved redox-sensitive gaseous species (e.g., O_2, N_2, CH_4, and H_2S), may disturb the oxidation state and also lead to evaporative concentration of nonvolatile species. Random periods of rainfall are likely to flush residual capillary waters from the overlying soil horizons of the vadose zone, which have been subject to evapotranspiration and modification by pedogenic processes. These vadose zone soil waters also contain the concentrated residues of dissolved species from earlier rainfall events. Bacterial oxidation of organic matter transported from the overlying soil zone in the dissolved or particulate state modifies the concentration of dissolved concentration of carbonate species in the groundwater and leads to elevated partial pressures of CO_2 in the gaseous phase in the overlying vadose zone. Such bacterial activity also modifies the concentrations of nutrients in the groundwater and generates reductants that can likewise induce the reductive dissolution or precipitation of minerals in the saturated zone. Ion exchange can take place in more than one mineral. Adsorption characteristics also vary, depending on the nature of the mineral substrates, of which there may be several.

The information available to help identify transient chemical processes in the saturated zone consists of some 60 comprehensive chemical analyses of groundwaters taken at intervals throughout the test, the temperature and electrical conductivity of the groundwaters samples, information on rainfall events, the height of the water table, and mineralogical analyses of core samples taken from a number of shallow boreholes (see Sections 2 to 4). In addition, data on the chemical composition of rainwater collected at two sites in Montana were downloaded from US EPA's National Pollutant Discharge Elimination System (NPDES) web site to estimate contributions of dissolved species to the groundwater from that source. These data are evaluated below using Principal Component Analyses (PCA) to determine whether certain species correlate with each other, potentially indicating similar or coupled geochemical behavior, and to shed light on possible geochemical mechanisms at play upon CO_2 injection. Because the geochemical behavior of many metal species in groundwater is tied to oxidation state, and because uncertainties remain concerning the controlling redox processes within the saturated zone at the ZERT site, thermodynamic analyses are also presented to help constrain the identity of potential phases exercising thermodynamic control over the redox potential at this site.

5.2.1 Principal Component Analysis

Principal Component Analysis (PCA) is a statistical tool for the interpretation of datasets consisting of multiple observations in each of many samples, and where it is desired to determine linear relations between the observations in the dataset. The aim is to reduce the observed relations among the variables to simpler relations between fewer variables, called principal components. These

principal components are linear combinations of the variables, which are not correlated, but which explain the total variance of the data.

In evaluating the groundwater analyses from the ZERT site, PCA does not identify what each principal component relates to in terms of the chemical processes taking place in the field. However, it does identify which chemical species are strongly correlated with a given principal component, and this in itself provides a basis for hypothesizing the relationship of each principal component to a chemical process that is likely to be operative. Unequivocal assignment of any specified chemical process to each of the derived principal components is plausible only in conjunction with an independent evaluation of the mineralogy, interpretation of measured soil chemical and physical properties, and independent thermodynamic and kinetic analyses. The interpretation can be further strengthened through an independent comparison of modeled predictions of groundwater composition with field observations, as is illustrated in a subsequent section of this report.

Shlens (2009) points out that certain assumptions are implicit in PCA for it to be effective:

1. Relations between the variables should be linear, although nonlinear regimes have been explored.
2. It is assumed that large variances have important structure. In other words, the data have a high signal-to-noise ratio, and the principal components with larger associated variances represent interesting structure.
3. The principal components are orthogonal. This assumption makes PCA solvable using linear algebra decomposition techniques.

Treatment of the data

The underlying relations between the various analyzed chemical species in the groundwaters are likely to obey thermodynamic or kinetic mass action relationships, which are defined in terms of the logarithms of the activities of the independent components. For a truly rigorous analysis, these activities would have to be calculated using a distribution of species code such as EQ3/6 (Wolery, 1993) or PHREEQC (Parkhurst and Appelo, 1999), taking into account species complexation and species activity coefficients. However, the supporting thermodynamic databases of such codes are typically incomplete, especially regarding complexation by trace elements, which are of particular interest to this study. Furthermore, since it is unlikely that the sampled groundwaters were in homogeneous equilibrium with respect to redox state, as is discussed further in Section 5.2.2, it is not possible to ascertain with any degree of confidence the likely oxidation state of several of the trace elements or their complexing agents. For these reasons, calculation of the thermodynamic activities of the aqueous basic species was not warranted. For the purpose of PCA, the measured species concentrations were therefore transformed to the logarithmic molar concentrations as proxies for the corresponding activities. The loss of accuracy introduced by this approximation is mitigated somewhat by the sampled groundwaters being very dilute (total dissolved solids (TDS) ≈ < 1,500 mg/L). Furthermore, since the activity coefficients of all charged species vary systematically within the limited range of ionic strength at the ZERT site, the ratio of the activity coefficients of any two species is approximately constant.

A preliminary study of the behaviors of individual chemical constituents indicated that the sampling period should be subdivided into discrete time intervals for evaluation and interpretation, because

different chemical processes became pre-eminent over time, as atmospheric influences changed. Here, we restrict our analysis to a data set consisting of the period utilized to establish the baseline ambient chemistry of the groundwater (July 7–8, 2008), and the initial period following the start of CO_2 injection up to the time when a significant rainfall event perturbed the water table elevation (July 8–17, 2008). This time period allows evaluation of the short-term response of groundwater chemistry to increasing partial pressure of CO_2, $P(CO_2)$. Because of the broad similarities in the chemical responses of the groundwaters to CO_2 injection during this period, regardless of location of the sampled wells, analyses from all wells were combined for the purpose of PCA.

The individual datasets were evaluated using the StatisticXL™ package, which is designed for use with the Microsoft Excel™ spreadsheet software under the Windows operating system. The number of principal components was not constrained, as prior knowledge of the geochemistry of the system suggested that many geochemical processes could be operative, and that independent processes affecting different mineral substrates might condition the initial response of the system to CO_2 uptake.

Results

Table 5.1 displays the correlation matrix of the log molar concentrations of all analyzed species. The correlation coefficients are color-coded in ranges 0.9, 0.8, 0.7, 0.6, 0.5 and 0.4. Very strong correlations exist between the alkali earth metals, Mg, Ca, Sr, Ba, HCO_3, Al, and to a slightly lesser extent with SiO_2. Li, Cd, Pb, Al, Cr, SiO_2 and B are also strongly correlated. Fe and Co are strongly, but inversely correlated with PO_4. Se is strongly correlated with Cr, whereas Mn is fairly strongly correlated with Co and moderately with Fe. Several species show notably weak correlations with other constituents, notably Zn, U, Cl, Br, and NO_3. H (-pH) is most strongly correlated with K (0.856), but is otherwise only moderately correlated with most other constituents. Although some of the observed correlations could be fortuitous, many probably reflect underlying thermodynamic, kinetic, stoichiometric, or mixing relations. These may involve complexing, exchange, or adsorption or, with negative correlations, precipitation. Figure 5.2 illustrates some examples of relevant correlations between various species in solution, which are intended to show that these results might ultimately be used to initiate broader lines of inquiry regarding the behavior of trace metals in response to system perturbations caused by CO_2 injection.

Table 5.1 *Correlation matrix of the log molar concentrations of all species analyzed in MSU-ZERT groundwaters for the period July 8 to July 17, 2008*

	H	Li	Na	K	Mg	Ca	Sr	Ba	Mn	Fe	Co	Cu	Zn	Cd	Pb
H	1.000														
Li	0.677	1.000													
Na	0.645	0.822	1.000												
K	0.856	0.580	0.524	1.000											
Mg	0.793	0.850	0.902	0.736	1.000										
Ca	0.850	0.813	0.851	0.846	0.974	1.000									
Sr	0.823	0.828	0.893	0.790	0.992	0.992	1.000								
Ba	0.830	0.762	0.799	0.835	0.959	0.974	0.972	1.000							
Mn	0.160	0.438	0.333	0.188	0.329	0.257	0.290	0.327	1.000						
Fe	0.554	0.729	0.723	0.529	0.814	0.767	0.794	0.829	0.645	1.000					
Co	0.411	0.665	0.595	0.348	0.620	0.539	0.584	0.619	0.889	0.877	1.000				
Cu	0.543	0.872	0.833	0.542	0.786	0.769	0.781	0.690	0.254	0.637	0.465	1.000			
Zn	0.067	0.347	0.289	0.099	0.262	0.216	0.243	0.219	0.118	0.143	0.225	0.284	1.000		
Cd	0.728	0.951	0.705	0.643	0.770	0.761	0.760	0.722	0.500	0.689	0.681	0.803	0.265	1.000	
Pb	0.612	0.927	0.676	0.571	0.704	0.685	0.690	0.627	0.476	0.620	0.624	0.828	0.255	0.967	1.000
Al	0.775	0.953	0.843	0.705	0.931	0.916	0.920	0.883	0.346	0.779	0.615	0.878	0.283	0.913	0.867
Cr	0.665	0.944	0.657	0.576	0.698	0.687	0.684	0.647	0.409	0.606	0.596	0.802	0.303	0.965	0.950
As	0.099	0.474	0.461	-0.015	0.320	0.241	0.282	0.180	-0.116	0.097	0.060	0.449	0.379	0.267	0.318
Se	0.525	0.918	0.720	0.413	0.695	0.634	0.659	0.596	0.336	0.558	0.544	0.789	0.395	0.836	0.843
Mo	0.225	0.633	0.594	0.214	0.478	0.396	0.444	0.356	0.388	0.443	0.470	0.693	-0.026	0.608	0.729
U	0.398	0.430	0.652	0.288	0.592	0.563	0.609	0.542	0.002	0.449	0.293	0.501	0.003	0.325	0.301
F	-0.491	-0.039	-0.070	-0.559	-0.332	-0.432	-0.375	-0.490	0.043	-0.381	-0.122	0.011	0.376	-0.084	0.063
Cl	0.217	0.253	0.099	0.367	0.306	0.246	0.254	0.329	0.458	0.364	0.375	0.262	-0.041	0.305	0.333
Br	-0.058	0.310	0.260	-0.018	0.214	0.149	0.169	0.082	0.103	0.098	0.067	0.518	0.181	0.255	0.259
NO3	-0.325	-0.415	-0.406	-0.096	-0.345	-0.232	-0.293	-0.316	-0.636	-0.473	-0.670	-0.229	-0.181	-0.440	-0.409
PO4	-0.479	-0.697	-0.668	-0.431	-0.722	-0.665	-0.696	-0.740	-0.758	-0.950	-0.912	-0.569	-0.152	-0.678	-0.596
SO4	0.448	0.492	0.409	0.451	0.649	0.552	0.586	0.621	0.351	0.587	0.490	0.389	0.040	0.461	0.468
HCO3	0.806	0.828	0.887	0.763	0.990	0.983	0.993	0.965	0.291	0.804	0.594	0.772	0.255	0.752	0.680
SiO2	0.753	0.963	0.860	0.661	0.909	0.879	0.893	0.847	0.346	0.753	0.625	0.868	0.354	0.889	0.855
B	0.727	0.911	0.693	0.616	0.791	0.747	0.758	0.726	0.471	0.662	0.642	0.751	0.264	0.939	0.926

LEGEND	
	> 0.9
	> 0.8
	> 0.7
	> 0.6
	> 0.5
	> 0.4

	Al 27	Cr 52	As 75	Se 82	Mo 98	U 238	F	Cl	Br	NO3	PO4	SO4	HCO3	SiO2	B 11
Al	1.000														
Cr	0.885	1.000													
As	0.347	0.414	1.000												
Se	0.821	0.910	0.727	1.000											
Mo	0.573	0.634	0.321	0.629	1.000										
U	0.462	0.242	0.234	0.302	0.411	1.000									
F	-0.204	0.009	0.293	0.127	0.322	-0.152	1.000								
Cl	0.299	0.282	-0.120	0.228	0.387	-0.077	-0.114	1.000							
Br	0.265	0.239	0.261	0.307	0.272	0.150	0.200	0.313	1.000						
NO3	-0.338	-0.427	-0.126	-0.463	-0.378	-0.059	-0.149	-0.419	-0.004	1.000					
PO4	-0.715	-0.603	-0.086	-0.567	-0.417	-0.318	0.264	-0.367	-0.141	0.615	1.000				
SO4	0.573	0.412	0.100	0.424	0.463	0.238	-0.217	0.795	0.168	-0.426	-0.506	1.000			
HCO3	0.919	0.681	0.275	0.653	0.446	0.603	-0.362	0.260	0.179	-0.296	-0.698	0.608	1.000		
SiO2	0.967	0.902	0.515	0.899	0.595	0.449	-0.134	0.285	0.239	-0.404	-0.692	0.556	0.894	1.000	
B	0.906	0.916	0.307	0.837	0.617	0.233	-0.032	0.459	0.219	-0.536	-0.654	0.656	0.758	0.888	1.000

LEGEND	
	> 0.9
	> 0.8
	> 0.7
	> 0.6
	> 0.5
	> 0.4

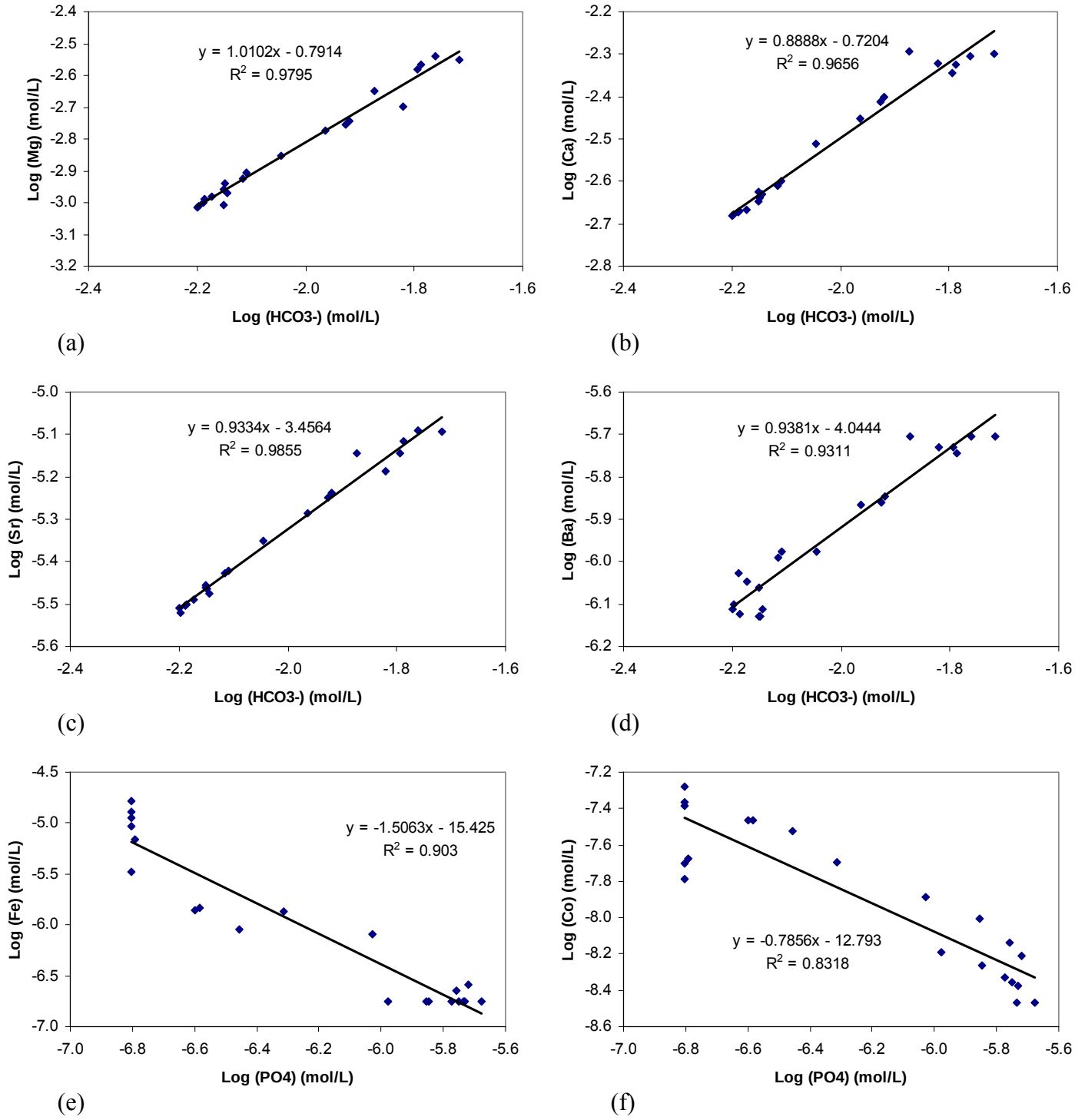

Figure 5.2. *Correlation plots showing relationships between various species in solution*

Figures 5.2a–d represent plots of the concentrations of the alkali earth metals with respect to alkalinity (reported as HCO_3^-), which shows a much stronger correlation than with H^+. Minimal scatter characterizes all four plots, even for Ba, which is present in micro-molar concentrations, and all regressions show linear correlations with slopes near unity. The trendlines of all alkali earth metal concentrations with respect to each other and with respect to alkalinity are also linear and extrapolate through the origin, suggesting a common source for all four metals. The correlations exhibited in Figures 5.2a–d cannot be attributed to complexing of the respective alkali earths by HCO_3^-, because an independent thermodynamic analysis demonstrates that the $MHCO_3^-$ complex (M = Mg, Ca, Sr, Ba) is present only as a minor species, the predominant species being M^{+2}. Equilibration with respect to a carbonate mineral according to the reaction

$$MCO_3 + CO_2(aq) + H_2O \Rightarrow M^{+2} + 2HCO_3^- \quad (5\text{-}1)$$

also cannot explain the unit slope positive correlation of log M with log HCO_3^-. Furthermore, the linear correlation between Mg and Ca yields a molar ratio, Mg/Ca of approximately 0.45, which, even for the most magnesian rich calcite, seems to be excessive (maximum observed values are approximately 0.25), and would imply that the observed secondary calcite precipitates at the MSU-ZERT site are proto-dolomites (Busenberg and Plummer, 1989). The perturbation of carbonate solubility according to the reaction

$$MCO_3 + H^+ \Rightarrow M^{+2} + HCO_3^- \quad (5\text{-}2)$$

is also not supported by the data, because correlations between all log M and pH are poor and non-stoichiometric. This is in part explained by the buffering effect that dissolved CO_2 has on pH according to the reaction:

$$CO_2(aq) + H_2O \Rightarrow HCO_3^- + H^+;\ pK \approx 6.5\ @\ 10°C \quad (5\text{-}3)$$

Finally, a comparison with Figure 5.5 (see Section 5.2.3 below) shows that significant resaturation of calcite started taking place only after the partial pressure of dissolved CO_2 exceeded 0.2 bar, which implies that calcite may not have been actively dissolving until that partial pressure had been exceeded. The linear trend observed between log (Ca^{+2}) and log (HCO_3^-) in Figure 5.2b suggests that Ca^{+2} was initially released from some source other than calcite, and that only later in the time period under investigation did calcite dissolution contribute significantly to the total dissolved Ca^{+2} in solution. This hypothesis is consistent with the argument that the increased acidity resulting from the dissociation of CO_2(aq) would depress the chemical potential of the CaO component in solution (defined in terms of log $[Ca^{+2}]/[H^+]^2$), and that this would have induced the release of Ca^{+2}, most probably from cation exchange sites, and concurrently through the dissolution of calcite.

The short-term and immediate response of the system to changes in alkalinity as demonstrated by these correlation plots can be best explained by ion exchange on the basis of the following arguments: (a) the strong correlation observed in Figures 5.2a–d and the inferred rapid response of the system to increasing alkalinity; (b) the linear relations between the log concentrations of the alkali earths and other divalent cations, suggesting a common source for all divalent cations, and even monovalent and trivalent cations; (c) the inferences drawn from the principal component analysis described below; (d) the close correlation of the geochemical modeling described in

Section 5.3 in which an ion exchange model, using independently derived ion exchange parameters, closely matches field measurements of pH against analytical data for the alkali earth metal and other divalent cation concentrations in solution; and (e) the mineralogical evidence for the presence of smectite in both vadose and phreatic zone sediments. We are led to the tentative conclusion that a shifting state of ion exchange equilibrium with respect to interlayer site occupancies on smectite may be responsible for the observed response of the groundwater composition to CO_2 uptake, although not necessarily driven exclusively by Ca^{+2} released by the dissolution of calcite. This process can be represented by the following equation, where X represents a negatively charged (-2) ion exchange site:

$$X\text{-}M(II) + 2H_2CO_3(aq) = X\text{-}H_2 + (M^{+2} \bullet 2HCO_3^-) \qquad (5\text{-}4)$$

Alkalinity (reported as HCO_3^-) is represented approximately by the concentration of HCO_3^- in this particular system (where minor complexation by HCO_3^- and the contribution due to CO_3^{-2} can be ignored). Therefore,

$$\log (HCO_3^-) \; \alpha \; ½\text{-}\log(M^{+2}) \qquad (5\text{-}5)$$

The trendlines in Figures 5.2a–d give slopes that approximate unity rather than 0.5, as would be expected from the above relationship. The observed correlation between alkalinity and the alkali earth metals is therefore not readily interpreted. Synthetic geochemical modeling of the response of a groundwater composition in equilibrium with a cation exchanger to changes in $P(CO_2)$ should be conducted to further elucidate the many complex system interactions that might explain the observed relationships.

Figures 5.2e and f show the negative correlations between phosphate (log PO_4), and log Fe and log Co, with trendline slopes of ~1.5 and 0.75, respectively. The correlation between log Fe and log PO_4 is strongly suggestive of an equilibrium state between these species and some ferrous phosphate mineral such as vivianite:

$$Fe_3(PO_4)_2.8H_2O = 3Fe^{+2} + 2PO_4^{-3}; \; \log [PO_4^{-3}] = K' + 3/2 \log[Fe^{+2}] \qquad (5\text{-}6)$$

Calculations show, however, that prior to CO_2 injection, the MSU-ZERT groundwaters were unsaturated with respect to both vivianite and strengite ($FePO_4.2H_2O$) prior to CO_2 injection. The slope coefficient of the trendline for cobalt could be explained by achievement of solution equilibrium with respect to the cobalt analogue of, for example, gormanite ($Fe^{II}{}_3Al_4(PO_4)_4(OH)_6 \bullet 2(H_2O)$), mclausanite ($HFe^{II}{}_3Al_2(PO_4)_4F \bullet 18(H_2O)$) or keckite $Ca(Mn,Zn)_2Fe^{III}{}_3(PO_4)_4(OH)_3 \bullet 2(H_2O)$, where:

$$\log [PO_4^{-3}] = K' + 3/4 \log[Co^{+2}] + \ldots, \text{ or } \log [PO_4^{-3}] = K' + 3/4 \log[Co^{+3}] + \ldots \qquad (5\text{-}7)$$

These examples are illustrative of the potential complexity associated with the mineralogy of shallow sedimentary systems. In reality, Co(II) is likely to substitute for Fe(II) in solid solution in Fe(II) hydroxides, such as green rust, but the presence of trace nanophases exercising solubility control over trace elements cannot be discounted, and insoluble phosphates might under some circumstance be potential candidates.

We now return to the correlation of the chemical species with a restricted set of principal components. Information on the first ten principal components is presented in Table 5.2. The first four principal components explain over 80% of the variance, whereas principal components No. 5 (PC5) and No. 6 (PC6) explain another 10%. As with Table 5.1, the correlation coefficients are similarly color coded in ranges 0.9, 0.8, 0.7, 0.6, 0.5 and also 0.4.

Table 5.2. *Principal components derived from an analysis of groundwater chemical compositions for the period July 7 to July 17, 2008*

Explained Variance (Eigenvalues)

Value	PC 1	PC 2	PC 3	PC 4	PC 5	PC 6	PC 7	PC 8	PC 9	PC 10
Eigenvalue	17.353	3.073	2.668	1.480	1.345	1.071	0.892	0.644	0.466	0.289
% of Var.	57.844	10.242	8.894	4.934	4.484	3.569	2.975	2.145	1.553	0.962
Cum. %	57.844	68.086	76.980	81.914	86.398	89.967	92.942	95.087	96.641	97.603

Component Loadings (correlations between initial variables and principal components)

Variable	PC 1	PC 2	PC 3	PC 4	PC 5	PC 6	PC 7	PC 8	PC 9	PC 10
H	0.774	-0.419	0.114	0.090	-0.289	-0.079	-0.111	0.051	0.279	0.018
Li	0.951	0.202	0.120	-0.010	-0.093	-0.063	0.071	-0.056	-0.026	0.086
Na	0.874	0.023	0.216	-0.246	0.223	-0.015	-0.064	0.062	0.113	-0.169
K	0.711	-0.500	0.071	0.245	-0.252	0.031	0.076	0.136	-0.005	-0.226
Mg	0.946	-0.215	0.111	-0.044	0.117	0.115	-0.059	0.029	-0.002	-0.002
Ca	0.914	-0.339	0.175	-0.014	0.018	0.062	0.023	0.051	-0.006	-0.070
Sr	0.931	-0.282	0.154	-0.060	0.084	0.077	-0.028	0.061	0.004	-0.044
Ba	0.902	-0.385	0.030	-0.053	0.025	0.127	-0.035	0.028	-0.032	-0.034
Mn	0.484	0.229	-0.735	-0.236	-0.001	-0.029	0.199	0.025	-0.033	-0.127
Fe	0.841	-0.169	-0.316	-0.257	0.156	0.019	0.088	-0.118	-0.164	0.044
Co	0.734	0.100	-0.537	-0.351	0.032	-0.015	0.077	-0.022	-0.070	0.045
Cu	0.857	0.201	0.275	0.113	0.176	-0.060	0.211	0.018	0.000	-0.116
Zn	0.282	0.372	0.221	-0.287	-0.268	0.663	0.076	0.317	-0.098	0.051
Cd	0.914	0.156	-0.013	0.080	-0.234	-0.173	0.163	0.030	0.044	0.119
Pb	0.872	0.287	0.007	0.155	-0.184	-0.233	0.109	0.089	-0.060	0.060
Al	0.972	-0.021	0.131	0.055	-0.054	-0.019	0.066	-0.004	-0.043	0.065
Cr	0.872	0.276	0.070	0.116	-0.298	-0.164	0.079	-0.061	-0.007	0.068
As	0.352	0.482	0.529	-0.105	0.044	0.174	-0.330	-0.410	-0.073	-0.109
Se	0.832	0.417	0.189	0.013	-0.142	0.001	-0.115	-0.228	-0.020	0.005
Mo	0.620	0.441	-0.058	0.196	0.313	-0.411	-0.150	0.166	-0.145	-0.143
U	0.497	-0.203	0.325	-0.258	0.562	-0.203	-0.126	0.194	0.086	0.208
F	-0.201	0.870	0.095	-0.056	0.047	0.006	-0.108	0.368	0.004	-0.045
Cl	0.385	0.035	-0.573	0.615	0.168	0.257	-0.102	0.029	-0.021	-0.081
Br	0.252	0.387	0.148	0.340	0.464	0.286	0.497	-0.140	0.275	0.046
NO3	-0.477	-0.303	0.547	0.195	0.083	-0.056	0.352	0.005	-0.431	0.026
PO4	-0.791	0.034	0.434	0.310	-0.094	-0.030	-0.125	0.165	0.027	0.012
SO4	0.631	-0.104	-0.347	0.406	0.217	0.245	-0.359	0.014	-0.153	0.179
HCO3	0.928	-0.271	0.141	-0.061	0.099	0.097	-0.032	0.065	-0.014	-0.007
SiO2	0.967	0.079	0.165	0.002	-0.079	0.028	-0.056	-0.076	-0.043	-0.009
B	0.910	0.172	-0.084	0.202	-0.223	-0.045	-0.061	0.031	0.038	0.107

LEGEND	
	> 0.9
	> 0.8
	> 0.7
	> 0.6
	> 0.5
	> 0.4

With respect to principal component No. 1 (PC1), nine of the chemical species show correlations of 0.9 and above, and another six show correlations between 0.8 and 0.9. With the exception of HCO_3,

Li and Na, all of the remainder are probably present as divalent cations or divalent hydroxy-cations of trivalent species, i.e., B, Al, Cr, and Mn. Principal component No. 2 (PC2) correlates strongly only with F, and relatively weakly with As, Se and Mo, all potential oxy-anionic species, and inversely, but weakly with H and K. Principal component No. 3 (PC3) inversely correlates with Mn, Co and Cl, and directly with As, NO_3 and PO_4. Principal component No. 4 (PC4) correlates with Cl and SO_4. Correlations of chemical species with the remaining six components are for the most part weak and are of questionable significance.

Interpretation

Each of the primary principal components most probably relates to a chemical process that takes place rapidly, given the short interval over which the analyses were taken, and considering the fact that a close logarithmic relationship is observed with respect to HCO_3^- in the first principal component. The most likely short term processes are, in order of reaction rate: adsorption/desorption, ion exchange (both cationic and anionic), dissolution of carbonates and metastable Fe hydroxides and green rusts, some homogeneous redox reactions in the aqueous phase, and pore water infiltration from the vadose zone. Other unidentified processes may also be involved, which future investigations might reveal.

Table 5.3 lists the correlated variable for each of the first six principal components, and identifies the likely processes in which the dominant aqueous species might participate. Note that over the possible range of redox states in the shallow phreatic zone at the ZERT site, several aqueous species might transform to other species with different oxidation states, notably Fe(III)/Fe(II), Cu(II)/Cu(I), Cr(VI)/Cr(III), N(VII)/N(0), U(VI)/U(IV), Se(VI)/Se(IV)/Se(-II). It is also possible, although less likely, that extremely reducing conditions might arise through the progressive decomposition of organic matter, leading to transformations with respect to As(III)/As(-I), S(VI)/S(-II), Mo(VI/Mo(II), C(IV)/C(0)/C(-IV), and N(0)/N(-III). It should also be noted that many trace elements could be present in solid solution in minerals that are known to dissolve rapidly in response to changing pH, such as calcite and/or hydroxide minerals including green rust. These have not been checked in Table 5.3 under "Precipitation/dissolution," because the extent of such solid solutions is unknown.

Table 5.3 suggests that PC1 may be related to ion exchange or desorption processes because the alkali earth metals and other divalent cations correlate very strongly with this component. Several monovalent cations (H^+, Li^+, Na^+, K^+) are also moderately to strongly correlated. These correlations suggest cation exchange on smectite interlayer sites. Trivalent species such as B, Al, Fe and Cr, and tetravalent Si (as $SiO_2(aq)$) are also moderately to strongly correlated, and are known to sorb onto clays. However, the strong positive correlation with HCO_3^- is not readily explained in relation to sorption or ion exchange on smectite. Other oxy-anionic species, such as SO_4^{-2}, Mo (as MoO_4^{-2}), Se (as SeO_4^{-2} or SeO_3^{-2}) are also positively correlated. It is tempting to assume that these species likely occupy the interlayer sites of anionic clays such as fougerite, a Mg-rich form of green rust, especially when it is recognized that such occupancy in green rust has been confirmed in the laboratory for all but MO_4^{-2}. However, the oxy-anions, PO_4 an NO_3, are negatively correlated, implying a different association with PC-1, which is not readily explained without further study.

PC2 appears to be dominated by anionic species (F, As (probably as $HAsO_4^{-2}$), Se (as SeO_4^{-2} or SeO_3^{-2}) and Mo (as MoO_4^{-2}), which are positively correlated, and by H and K, which are negatively correlated, and suggest adsorption on hydrous ferric oxide (HFO), which could be ferrihydrite,

lepidocrocite, or goethite. PC3 shows a negative correlation with respect to Mn, Co and Cl, and a positive correlation with respect to As (probably as $HAsO_4^{-2}$), NO_3 and PO_4. This correlation is suggestive of saturation control by some transition metal phosphate with substitution of AsO_4^{-3} for PO_4^{-3}. PC4 may be related to infiltration of pore water from the overlying vadose zone. U is correlated with PC5 and Zn appears to show the strongest correlation by far with PC-6. No explanation for these correlations is apparent. The behavior of Zn appears to be unique, and is unexpected.

Because smectite has been identified as a mineral that is present in the sediments in the saturated zone, it is reasonable to assume as a working hypothesis that ion exchange on smectite is operative, and is responsible for the species correlations observed with respect to PC1. It is not entirely clear, though, what specific ion exchange mechanism is taking place. Increasing H^+ caused by the dissolution of CO_2 might be responsible. However, the correlation between H^+ and the first principal component is only moderate, and as noted in preceding discussions, does not explain the strong positive correlation with HCO_3^-. Another possibility is that increased $P(CO_2)$ leads to calcium carbonate dissolution, which in turn induces ion exchange with other divalent cations observed to increase in concentration in the groundwater. This mechanism would therefore be controlled by the rate of calcite dissolution. As a working hypothesis, we will assume that the primary response to increasing concentrations of dissolved CO_2 is cation exchange and desorption induced by Ca^{+2} due to calcite dissolution, and anion exchange induced by increasing HCO_3^- in solution. We will also assume that an adsorbent is present whose surface behaves analogously to HFO such as ferrihydrite, or other ferric oxy-hydroxides and other metastable phases (e.g., schwertmannite and green rust) commonly resulting from the transformation of HFO (see further discussion in Section 5.2.2). The presence of these minerals can also provide anionic exchange sites as suggested by the correlation between PC1 and PC2 with respect to aqueous anionic species. The modeling of this system is presented subsequently in Section 5.3 of this report.

Table 5.3. *Correlation of aqueous species with principal components for the period July 7 to July 17, 2008 in relation to short-term chemical processes*

Component	Variable	Correlation	Dominant Aqueous Species	Cation Exchange	Anion Exchange	Adsorption	Precipitation/ dissolution	Redox Reactions	Infiltration
1	H	0.774	H^+	√		√			
	Li	0.951	Li^+	√		√			
	Na	0.874	Na^+	√		√			
	K	0.711	K^+	√		√			
	Mg	0.946	Mg^{+2}	√		√	√		
	Ca	0.914	Ca^{+2}	√		√	√		
	Sr	0.931	Sr^{+2}	√		√			
	Ba	0.902	Ba^{+2}	√		√			
	Mn	0.484	Mn^{+2}	√		√		√	
	Fe	0.841	Fe^{+2}	√		√	√	√	
	Co	0.734	Co^{+2}	√		√	√		
	Cu	0.857	Cu^{+2}/Cu^+	√		√		√	
	Cd	0.914	Cd^{+2}/CdSe	√		√			
	Pb	0.872	$PbCO_3$/PbSe	√		√			
	Al	0.972	$Al(OH)_3$-H_3SiO_4-	?	?	√	√		
	Cr	0.872	CrO_4^{-2}/CrO^+	?	√	√	√		
	Se	0.832	SeO_4^{-2}		√	√		√	
	Mo	0.620	MoO_4^{-2}			√			
	U	0.497	$UO_2(CO_3)_2^{-2}/UO_2$			√		√	
	NO3	-0.477	NO_3^-		√	√		√	√
	PO4	-0.791	H_2PO_4-		√	√			
	SO4	0.631	SO_4-2		√	√		√	√
	HCO3	0.928	HCO_3^-		√	√	√	?	
	SiO2	0.967	$Si(OH)_4$			√	√		
	B	0.910	$B(OH)_3$			√			
2	H	-0.419	H+	√		√			
	K	-0.500	K^+	√		√			
	As	0.482	AsO_3F^{-2}		√	√		?	
	Se	0.417	$SeO_4^{-2}/HseO_3^-$		√	√		√	
	Mo	0.441	MoO_4^{-2}		√			?	
	U	-0.203	$UO_2(CO_3)_2^{-2}/UO_2$			√		√	
	F	0.870	F^-		√				
3	Mn	-0.735	Mn^{+2}	√		√		√	
	Co	-0.537	$CO_2(OH)_3^+$	√		√			
	As	0.529	AsO_3F^{-2}			√		?	
	Cl	-0.573	Cl^-		√				√
	NO3	0.547	NO_3^-		√				√
	PO4	0.434	$H_2PO_4^-$		√	√			
4	Cl	0.615	Cl-						√
	SO4	0.406	SO_4^{-2}						√
5	U	0.562	$UO_2(CO_3)_2^{-2}/UO_2$			√		√	
	Br	0.464	Br^-						√
6	Zn	0.663	Zn^{+2}	√		√			
	Mo	-0.411	MoO_4^{-2}		√	√		?	

5.2.2 Thermodynamic Evaluation of Baseline Groundwater Composition and Redox State

One of the more difficult problems associated with interpreting the geochemistry of the groundwaters in the saturated zone at the ZERT Site is the determination of the redox state. In addition, as discussed further below, it has been clearly established that complete redox equilibrium in shallow groundwater systems is rarely, if ever, achieved (e.g., Lindberg and Runnels, 1984; Washington et al., 2004; Stefansson et al., 2005). Furthermore, many of the trace elements and some of the major constituents can undergo reduction or oxidation in response to periodic infiltration of rainfall, which transports not only dissolved constituents already present in the rain (Na^+, Mg^{+2}, Ca^{+2}, NH_4^+, HCO_3^-, NO_3^-, SO_4^{-2}, Cl^-, Br^-), which have been subject to evapo-transpiration, but also dissolved inorganic constituents and organic matter from the overlying soil zone. The transported organic matter is present both in the form of dissolved organic acids and associated complexes with inorganic cations, but also is probably present in colloidal form. Both during transport and after reaching the water table, the organic matter in the pore waters undergoes oxidative mineralization through the agency of bacteria and fungal matter, depleting all dissolved and gaseous phase oxygen in the vadose and phreatic zones, and then reducing both dissolved and solid-phase electron donors. These include N(V) as NO_3^-, N(III) as NO_2^-, N(0) as N_2, S(VI) as SO_4^{-2}, and dissolved minor elements and trace metals involving species and complexes and associated solid phases in the following oxidation states; C(IV)/C(0)/C(-IV), Fe(III)/Fe(II), Mn(IV)/Mn(III)/Mn(II), As(V)/As(III)/As(-I)/As(-III), Se(VI)/Se(IV)/Se(0)/Se(-II), Cr(VI)/Cr(III), Co(III)/Co(II), Cu(II)/Cu(I), Mo(VI)/Mo(II) and U(VI)/U(IV).

The traditional approach taken in trying to characterize the redox state of groundwaters is through the use of a platinum (Pt) electrode and associated reference electrode, e.g., calomel or Ag/AgCl, which measures the redox potential of the groundwater when in thermodynamic equilibrium. However, as noted above, shallow groundwaters are rarely if ever at thermodynamic equilibrium, and therefore the measured mixed potential cannot be utilized as a meaningful representation of the redox potential. Furthermore, a Pt electrode can locally catalyze redox reactions on its surface, leading to precipitation of PtO, which, in combination with the Pt substrate, results in it responding to pH rather than Eh (see Baas Becking, 1960). The Pt electrode can also be poisoned. Thus, unless great precaution is taken, the measured potential may have more to do with the electrode sensor than the solution in which it is immersed.

The problems associated with direct *in situ* measurement of redox potential using a Pt electrode have been known for many years (Baas Becking, 1960). Following Lindberg and Runnels (1984), therefore, attempts have been made to chemically analyze dissolved redox pairs in groundwaters (e.g., Washington et al., 2004; Stefansson et al., 2005), and then calculate the apparent redox potential for each pair. As expected, the analyzed redox pairs yield disparate redox "potentials." indicating a nonattainment of homogeneous equilibrium. Washington et al. (2004) made a significant contribution, when they showed that the potentials associated with the analyzed redox pairs are not random, but behave in a systematic manner, and that "…redox couples composed of concentrated reactants achieve nearly thermodynamic equilibrium concomitantly, and those with dilute reactants deviate from equilibrium by an amount roughly inverse to their concentrations." In typical groundwaters, an upper group of redox couples is essentially controlled by the presence of NO_3, which is involved in the oxidation of species such as, for example, Fe(II), thus:

$$NO_3^- + 2Fe^{+2} + 5H_2O \rightarrow NO_2^- + 2Fe(OH)_3(ppt) + 4H^+ \qquad (5\text{-}8)$$

and a lower group controlled by the presence of dissolved organic matter, which can be represented by equations of the type:

$$3CH_2O + 2H^+ + SO_4^{-2} \rightarrow H_2S(aq) + 2CO_2(aq) + 2H_2O \ , \qquad (5\text{-}9)$$

where CH_2O is a generic representation of dissolved (and particulate) organic matter. According to Washington et al. (2004), the upper cluster of redox pairs is centered on pe ≈ +10, whereas the lower cluster is centered on pe ≈ -2. Over time, or with increasing depth below the water table, all NO_3 in solution is progressively consumed, and the redox pairs, initially in local partial equilibrium with respect to NO_3, drift to lower redox states, where control of the redox state is assumed by the reservoir of organic matter and microbial activity, which is usually the dominant reducing agent in shallow unconfined aquifers underlying soil zones with active vegetative cover. This scenario is particularly pertinent to the redox state of the ZERT site, as is described further below.

While the direct characterization of redox pairs represents the most rigorous means of characterizing the redox state in a groundwater, such an approach is rarely implemented in practice, because it requires elaborate sampling procedures to avoid inadvertent contamination by atmospheric oxygen, and time-consuming and expensive analytical procedures. A more typical scenario is represented by the current characterization of the ZERT site and elsewhere—e.g., see Bourrie et al. (1999) and Feder et al. (2005)—where collected groundwaters are subjected to standard field and laboratory analytical procedures, and where only the total concentrations of elements in solution are determined rather than their speciation, including the distribution of species between oxidation states.

An alternative means of indirectly characterizing the oxidation state of a groundwater is through a thermodynamic analysis of the groundwater composition using a distribution of species code such as PHREEQC (Parkhurst and Appelo, 1999) or EQ3/6 Wolery, 1992, 1993) and calculating the saturation states of minerals that might control the redox state of the system by varying the redox potential over a specified range and examining at what pe (or Eh) potential redox controlling minerals equilibrate with the redox affected aqueous species in solution. Ideally, the redox state can be established where one or more redox sensitive phases containing the same redox pair coexist in a state of saturation at a particular value of pe. Such an analysis is in some respects more fundamental, in that solid phases participating in redox reactions are likely to exert a substantial buffering capacity on the system as a whole, and are more likely to define a temporally averaged redox state, rather than a momentary, but not necessarily representative oxidation state characterized by the analysis of an isolated groundwater sample. Such utilization of redox sensitive minerals to help define the oxidation state of an aqueous system is subject to several limitations and caveats:

1. The redox sensitive phases must be reactive, i.e., they must be able to respond by dissolving or precipitating sufficiently rapidly, so that they reasonably approach thermodynamic equilibrium under ambient conditions. Such phases are most likely to be metastable and either finely crystalline or amorphous.
2. The redox sensitive phases must be clearly identified, and their thermodynamic properties reasonably well characterized.
3. Ideally, several redox sensitive components should be considered in the analysis in order to provide independent corroboration.

4. The participating aqueous species must be present at sufficiently high concentrations to be detectable and quantifiable in solution.
5. Groundwater sampling procedures exclude contamination, and custodial integrity can be assumed (i.e., samples have not re-equilibrated under post-sampling redox conditions).
6. The thermodynamic properties of the aqueous species must be known and their complexation with other species in solution must be known and quantified.
7. Suitable corrections to the thermodynamic data used in the analysis should be made to account for ambient field temperatures of 10ºC rather than the standard reference temperature of 25ºC used in most thermodynamic calculations concerning groundwaters.
8. Validation of the thermodynamic analysis should be made through an independent mineralogical study of the abundance and distribution of redox sensitive phases in the soil/sediment profile through the vadose and phreatic zones where the groundwaters were sampled.

In the following analysis, a modified EQ3/6 thermodynamic database was used as described in Birkholzer et al. (2008). The database is a substantial revision of an earlier database, Data0. ymp.R4, which was developed and qualified for use by the Yucca Mountain Project on behalf of the U.S. Department of Energy. A very important requirement for conducting a successful thermodynamic evaluation of the ZERT site is the incorporation of the solubility products of metastable redox sensitive minerals that might exercise partial or complete secular control over the redox state of the system. Among these is a class of minerals referred to as "green rusts" of which fougerite is the most important naturally occurring representative. Because this mineral is unstable under oxic conditions, its recovery and preservation during coring for soil and sediment samples is questionable unless appropriate precautions are taken to avoid contamination with atmospheric oxygen. Despite the fact that such precautions were not anticipated or implemented, circumstantial evidence suggests that it may be present at the ZERT site, and some geochemical similarities between the ZERT site and the type locality for fougerite in Brittany mandate that it be taken into consideration in the following thermodynamic evaluation. (By "type locality", we refer to the original site from which the fougerite was initially obtained, characterized mineralogically, and reported in the scientific literature.) Appendix C presents a summary description regarding the known thermodynamic properties of fougerite and its compositional variation, as cited in the recent literature, and describes the procedure adopted for calculating its solubility product in a form appropriate for inclusion in Data0.ymp.R4.

Baseline Groundwater Composition

The groundwater composition selected for evaluation of the redox state is based on the average of seven comprehensive chemical analyses of groundwaters taken on July 7 and 8, 2008, immediately prior to CO_2 injection. With the exception of sample 08ZERT-104, all samples were taken from the deeper A-wells and from two monitoring wells drilled further away from the injection well (MW1 and MW2). It is possible that a redox gradient exists between the water table and deeper horizons within the phreatic zone, and that sample 08ZERT-104 may reflect more oxidizing conditions. However, the chemical analysis does not support this interpretation, and even suggests a lower redox potential induced by exogenic contamination, as is noted further below. These analyses and the average values are given in Table 5.4.

Table 5.4 *Initial composition of the groundwater at the ZERT site prior to CO_2 injection*

SAMPLE	T	pH	Li	Na	K	Mg	Ca	Sr	Ba	Mn	Fe
	°C		mg/L	mg/L	mg/L	mg/L	mg/L	mg/L	mg/L	mg/L	mg/L
08ZERT-**102**	10	6.8	0.003	7.5	6.2	24	85	0.27	0.13	0.002	<0.01
08ZERT-**103**	10	6.8	0.003	9.2	5.5	24	95	0.31	0.12	0.001	<0.01
08ZERT-**104**	15	6.9	0.006	9.7	5.6	27	90	0.30	0.10	0.11	0.05
08ZERT-**105**	8	6.9	0.003	7.8	5.6	23	84	0.27	0.11	0.001	<0.01
08ZERT-**106**	8	6.9	0.004	8.1	5.6	25	86	0.28	0.10	0.31	<0.01
08ZERT-**107**	8	6.7	0.005	7.5	5.3	24	84	0.26	0.11	0.001	<0.01
08ZERT-**109**	12	7.0	0.007	9.1	5.4	28	92	0.30	0.10	0.028	<0.01
Average	10.286	6.871	0.004	8.414	5.583	24.992	87.988	0.285	0.110	0.065	0.015

SAMPLE	Co	Cu	Zn	Cd	Pb	Al	Cr	As	Se	Mo	U
	ug/L	*ug/L*	*ug/L*	*ug/L*	*ug/L*	*ug/L*	*ug/L*	*ug/L*	*ug/L*	*ug/L*	*ug/L*
08ZERT-**102**	<0.2	1.4	3.4	0.07	<0.02	2	<0.4	0.8	<2	0.4	4.3
08ZERT-**103**	0.3	1.5	4.0	0.09	<0.02	2	0.4	1.0	<2	0.3	4.9
08ZERT-**104**	0.8	2.4	2.4	0.26	0.08	3	10	1.0	<4	1.3	4.5
08ZERT-**105**	<0.2	1.2	2.8	0.08	0.02	2	<0.4	0.9	<2	0.4	4.0
08ZERT-**106**	0.6	1.1	3.2	0.10	0.02	2	<0.4	0.8	<2	0.3	4.0
08ZERT-**107**	0.2	1.6	3.1	0.23	0.05	3	12	1.0	<4	0.4	4.1
08ZERT-**109**	0.4	2.5	3.8	0.29	0.06	3	12	1.3	5	0.7	4.3
Average	0.376	1.668	3.245	0.162	0.038	2.383	5.010	0.976	3.003	0.545	4.291

SAMPLE	F	Cl	Br	NO3	PO4	SO4	HCO3	SiO2	B 11
	mg/L	mg/L	mg/L	mg/L	mg/L	mg/L	mg/L	mg/L	mg/L
08ZERT-**102**	0.09	6.5	0.051	0.12	0.20	8.3	396	27	0.012
08ZERT-**103**	0.10	3.7	0.042	0.79	0.17	5.8	432	27	0.009
08ZERT-**104**	0.17	5.3	0.046	0.10	0.09	7.3	431	33	0.017
08ZERT-**105**	0.10	4.7	0.040	0.55	0.17	7.5	386	26	0.012
08ZERT-**106**	0.11	5.1	0.044	0.19	0.13	7.4	398	26	0.013
08ZERT-**107**	0.12	4.8	0.042	0.60	0.18	7.4	387	32	0.018
08ZERT-**109**	0.17	5.4	0.099	0.26	0.10	7.2	434	32	0.017
Average	0.123	5.071	0.052	0.373	0.149	7.270	409.129	28.931	0.014

In general, most of the major chemical constituents and trace elements show relatively consistent values, giving one confidence that the analyses truly reflect the actual concentrations present in the groundwater. However, several species of critical interest in defining the oxidation state of the groundwater and the saturation state of redox sensitive phases are at or close to their detection limits. These include Mn, Fe, Cr and Se. Furthermore, sample 08ZERT-104 shows anomalously high concentrations of Fe, Cu, Cd, Cr and Mo, suggesting contamination by steel. The averaged concentrations should therefore be considered as maximum values in interpreting the subsequent results. However, it should also be noted that these same species show variations in concentrations subsequent to CO_2 injection that place them well within the range of detectability for the analytical methods used.

Thermodynamic Analysis of Baseline Groundwater

The average concentrations of the chemical species given in Table 5.4 were entered into the input file of EQ3/6, and an initial run was made to calculate the extent of complexation by HCO_3^- at 25ºC. The analytical value for HCO_3^- was adjusted to account for cation complexation, and the revised value inserted as a "free" concentration. In this manner, the total equilibrium concentration of all carbonate species, including CO_2(aq), can be accounted for in solution, and P(CO_2) determined. EQ3/6 was then re-run, setting the temperature to the average ambient value of 10.28ºC. The resulting charge imbalance was calculated to be –0.50% of the mean charge of all charged species, which is excellent, and therefore no attempt was made to ensure electrical neutrality by balancing on any selected species.

The calculated saturation indices (SI) for several primary and secondary minerals of interest, but which are not sensitive to the redox state of the system, are listed in Table 5.5. The saturation indices of aluminosilicate minerals have been normalized to both Al and Si to afford a better respective comparison with the gibbsite ($Al(OH)_3$) and silica (opal-CT or quartz) chemical components. These results are typical of what would be expected in a soil zone of this type, where primary rock-forming minerals associated with detrital igneous, metamorphic, and sedimentary rock fragments observed in the shallow subsurface environment at the ZERT site are weathering in the presence of neutral to weakly acid groundwaters containing dissolved organic matter from the overlying soil zone. The aluminum concentration is elevated and actually supersaturated with respect to gibbsite, which is consistent with field observations elsewhere (Dobrzynski, 2007), and is caused by the formation of metastable amorphous or poorly crystalline hydroxy-aluminum silicates (HAS) such as imogolite or allophane as weathering products of detrital minerals of igneous or metamorphic provenance. These HAS minerals are also closely associated with secondary opal-CT, which forms concurrently in systems with excess silica. Recent work has shown that HAS minerals form as metastable precursors to secondary minerals actually observed in the fine fractions of sediments recovered from the site, i.e., smectite, illite, and kaolinite. The transformation from HAS to these secondary clays is exceedingly slow, and therefore the former, together with opal-CT, controls the activity of $Al(OH)_3$ and SiO_2 components in the aqueous phase. As a result, the weathering minerals can approach thermodynamic equilibrium, and indeed, secondary epitaxial overgrowths of K-feldspar on detrital feldspar grains have sometimes been observed.

The groundwater at the ZERT site does not appear to be saturated with respect to either HAS or to opal-CT. Calcite also appears to be undersaturated, with SI(calcite) = -0.283. Given the fact that secondary calcite precipitates are ubiquitous both below and above the water table at the ZERT site (Section 4), it is perhaps surprising that it is not closer to saturation. Furthermore, mineralogical studies of secondary calcite suggest that it may be magnesium rich. Such calcites are less stable than the pure form (Busenberg and Plummer, 1989), which would imply even greater degrees of undersaturation. However, undersaturation with respect to HAS, opal-CT and calcite can be explained by transient dilution of the groundwater due to rainfall prior to the start of the test. Table 5.5 shows that all of the listed potential secondary phyllosilicates except celadonite, including those actually observed to be present in sediments at the ZERT site, are supersaturated, as expected. The supersaturation of K-feldspar is consistent with some observations elsewhere (Zhu et al., 2006), but may be related to potassium retention by vegetation in the presence of illite, rather than any thermodynamic or kinetic control by this mineral, especially when it is recognized that the pH is ≤7. The observed undersaturation with respect to low albite is expected.

Table 5.5 also lists the saturation indices of some other minerals of passing interest. Dolomite is strongly undersaturated, as is characteristic of shallow groundwaters (Edmunds et al., 1982; Back et al., 1983; Hopkins and Putnam, 2000; James et al., 1993; Pacheco and Szocs, 2006), and therefore dolomite, if present, would tend to dissolve. As mentioned in Section 4, individual grains of detrital dolomite and occasional fragments of dolomitic limestone were identified in the coarse fractions of sediments from the ZERT site. This material shows evidence of corrosion, which is consistent with the findings of the thermodynamic analysis. Earlier work (Birkholzer et al., 2008) involving the thermodynamic evaluation of 38,000 potable groundwaters showed that the concentration of Ba was controlled primarily with respect to barite ($BaSO_4$). Table 5.5 shows that barite is significantly undersaturated with respect to both barite and to alstonite, the barium analogue of dolomite. This finding is also suggestive of dilution by rainfall, preventing the accumulation of the products of weathering to saturate, except possibly after prolonged dry spells. Finally, the saturation indices of hydroxy-apatite, fluor-apatite and crandallite are compared. Hydroxy-apatite is strongly under-saturated, whereas fluor-apatite is strongly supersaturated. Many of the detrital lithic fragments at the ZERT site consist of amphibolites or extrusive mafic rocks including andesitic volcanics. These rocks typically contain apatite, commonly with significant F^- substitution for OH^-. Therefore, it is possible that the shallow groundwaters may be saturated with respect to hydroxy-fluor apatite. It is more likely, however, that apatite is unstable with respect to secondary crandallite, which is close to saturation. Other alkali-earth metals such as Sr and Ba, and also Pb and Cd are known to substitute for Ca, and AsO_4^{-3}, VO_4^{-3}, CO_3^{-2}, MoO_4^{-2}, SO_4^{-2}, SeO_4^{-2} and even CrO_4^{-2} can substitute for PO_4^{-3} in the crandallite crystal structure. Fe^{+3} and Cr^{+3} can also substitute for Al^{+3} in crandallite—see Schwartz, et al. (2000). Therefore, this mineral or an isostructural mixed phosphate-sulfate, woodhouseite ($CaAl_3(PO_4)(SO_4)(OH)_6$), could exercise partial thermodynamic control over the activities of a number of trace elements in the groundwater.

Table 5.5. *Saturation indices of redox-insensitive primary and secondary minerals with respect to groundwater at the ZERT site*

Name	Formula	SI	SI(n. Al)	SI(n. Si)
Quartz	SiO2	+0.633	-	+0.633
Opal-CT	SiO_2	-0.267	-	-0.267
Gibbsite	$Al(OH)_3$	+0.402	+0.402	-
Hydroxy Aluminum and Magnesium Silicates				
Imogolite	$Al_2SiO_5.xH_2O$	-0.897	-0.448	-0.897
Hydroxy aluminium silicate	$Al_2Si_2O_5(OH)_4$	-2.310	-1.155	-1.155
Kaolinite	$Al_2Si_2O_5(OH)_4$	+2.440	+1.220	+1.220
Talc	$Mg_3Si_4O_{10}(OH)_2$	-5.540	-	-1.385
Clinochlore	$Mg_5Al_2Si_3O_{10}(OH)_8$	+2.332	+1.166	+0.777
Pyrophyllite	$Al_2Si_4O_{10}(OH)_2$	+1.919	+0.959	+0.480
Smectites				
Beidellite-Ca	$Ca_{0.165}Al_{2.33}Si_{3.67}O_{10}(OH)_2$	+2.206	+0.947	+0.601
Smectite-Ca	$Ca_{0.145}Mg_{0.26}Al_{1.77}Si_{3.97}O_{10}(OH)_2$	+4.639	+2.621	+1.169
Montmorillonite-Ca	$Ca_{0.165}Mg_{0.33}Al_{1.67}Si_4O_{10}(OH)_2$	+2.175	+1.302	+0.544
Phengites				
Celadonite	$KMgAlSi_4O_{10}(OH)_2$	-0.355	-0.355	-0.089
Illite	$K_{0.6}Mg_{0.25}Al_{1.8}Al_{0.5}Si_{3.5}O_{10}(OH)_2$	+1.647	+0.716	+0.544
Feldspars				
K-feldspar	$KAlSi_3O_8$	+1.009	+1.009	+0.336
Albite-low	$NaAlSi_3O_8$	-1.887	-1.887	-0.629
Carbonates				
Calcite	$CaCO_3$	-0.283	-	-
Dolomite	$CaMg(CO_3)_2$	-3.196*	-	-
Alstonite	$BaCa(CO_3)_2$	-2.435	-	-
Phosphates				
Hydroxy-apatite	$Ca_5(OH)(PO_4)_3$	-4.992	-	-
Fluor-apatite	$Ca_5(F)(PO_4)_3$	+5.721	-	-
Crandallite	$CaAl_3(PO_4)(OH)_5.H_2O$	-0.230	-0.077	-
Sulfates				
Barite	$BaSO_4$	-0.440	-	-

** Solubility product is based on data reported by Rock et al. (2001)*

To evaluate redox sensitivities, EQ3/6 was re-run specifying the redox state at successive increments ranging from –2 to +14 in units of pe (-log[e-]) (mol/kg H_2O) at 2-unit pe intervals. The

principal aqueous species of Fe, Mn and selected trace elements are displayed for each pe increment in Table 5.6. Note that Mn, Co, Cd, Pb and Zn remain in the (II) state throughout the range of pe's investigated. However, solid Mn and Fe phases coexisting with aqueous Mn and Fe do show changes in oxidation state. The dominant speciation for Pb and Zn also changes under strongly reducing conditions. Changes in aqueous speciation associated with changes in oxidation state are observed for Fe, Cu, Cr, Se, U, and NO_3, but changes are not observed with respect to As, which remains in the As(V) state, and S (as SO_4), which remains in the S(VI) state, although reducing conditions are likely to stabilize As(O), As(-I), As(-II), S(-I), and S(-II), respectively.

The candidate elements that show the most potential for identifying redox controls over the expected range of values at the ZERT site appear to be Mn, Fe, Cr, Cu and Se. In the following evaluation, only Fe and Mn are addressed. The behavior of Cr, Cu, and Se are addressed in Appendix D. In this evaluation, the concentrations of all species in solution are held constant, in conformity with the average composition given in Table 5.4, regardless of the oxidation state specified by the pe. The calculations assume complete homogeneous equilibrium with respect to the groundwater, and the saturation index (SI) for each redox-sensitive solid phase is calculated. If the trend of calculated SI's of a given redox-sensitive phase as a function of pe intersects the zero axis, i.e., SI = 0, then that phase is in equilibrium with the groundwater at the pe where SI = 0, regardless of the number of essential redox-sensitive components constituting that phase. For example, consider the mineral bornite (Cu_5FeS_4) (Appendix D, Figure D.2). In this mineral, all three elements can take up different equilibrium oxidation states in solution, depending on pe, as is illustrated in Table 5.6, i.e., Cu(II)/Cu(I), Fe(III)/Fe(II) an S(VI)/S(-II). The translation equation defining the solubility product of bornite in Data0.ymp.R4 of EQ3/6 is given by:

$$Cu_5FeS_4 + 4H^+ = Cu^+ + Cu^{+2} + Fe^{+2} + 4HS^- \quad (5\text{-}10)$$

Each redox-sensitive species is also related to the primary basis redox-sensitive species by other translation equations defining the appropriate dissociation constants relating redox pairs, thus:

$$Cu^+ + H^+ + 1/4O_2(g) = Cu^{+2} + 1/2H_2O \quad (5\text{-}11)$$

$$Fe^{+3} + 1/2H_2O = 1/4O_2(g) + Fe^{+2} + H^+ \quad (5\text{-}12)$$

$$HS^- + 2O_2(g) = SO_4^{-2} + H^+ \quad (5\text{-}13)$$

where

$$O_2(g) + 4H^+ + 4e^- = 2H_2O; \quad (5\text{-}14)$$

$$pe = \log K' + \log \frac{[O_2(g)]^{1/2}[H^+]}{[H_2O]^{1/2}} \quad (5\text{-}15)$$

When EQ3/6 calculates the distribution of species in the aqueous phase, it ensures that all aqueous redox pairs are in a state of homogeneous equilibrium at the specified pe, defined in relation to $O_2(g)$ in the above-cited equation. Therefore, when SI(bornite) is calculated, it does so in relation to all equilibrated redox-sensitive species at the specified pe. In the following figures, and those given

in Appendix D, the SIs of redox-sensitive minerals for a given redox-sensitive component can be compared, regardless of the presence of any other redox-sensitive essential components in any given phase.

In the following evaluation, the purpose is to identify coexisting pairs of redox-sensitive minerals that buffer the pe (Eh) of the system at equilibrium, i.e., where the stability fields of each intersect each other at equilibrium with the coexisting groundwater, which can be recognized by the intersection of their respective SIs, where both SIs = 0. In reality, the intersection may occur incrementally above or below SI = 0, because of uncertainties in the thermochemical data used in the analyses, analytical errors (which are accentuated near the detection limits for elements in solution), and other factors, such as temperature, ionic strength, and accountability of all aqueous complexes of the participating species.

The saturation indices of relevant iron and manganese phases as a function of pe were tabulated and the data graphed as shown in Figures 5.3 and 5.4, respectively. To make meaningful comparisons between the saturation indices of different minerals of a given element, each saturation index was normalized to represent the stoichiometry of a mineral containing one mole of the referenced element, e.g., in the iron system, SI(magnetite (Fe_3O_4)) is divided by 3 to yield SI($FeO_{1.333}$).

Table 5.6. *Variation in principal aqueous species of selected redox-sensitive species as a function of pe at circum-neutral pH (pH = 6.9).*

Aqueous	Dominant Aqueous Species at Specified pe								
Species	14	12	10	8	6	4	2	0	-2
Mn	Mn^{+2}	Mn^{+2}	Mn^{+2}	Mn^{+2}	Mn^{+2}	Mn^{+2}	Mn^{+2}	Mn^{+2}	Mn^{+2}
Fe	FeO^{+}	FeO^{+}	FeO^{+}	FeO^{+}	Fe^{+2}	Fe^{+2}	Fe^{+2}	Fe^{+2}	Fe^{+2}
Co	Co^{+2}	Co^{+2}	Co^{+2}	Co^{+2}	Co^{+2}	Co^{+2}	Co^{+2}	Co^{+2}	Co^{+2}
Cu	Cu^{+2}	Cu^{+2}	Cu^{+2}	Cu^{+2}	Cu^{+2}	Cu^{+}	Cu^{+}	Cu^{+}	Cu^{+}
Cd	Cd^{+2}	Cd^{+2}	Cd^{+2}	Cd^{+2}	Cd^{+2}	Cd^{+2}	Cd^{+2}	Cd^{+2}	Cd^{+2}
Pb	$PbCO_3$	$PbCO_3$	$PbCO_3$	$PbCO_3$	$PbCO_3$	$PbCO_3$	PbSe	PbSe	PbSe
Cr	CrO_4^{-2}	CrO_4^{-2}	CrO_4^{-2}	CrO^{+}	CrO^{+}	CrO^{+}	CrO^{+}	CrO^{+}	CrO^{+}
As	$FeAsO_4$(aq)	$FeAsO_4$(aq)	$FeAsO_4$(aq)	$FeAsO_4$(aq)	$FeAsO_4$(aq)	$FeAsO_4$(aq)	$FeAsO_4$(aq)	$AsSe(OH)(SeH)^{-}$	$AsSe(OH)(SeH)^{-}$
Se	SeO_4^{-2}	SeO_4^{-2}	SeO_4^{-2}	$HSeO_3^{-}$	$HSeO_3^{-}$	$HSeO_3^{-}$	ZnSe	FeSe	FeSe
Mo	MoO_4^{-2}	MoO_4^{-2}	MoO_4^{-2}	MoO_4^{-2}	MoO_4^{-2}	MoO_4^{-2}	MoO_4^{-2}	MoO_4^{-2}	MoO_4^{-2}
U	$UO_2(CO_3)_2^{-2}$	$UO_2(CO_3)_2^{-2}$	$UO_2(CO_3)_2^{-2}$	$UO_2(CO_3)_2^{-2}$	$UO_2(CO_3)_2^{-2}$	$UO_2(CO_3)_2^{-2}$	$UO_2(CO_3)_2^{-2}$	$UO_2(CO_3)_2^{-2}$	UO_2
Zn	Zn^{+2}	Zn^{+2}	Zn^{+2}	Zn^{+2}	Zn^{+2}	Zn^{+2}	Zn^{+2}	$Zn(SCN)_4^{-2}$	$Zn(SCN)_4^{-2}$
NO3	NO_3^{-}	N_2	N_2	N_2	N_2	N_2	N_2	N_2	N_2
PO4	H_2PO_4-	H_2PO_4-	H_2PO_4-	H_2PO_4-	H_2PO_4-	H_2PO_4-	H_2PO_4-	H_2PO_4-	H_2PO_4-
SO4	SO_4^{-2}	SO_4^{-2}	SO_4^{-2}	SO_4^{-2}	SO_4^{-2}	SO_4^{-2}	SO_4^{-2}	SO_4^{-2}	SO_4^{-2}
HCO3	HCO_3^{-}	HCO_3^{-}	HCO_3^{-}	HCO_3^{-}	HCO_3^{-}	HCO_3^{-}	HCO_3^{-}	HCO_3^{-}	HCO_3^{-}

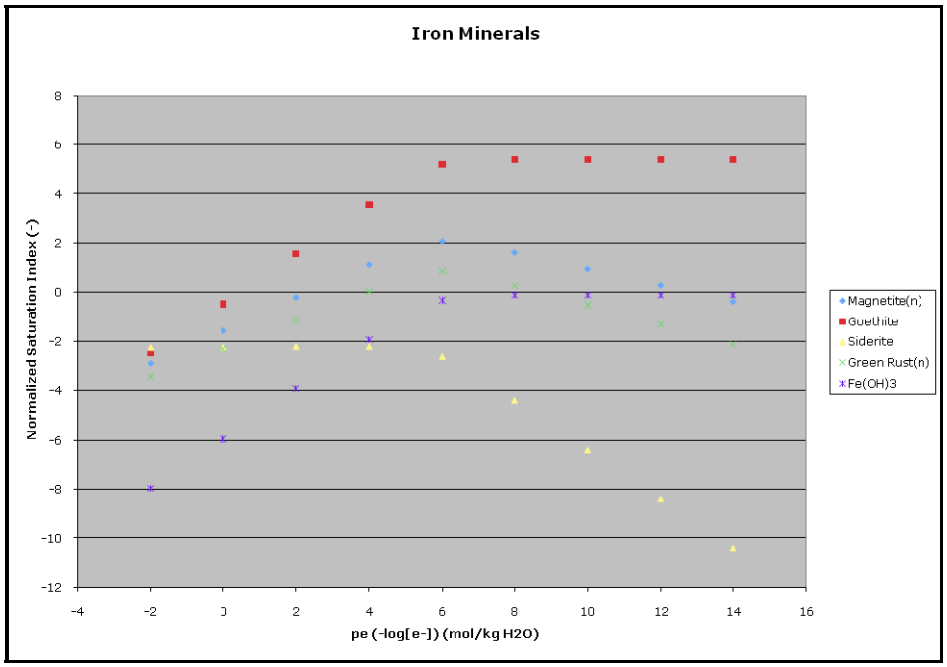

Figure 5.3. *Normalized saturation indices of magnetite, goethite, siderite, green rust (fougerite-CO_3) and $Fe(OH)_3$ (ferrihydrite) plotted as a function of pe.*

Inspection of Figure 5.3 indicates that the phase boundary between fougerite-CO_3 and $Fe(OH)_3$ (ferrihydrite is located where SI(fougerite-CO_2) –SI($Fe(OH)_3$) ≈ 0 at pH =6.82 and pe ≈ +9 (Eh ≈ +0.51 V). This oxidation potential is somewhat higher than that calculated for the boundary between green rust sulfate where pe ≈ +6 at the same pH, as calculated by Majzlan et al. (2004). However, these investigators used the thermodynamic properties for green rust sulfate estimated by Bourrie et al. (1999), which ignored the presence of Mg(II) substitution for Fe(II) in the tri-octahedral sheets. This substitution considerably expands the stability field of naturally occurring fougerite in pe-pH space (Bourrie et al., 2004).

Given the reactive nature of both fougerite-CO_3 and ferrihydrite, and the potentially rapid transformation between one mineral and the other, we assert that the redox potential is most likely to be buffered through the coexistence of these two minerals. Note that detrital magnetite is also observed in the ZERT sediments (Section 4), and both fougerite and ferrihydrite could be reductively transformed to magnetite within the pe range between +2.5 and +13. However, the reaction is likely to be inhibited kinetically. The groundwater would also be supersaturated with respect to goethite at any pe ≥ 1. However, it is well recognized that the presence of SiO_2(aq) inhibits the transformation of green rust and ferrihydrite to more stable oxy-hydroxides (Kwon et al., 2007). Finally, it should be noted that siderite remains unsaturated, i.e., SI(siderite) ≈ -2, even under reducing conditions where all dissolved Fe(T) is transformed to Fe(II), i.e., pe ≤ +4. In this context, it should be mentioned that at greater unsampled depths below the water table, reducing conditions could be such that all Fe(III) in metastable iron oxides, i.e., ferrihydrite and green rust, and presumed to be prevalent near the interface with the vadose zone, could be reduced to Fe(II) and transformed to siderite under ambient P(CO_2).

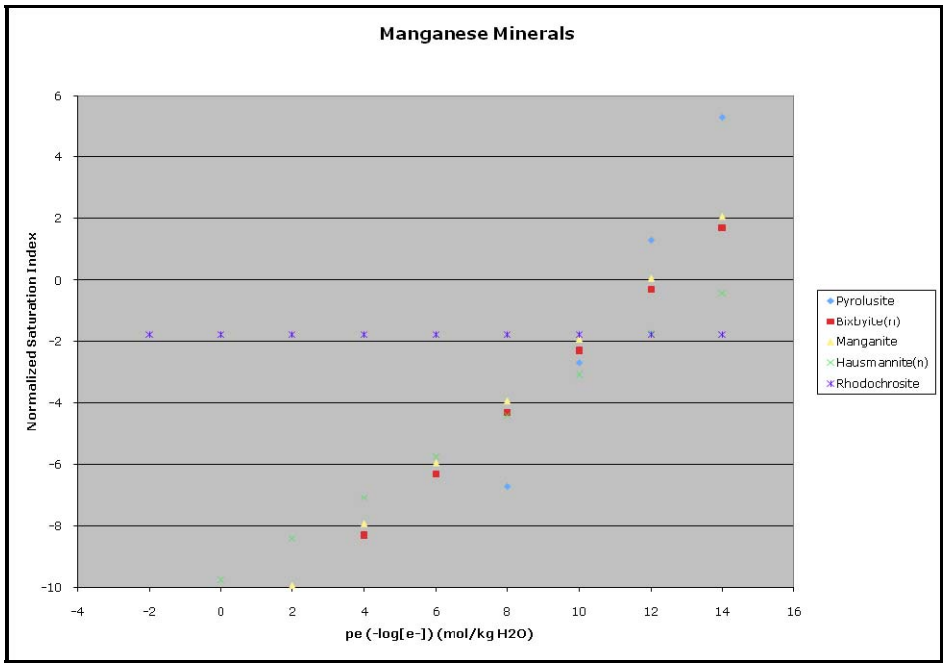

Figure 5.4. *Normalized saturation indices of pyrolusite, bixbyite, manganite, hausmannite and rhodochrosite, plotted as a function of pe.*

Examination of Figure 5.4, which displays the calculated normalized saturation indices of various manganese oxides, shows that pyrolusite (MnO_2) would saturate at pe ≈ +11.5, bixbyite (Mn_2O_3) and manganite (MnOOH) at pe ≈ +12, and hausmannite (Mn_3O_4) at pe ≈ +14.5. Rhodochrosite remains undersaturated, that is, SI(rhodochrosite) ≈ -1.8, throughout the examined range of pe values (-2 < pe < +14). Thus, if any of the minerals pyrolusite, bixbyite, manganite, or hausmannite were present as pure substances, and in equilibrium with the groundwater, the pe would, at a minimum be ≈ +11 (for pyrolusite). However, given that the average crustal abundance of Mn is about 1.7% that of Fe, it is likely that most, if not all Mn is present in solid solution in reactive Fe oxy-hydroxides such as ferrihydrite or goethite, e.g., see Sileo et al. (2001). Thus, assuming an ideal solid solution in ferrihydrite, Mn^{+2} ions would be in equilibrium with a solid solution at pe ≈ 12 – 1.8 = 10.2, which is about 1 pe unit higher that the pe estimated from the pe buffering equilibrium between fougerite-CO_3 and $Fe(OH)_3$ (ferrihydrite). Note that in the presence of significant concentrations of Mn in sediments, Fe(II) can reduce pyrolusite with concomitant precipitation of the manganese spinel, jacobsite ($MnFe_2O_4$), e.g., see Villinski et al. (2000).

In summary, the foregoing analysis of the saturation indices of redox-sensitive minerals indicates that the redox potential of the system is to a large extent controlled by the metastable redox buffering equilibrium between fougerite-CO_3 and ferrihydrite at a pe circa +9 (Eh ≈ +0.51 V). The observed initial concentration of Mn in solution is consistent with saturation with manganese oxide minerals at an oxidation state pe ≤ +11.5, but because the average crustal abundance of Mn is less than that of iron, it is likely that the system pe with respect to Mn is determined by a solid solution of Mn(II) in ferrihydrite, and therefore the pe would be << +11.5. Equilibrium between potential Cr oxide minerals suggests a pe-buffering phase equilibrium between Cr-ferrihydrite and chromite at pe ≈ +8.7, although both the thermodynamic data used in the interpretation and the potential involvement of solid solution substitution in Fe(III) bearing phases such as ferrihydrite discounts

the significance of this observation. Nevertheless, the behavior of the Cr system is consistent with those of Fe and Mn.

The preponderance of the evidence from the foregoing analysis is that the pe of the system is probably buffered at approximately +9 ±1 (see also Appendix D regarding Cr minerals). This value is close to the pe value of +10 of the local partial equilibrium cluster of redox pairs controlled by nitrate observed in shallow Georgia groundwaters by Washington et al. (2004). However, examination of the behavior of Cu and Se minerals as a function of pe (see Appendix D) suggests that organic matter might also be playing a role with respect to the establishment of a lower pe cluster of redox pairs at pe ≈ +1. This compares with an average value of pe ≈ -2 determined by Washington et al. (2004)

Note the distribution of Cr, Fe and Se species in solution at pe = +9, as shown in the following Table 5.7. With respect to Cr, Cr(VI) and Cr(III) species are present in sub-equal concentrations, i.e., 82 mol.% versus 18 mol.%. A similar situation obtains with respect to Se(VI) versus Se(IV) species with respective concentrations of 85.1 and 15 mol.%. With respect to Fe, however, Fe(III) dominates Fe(II) by about 10^3. It is possible that all three species are impacted by NO_3^-/NO_2^- in solution, although unfortunately, the concentration of NO_2^- was not measured in groundwater samples from the ZERT site.

Table 5.7. *Distribution of the predominant Cr, Fe and Se species in solution at pH = 6.82 and pe = +9*

Species	Molality	Percentage
Chromium Species		
CrO_4^{-2}	1.99E-08	43.4
$CaCrO_4(aq)$	1.11E-08	24.2
$HCrO_4^-$	6.55E-09	14.31
CrO^+	6.43E-09	14.04
$CrOH^{+2}$	1.80E-09	3.92
$HCrO_2(aq)$	4.58E-11	1.00E-01
Cr^{+3}	8.91E-12	1.95E-02
Iron Species		
FeO^+	1.28E-07	41.83
$HFeO_2(aq)$	1.05E-07	34.49
$Fe(OH)_2F(aq)$	5.44E-08	17.83
$Fe(OH)_3H_3SiO_4^-$	1.73E-08	5.68
$FeOH^{+2}$	1.49E-10	4.89E-02
Fe^{+2}	1.33E-10	4.36E-02
Selenium Species		
SeO_4^{-2}	2.59E-08	85.1
$HSeO_3^-$	3.16E-09	10.38
SeO_3^{-2}	1.37E-09	4.51

5.2.3 Evolution of Calcite Saturation Indices During Injection

Examination of core material from the ZERT site shows that coatings of secondary calcite are ubiquitous throughout the section, including that section below the water table from which groundwater samples were drawn for analysis. It would therefore not be surprising if a thermodynamic analysis showed that initial groundwater samples taken prior to injection of carbon dioxide were saturated with respect to calcite. However, it must be recognized that the equilibrium state of the shallow subsurface environment at that ZERT site is subject to perturbations due to seasonal and long-term variations in the following parameters:

- Fluctuations in temperature
- Groundwater recharge, leading to fluctuations in the height of the water table.
- Infiltration of rainwater
- Evapotranspiration from the vadose zone
- Capillary transport
- Bio-metabolism

That some or all of these processes are operative is evident from the detection of a caliche horizon within the vadose zone approximately one meter below the surface. An extensive body of literature exists which describes the listed processes in relation to the formation of caliche zones under various climatic conditions, and which could aid in interpreting how these processes might impact groundwater composition and trace element distributions at the ZERT site. However, time limitations permit only a cursory examination of changes in calcite saturation in response to CO_2 injection during the test.

Table 5.8 shows the calculated saturation indices of calcite and calculated $P(CO_2)$ for each groundwater sample based on a thermodynamic analysis using the code EQ3/6 (Wolery, 1992, 1993). The groundwater samples are those taken between the start of the sampling program and the first significant rainfall, i.e., between July 7 and July 17, 2008. The calculations incorporate an adjustment to the analytical value of HCO_3 to account for bicarbonate complexation, and entry of the corrected HCO_3^- as a "free" concentration to force the code to calculate the concentration of dissolved CO_2 in equilibrium with the "free" bicarbonate concentration. Each calculation was conducted at the measured temperature for each groundwater (≈ 10ºC). Also included in Table 5.8 is the calculated charge imbalance, as a percentage of total charge for each groundwater chemical analysis. The charge imbalances are, with the exception of samples 124 and 128, within the acceptable limits of ±5%, and might generally be considered as excellent.

Figure 5.5 is a graphical representation of the same data. It is clear that the increase in ambient $P(CO_2)$ leads to undersaturation of the groundwater with respect to calcite and the rate of dissolution of the calcite is insufficient to maintain equilibrium. The trend is irregular and shows considerable scatter, which would be expected of a system where samples are taken from different wells at different depths in a soil system that is vertically heterogeneous, and probably also laterally heterogeneous. Also plotted on Figure 5.5 are three trend lines. Trend Line A assumes the approximate path taken with respect to calcite resaturation as $P(CO_2)$ increases. This path would vary depending on the rate of CO_2 saturation of the groundwater, the kinetics of calcite dissolution, calcite surface area and abundance, and groundwater flow rates. Path A is constrained by the other two trend lines. Trend Line B is the path taken under static conditions where resaturation of calcite occurs after instantaneous saturation of the groundwater with CO_2 at a pressure of 1 bar, the

approximate limit of saturation expected at the ZERT site. Trendline C assumes that no dissolution of calcite takes place upon uptake of CO_2. It is evident that about half of the water samples taken between July 7 and July 17, 2008 reflect this state of affairs (close to trendline C), and that only after log $P(CO_2)$ exceeded ≈ -0.7, equivalent to 0.2 bar, did significant dissolution of calcite occur.

From the start of the test until the first significant rainfall, the water table fell progressively, which suggests that the water table was still responding to some rainfall event preceding the start of the test, due either to drainage, or to evapotranspiration. Dilution by rainfall could explain the initial degree of undersaturation of calcite, and this observation is indirectly corroborated by the observed undersaturation with respect to opal-CT and amorphous hydroxy-aluminosilicates (HAS). For this reason, it is less likely that the initial undersaturation might be due to transient elevation of $P(CO_2)$ due to aggressive mineralization of carbonaceous material by bacteria.

Table 5.8. *Calculated calcite saturation index and CO_2 partial pressure for groundwaters taken at the ZERT site between July 7 and July 17, 2008*

ZERT Sample No.	Charge Imbalance. %	SI(Calcite) (-)	Log $P(CO_2)$ (bars)
102	-1.20	-0.377	-1.3113
103	-4.10	-0.342	-1.2739
104	-0.30	-0.156	-1.3567
105	-1.73	+0.691	-0.951
106	0.15	-0.301	-1.4203
107	0.65	-0.524	-1.2369
109	0.96	-0.090	-1.4708
112	0.74	-0.566	-0.9664
116	-2.00	-0.369	-0.3542
117	2.94	-1.237	-0.0961
118	0.78	-0.415	-0.7166
119	0.08	-0.178	-1.5106
124	-7.69	-0.492	-0.0881
126	0.63	-0.781	-0.7594
127	0.09	-0.856	-0.1881
128	8.11	-0.715	-0.1458
129	-2.95	-0.588	-0.1579
130	-1.20	-0.759	-0.7421
131	-1.30	-0.827	-0.1648
132	-2.39	-0.692	-0.09

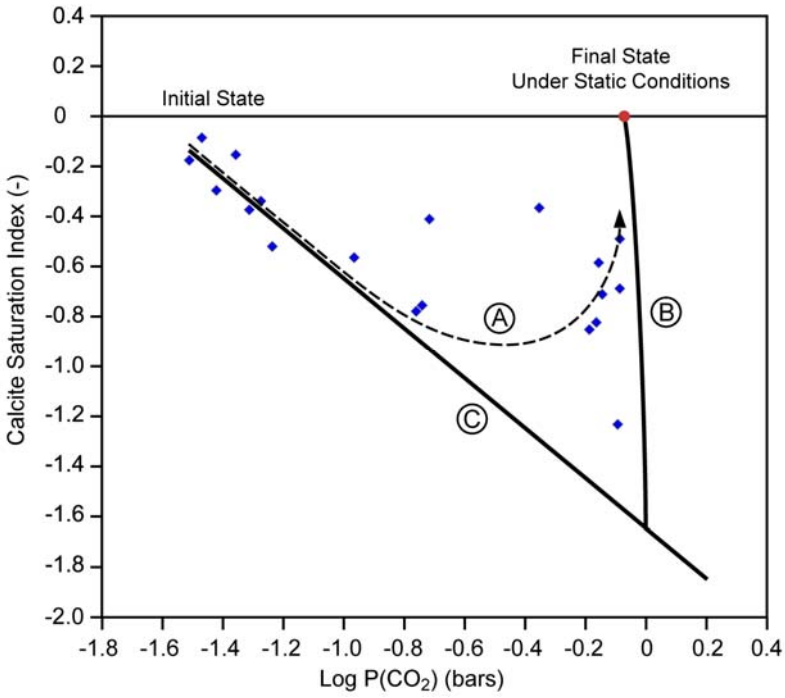

Figure 5.5. *Saturation index of calcite as a function of log $P(CO_2)$ calculated for groundwater samples taken between July 7 and July 17, 2008 at the ZERT site. For an explanation of the trend lines, please refer to the text.*

5.2.4 Findings from Geochemical Evaluations

This section summarizes the principal findings of the foregoing geochemical evaluations. These findings have been useful in setting up the geochemical model described in Section 5.3 below.

- Principal Component Analysis of the initial perturbation (first 10 days of the test) in groundwater quality due to CO_2 uptake shows strong positive linear correlations between the transformed logarithmic concentrations of many of the measured species. The first principal component, PC1, correlates strongly with monovalent, divalent and trivalent cations, suggesting that ion exchange on smectite might be the mechanism responsible for their release. The positive correlation between various anionic species: HCO_3, SO_4, Mo (as MO_4) and Se (as SeO_3 or SeO_4) and PC1 also suggest a common mechanism involving either ion exchange or adsorption. However, NO_3 and PO_4 are negatively correlated. The second principal component, PC2, correlates strongly with F, and relatively weakly with As, Se and Mo, and inversely, but weakly with H and K, suggesting some anionic exchange or adsorption process. The third principal component, PC3, correlates inversely with Mn, Co and Cl, and directly with As, NO_3 and PO_4, suggesting precipitation control by a transition metal phosphate. PC4 correlates with Cl and SO_4, which may be related to earlier infiltration of rain water from the overlying vadose zone. Not all correlation trendlines between the various species are readily explained, highlighting the need for more in-depth study of the geochemistry of shallow groundwater systems (Section 5.2.1).
- Thermodynamic evaluation of the groundwater chemistry before CO_2 injection reveals a species distribution that reflects rapid weathering and the formation of metastable hydroxy-

aluminum silicates. The initial groundwater is slightly undersaturated with respect to calcite, opal-CT and barite, suggesting dilution of the groundwater by rainwater prior to the test. Supersaturation with respect to smectites, illite and kaolinite and gibbsite is indicative of saturation by persistent metastable hydroxy-aluminum silicates (Section 5.2.2).

- Examination of the degree of supersaturation of redox sensitive minerals as a function of pe (or Eh) suggests that the redox potential is most likely buffered by the coexistence of fougerite-CO_3 and $Fe(OH)_3$ (ferrihydrite) at a pe ≈ +9. However, there are also indications that the concentrations of some trace elements, e.g., Cd, Cu, Pb, may be controlled by precipitation of reduced species such as CdSe, Cu_2O and PbSe. This suggests that decaying organic matter might be exercising reductive control over these, and possibly other species, which implies that the system redox state is not in equilibrium, and may also be spatially inhomogeneous. The distribution of species, therefore, may be kinetically controlled (Section 5.2.2).
- Examination of the perturbation in calcite saturation following injection of CO_2 shows that calcite immediately became significantly undersaturated, but recovery of the saturation states was slow and incomplete during the first ten days of the test (Section 5.2.3).

5.3 Geochemical Modeling

Geochemical simulations were run to test some of the observations discussed earlier, namely that ion exchange and sorption processes, together with dissolution of carbonates, could explain the water chemistry trends observed during the test (Zheng et al., 2009a). Additional modeling work incorporating transport processes was not warranted because of the relatively limited set of field data, as well as uncertainties regarding groundwater flow and CO_2 transport (e.g., Section 5.1), subsurface heterogeneity, and rainfall effects. It should be noted that geochemical changes in groundwater after the release of CO_2 were fairly rapid and even, occurring almost simultaneously in wells 1B, 2B and 5B (Section 3). Furthermore, PCA analyses (Section 5.2) reveal similar groundwater chemistry responses to CO_2 injection at the different monitored locations. This suggests that "batch" simulations, focused solely on reactive processes induced by increasing levels of CO_2, are a good modeling approach in this case, with little more to gain from more sophisticated simulations including transport. The simulations were performed using, TOUGHREACT (Xu et al., 2006), which was enhanced through incorporation of surface complexation and ion exchange models to compute the distribution of adsorbed chemical species on mineral surfaces (Zheng et al., 2009b).

Rainfall was shown to significantly affect groundwater chemistry during the test (Section 3). Because of the limited amount of rainfall-related data (including composition, recharge rates, and oxidation/mixing effects in the subsurface), and because PCA analyses (Section 5.2.1) focused on the groundwater chemistry data before the first rainfall, the geochemical simulations discussed below were based solely on groundwater data collected before the first rainfall.

5.3.1 Model setup

A "batch" (single-gridblock) geochemical model was developed, with initial conditions representative of field conditions prior to CO_2 injection (Table 5.9). CO_2 was then (numerically)

injected into the modeled system, and model results were examined as a function of pH. As discussed previously, the CO_2 volume fractions measured in the head space of groundwater monitoring wells increased rapidly (within a day to a few days) to levels up to 0.9 (90% by volume), corresponding to $P(CO_2)$ values near 1 bar at the water table soon after injection. CO_2 was injected into the model gridblock until the computed pH value fell from an initial value ~7.1 to a value near 5.8, consistent with the field measurements. At this point, the calculated maximum $P(CO_2)$ was around 1.5 bar. Instantaneous equilibration of gaseous CO_2 with the aqueous phase was assumed. Other elements of the model are described below. Simulations were carried out assuming an initial temperature of 10°C and an initial pressure close to atmospheric values.

Initial conditions

Seven groundwater samples were taken before the release of CO_2. The initial chemical composition for the model (Table 5.9) was taken from one of these samples (i.e., 08ZERT-107), with initial pH adjusted slightly from 6.7 to 7.1 so that our calculation covers the pH range of all samples considered in this study. An initial aqueous speciation was conducted with EQ3 (Wolery, 1993) to verify charge balance and evaluate the water saturation with respect to several minerals. The initial partial pressure of CO_2 in the groundwater was calculated to be 2.5×10^{-2} bars. Furthermore, calcite was close to saturation, i.e., SI(calcite) ≈ –0.1 (–0.3 at pH 6.7).

As pointed out in Section 5.2, redox is not likely to have reached equilibrium in this shallow, low-temperature system. This complicates the use of geochemical models such as the one applied here, because these models rely on the assumption of redox equilibrium to calculate the distribution of redox-sensitive species. Here, the initial redox state of the groundwater is calculated from the Fe(II)/Fe(III) equilibrium using the measured (total) Fe concentration in water and assuming equilibrium with goethite, yielding a pe ~ 1.7. Assuming equilibrium with ferrihydrite and fougerite (green rust) would result in a significantly higher value (pe ~9) (Section 5.2.2). This range of pe values suggests suboxic (but not strongly reducing) conditions prevail at the site. Note that measured Eh values (150–200 mV, Section 3) correspond to pe ~ 2.5–3.5. However, as discussed in Section 5.2.2, measured potentials represent mixed potentials that are not representative of a specific redox couple and that may be biased by the redox sensor. Given these uncertainties, and the fact that redox equilibrium is assumed in the simulations, model results regarding redox species should be viewed as qualitative rather than quantitative. Obviously, the choice of pe affects model results for redox-sensitive species. However, in this modeling case, the amount of solid Fe for sorption is unknown and adjusted to match observed groundwater compositions. Therefore, assuming a higher pe would likely be compensated by this calibration such that, qualitatively, model results would not be expected to change significantly if a different pe was used.

Table 5.9. *Primary species and their initial concentration*

Species	Concentration (mol/L)	Species	Concentration (mol/L)
pH	7.1	Ba^{+2}	7.9E-07
Ca^{+2}	1.9E-03	Cd^{+2}	2.0E-09
Mg^{+2}	9.8E-04	Co^{+2}	4.2E-09
Na^{+}	3.3E-04	Cu^{+2}	2.4E-08
K^{+}	1.4E-04	$H_2AsO_4^{-}$	1.3E-08
Fe^{+2}	1.8E-09	Mn^{+2}	1.8E-08
AlO_2^{-}	1.2E-07	Sr^{+2}	3.0E-06
SiO_2(aq)	5.3E-04	Zn^{+2}	4.6E-08
Cl^{-}	1.3E-04	$HSeO_3^{-}$	4.9E-08
HCO_3^{-}	6.3E-03	MO_4^{-2}	4.6E-09
SO_4^{-2}	7.7E-05	UO_2^{+2}	1.7E-08
NO_3^{-}	9.6E-06	$Cr(OH)_2^{+}$	2.2E-07
O_2(aq)[1]	1.2E-51	HPO_4^{-2}	1.8E-06
Pb^{+2}	2.4E-10	Li^{+}	7.7E-07

[1]Corresponds to pe ~ 1.7, Eh ~ 100 mV (see text)

Mineralogy

Section 4.2 describes the mineralogical analyses of cored sections to a depth of approximately 3 m. Sediments in the saturated zone are composed predominantly of a matrix of cobble-sized rounded fragments, consisting primarily of andesitic volcanic rocks with predominant plagioclase, quartz-biotite-amphibole gneiss, and red granite/gneiss. The mafic volcanic rock fragments are very high in magnetic iron. Minor limestone and occasional dolomite fragments are also observed in the matrix. Unspecified Fe oxides appear in a <0.25 mm fraction as "powdery orange blebs." Secondary carbonate coatings are found throughout the core, and a caliche zone is present in the overlying unsaturated zone. Small quantities of clay (~1 wt%), believed to consist of smectite and minor kaolinite are also found in the saturated zone. The list of minerals considered in the geochemical model (Table 5.10) was based on these observations, as well as on the discussions in Section 5.2. Arbitrary volume fractions are assigned to each mineral, which are roughly consistent with the mineralogy analyses. It should be noted that in the time frame of the simulation described in this report, most of the listed rock-forming minerals are essentially inert, i.e., they are mostly unreactive during the short injection period, as discussed later.

Table 5.10. *Minerals considered in the model.*

Primary Mineral	Volume fraction	Primary Mineral	Volume fraction
Quartz	0.45	Ferrihydrite	0.01
K-feldspar	0.1	Magnetite	0.02
Oligoclase	0.34	Goethite	0.001
Smectite	0.01	Siderite	0.001
Dolomite	0.02	Calcite	0.05

Chemical reactions and equilibrium/kinetic constraints

Chemical reactions considered in the model include aqueous complexation, cation exchange, adsorption/desorption, and mineral dissolution/precipitation. Of these, cation exchange and

adsorption/desorption reactions are believed to predominate (see Section 5.2.1). Table 5.11 lists aqueous complexes included in the simulation and their dissociation constants which are from database data0.ymp.R4 (Wolery and Jareck, 2003; Wolery and Jove-Colon, 2007). Table 5.12 lists the cation exchange reactions and their selectivity coefficients. The Gaines-Thomas convention is used here. The selectivity coefficient for exchangeable H^+ is taken from Charlet and Tournassat (2005), and those for the remainder of the exchangeable cations are taken from Appelo and Postma (1994). The cation exchange capacity (CEC) is the key parameter for the calculation of cation exchange. Because the measured CEC for the sediments at ZERT site is not currently available, we used a CEC value of around 12 meq/100g measured for Hanford sediments (Steefel et al., 2003), which has similar composition to the sediments at the ZERT site. A nonelectrostatic surface complexation model calculates adsorption/desorption, which involves most anions and H^+. Table 5.13 lists the surface complexation reactions. Surface complexation constants are taken from Dzombak and Morel (1990). Hydrous ferric iron oxide (HFO) is assumed to be the only adsorbent. The site density for the strong site is assumed to be 1.76×10^{-6} mol/m^2, and that for weak sites is assumed to be 3.22×10^{-6} mol/m^2 (Muller and Sigg, 1991). The specific surface area is assumed to be 14.7 m^2/g (Muller and Sigg, 1991). The amount of HFO for sorption was (loosely) calibrated to metal concentrations in groundwater using these data.

Table 5.11. *Aqueous complexes and their dissociation constants*

Species	Logk (25°C)	Species	Logk (25°C)	Species	Logk (25°C)	Species	Logk (25°C)
OH^-	13.991	$Al(OH)_2^+$	-12.78	$Cu(CO_3)_2^{-2}$	10.476	$SrOH^+$	13.292
$CaHCO_3^+$	-1.043	$AlOH^{+2}$	-17.868	$NaHCO_3$(aq)	-0.17	$UO_2(CO_3)_2^{-2}$	3.747
$FeHCO_3^+$	-2.044	$Al_{13}O_4(OH)_{24}^{+7}$	-198.749	$NaSO_4^-$	-0.811	$UO_2(CO_3)_3^{-4}$	9.43
$FeCO_3$(aq)	4.879	$CdCl^+$	-1.966	NaCl(aq)	0.782	$UO_2(CO_3)$ (aq)	0.663
CO_2(aq)	-6.342	$HCOO_2^-$	21.243	$PbCl^+$	-1.456	$UO_2(OH)_2$(aq)	10.315
CO_3^{-2}	10.325	$HAsO_4^{-2}$	6.754	$PbCl_2$(aq)	-2.016	$Cr(OH)_3$(aq)	8.3
$MgHCO_3^+$	-1.033	$MnCO_3$(aq)	5.809	$SrSO_4$(aq)	-2.271	$Cr(OH)^{+2}$	-5.7
$MgSO_4$(aq)	-2.382	$MnHCO_3^+$	-0.882	$SrCO_3$(aq)	7.47	$CaHPO_4$(aq)	-2.69
$CaSO_4$(aq)	-2.1	$BaCO_3$(aq)	7.691	$SrCl^+$	0.253	$MgHPO_4$(aq)	-2.91
$HAlO_2$(aq)	-6.448	$CuOH^+$	7.287	$SrNO_3^+$	-0.796		

Table 5.12. *Cation exchange reactions and selectivity coefficients.*

Cation exchange reaction	$K_{Na/M}$
$Na^+ + X\text{-}H = X\text{-}Na + H^+$	1
$Na^+ + X\text{-}K = X\text{-}Na + K^+$	0.2
$Na^+ + 0.5X\text{-}Ca = X\text{-}Na + 0.5Ca^{+2}$	0.4
$Na^+ + 0.5X\text{-}Mg = X\text{-}Na + 0.5Mg^{+2}$	0.45
$Na^+ + 0.5X\text{-}Pb = X\text{-}Na + 0.5Pb^{+2}$	0.4
$Na^+ + 0.5X\text{-}Ba = X\text{-}Na + 0.5Ba^{+2}$	0.35
$Na^+ + 0.5X\text{-}Cd = X\text{-}Na + 0.5Cd^{+2}$	0.4
$Na^+ + 0.5X\text{-}Co = X\text{-}Na + 0.5Co^{+2}$	0.6
$Na^+ + 0.5X\text{-}Cu = X\text{-}Na + 0.5Cu^{+2}$	0.5
$Na^+ + 0.5X\text{-}Mn = X\text{-}Na + 0.5Mn^{+2}$	0.55
$Na^+ + 0.5X\text{-}Sr = X\text{-}Na + 0.5Sr^{+2}$	0.35
$Na^+ + 0.5X\text{-}Zn = X\text{-}Na + 0.5Zn^{+2}$	0.4
$Na^+ + 0.5X\text{-}Fe = X\text{-}Na + 0.5Fe^{+2}$	0.6

Table 5.13. *Surface complexation reactions and surface complexation constants (logK) on HFO*

Surface complexation	logK
$HFO\_sOH_2^+ = HFO\_sOH + H^+$	-7.29
$HFO\_wOH_2^+ = HFO\_wOH + H^+$	-7.29
$HFO\_sO^- + H^+ = HFO\_sOH$	8.93
$HFO\_wO^- + H^+ = HFO\_wOH$	8.93
$HFO\_sOHSO_4^{-2} = HFO\_sOH + SO_4^{-2}$	-0.79
$HFO\_wOHSO_4^{-2} = HFO\_wOH + SO_4^{-2}$	-0.79
$HFO\_sSO_4^- + H_2O = HFO\_sOH + SO_4^{-2} + H^+$	-7.78
$HFO\_wSO_4^- + H_2O = HFO\_sOH + SO_4^{-2} + H^+$	-7.78
$HFO\_sSeO_3^- + H_2O = HFO\_sOH + HSeO_3^-$	-4.29
$HFO\_wSeO_3^- + H_2O = HFO\_wOH + HSeO_3^-$	-4.29
$HFO\_sMoO_4^- + H_2O = HFO\_sOH + MoO_4^- + H^+$	-9.5
$HFO\_wMoO_4^- + H_2O = HFO\_wOH + MoO_4^- + H^+$	-9.5
$HFO\_sOHMoO_4^{-2} = HFO\_sOH + MoO_4^{-2}$	-2.4
$HFO\_wOHMoO_4^{-2} = HFO\_wOH + MoO_4^{-2}$	-2.4
$HFO\_sH_2AsO_4 + H_2O = HFO\_sOH + H_2AsO_4^- + H^+$	-10.17
$HFO\_wH_2AsO_4 + H_2O = HFO\_wOH + H_2AsO_4^- + H^+$	-10.17
$HFO\_sHAsO_4^- + H_2O = HFO\_sOH + H_2AsO_4^-$	0.35
$HFO\_wHAsO_4^- + H_2O = HFO\_wOH + H_2AsO_4^-$	0.35
$HFO\_sH_2PO_4 + H_2O = HFO\_sOH + HPO_4^{-2} + 2H^+$	-18.9
$HFO\_w\ H_2PO_4 + H_2O = HFO\_wOH + HPO_4^{-2} + 2H^+$	-18.9
$HFO\_sPO_4^{-2} + H_2O = HFO\_sOH + HPO_4^{-2}$	-5.4
$HFO\_wPO_4^{-2} + H_2O = HFO\_wOH + HPO_4^{-2}$	-5.4
$HFO\_wCO_2^- + H_2O = HFO\_sOH + HCO_3^-$	-2.45
$HFO\_wCO_2H + H_2O = HFO\_sOH + HCO_3^- + H^+$	-2.45

All minerals are set to react under kinetic constraints. Currently, TOUGHREACT (Xu et al., 2006) uses a general form of kinetic rate law based on the transition state theory (TST) (Lasaga et al., 1994; Steefel and Lasaga, 1994):

$$r = kA\left[1-\left(Q/K\right)^{\theta}\right]^{\eta} \tag{5-16}$$

where r is the kinetic rate (positive values indicate dissolution, negative values precipitation), k is the rate constant (moles per unit mineral surface area and unit time), which is temperature dependent, A is the specific reactive surface area per kg H_2O, K is the equilibrium constant for the mineral–water reaction, and Q is the reaction quotient. Here, the parameters θ and η are assumed equal to unity, and surface areas are estimated based on Xu et al. (2006). For further details concerning the kinetics of mineral dissolution/precipitation, the reader is referred to Xu et al. (2006).

Tables 5.14 and 5.15 list the equilibrium constants (as log(K)) and rate constants (k), respectively, for minerals included in the simulations. Except for siderite, equilibrium constants are from database data0.dat.ymp.R4 (Wolery and Jareck, 2003; Wolery and Jove-Colon, 2007). The equilibrium constant for siderite was calculated from more recent data from Preis and Gamsjager (2002), and differs slightly from that adopted in data0.ymp.R4. The value of Q/K in Equation 5-16 dictates whether dissolution or precipitation occurs. In the present case, all minerals dissolve. However, except for calcite and siderite, the calculated dissolution rates are very small (relative to the length of the test) and do not affect model results.

The dissolution rate of calcite is critical, because the increase of Ca^{+2} resulting from calcite dissolution affects cation exchange, which may be responsible for the increases in major cations and most trace metals except for Fe and possibly Mn and Co (Section 5.3.2). Depending on the level of undersaturation, according to Kaufmann and Dreybrodt (2007), the dissolution of calcite can be described by a fast and a slow rate law. The fast and slow rate laws are discriminated by the ratio of calcium concentration in the solution to the calcium concentration in equilibrium with calcite (C/Ceq) at a given CO_2 partial pressure. Kaufmann and Dreybrodt (2007) reported that when the ratio (C/Ceq) is <0.3, the fast rate law applies, whereas when C/Ceq > 0.3, the slow rate law applies. In the current simulations, C/Ceq is about 0.4–0.5, and thus the slow rate law of Kaufmann and Dreybrodt (2007) is adopted, with the rate constant k (Equation 5-16) equal to 1.6×10^{-6} mol/m^2/s. Svensson and Dreybrodt (1992) investigated the dissolution kinetics of calcite in CO_2-water systems approaching calcite equilibrium and gave a rate constant k of 1.6×10^{-6} – 2.2×10^{-6} mol/m^2/s, although they indicated that C/Ceq should be around 0.6–0.8. Gledhill and Morse (2006) reported that the dissolution rate depends on brine composition, P(CO_2) (0.1–1 bar), and temperature and the rate constant (k) can be estimated from a multiple regression model. Applying their regression model to our simulation conditions, the rate constant is from 1.6×10^{-6} to 2.2×10^{-5} mol/m^2/s. Jordan and Rammensee (1998) gave a dissolution rate of 1.6×10^{-6} mol/m^2/s on the calcite surface obtained by scanning force microscopy, which corresponds well to the rates obtained from batch experiments. Pokrovsky et al. (2005) measured the dissolution rate of calcite at high pressure, which is more relevant to deep CO_2 geological storage than CO_2 releases at the ZERT site. Therefore, these various published dissolution rates for calcite at lower levels of undersaturation are all quite consistent with the value selected for this study.

The baseline model considers only cation exchange for iron. However, sensitivity analyses were conducted to consider the dissolution of green rust (fougerite) and siderite. Note that siderite is initially undersaturated (SI ≈ -1.5) and thus unlikely to be present, except possibly as a detrital phase. For siderite, the kinetic rate reported by Duckworth and Martin (2004) is adopted. These investigators studied the dissolution of siderite under both oxic and anoxic conditions at 298 K, and fitted their measured data to a mechanistic kinetic equation similar to that employed in TOUGHREACT. The rate constant is given for both neutral and acid dissolution mechanisms:

$$k = k_n[\mathrm{H_2O}] + k_H[\mathrm{H^+}] \tag{5-17}$$

with $k_n = 10^{-8.65}$ mol/m^2/s and $k_H = 10^{-4.6}$ mol/m^2/s, respectively. The dissolution rate is dominated by the neutral mechanism when pH > 5.5, whereas the acid mechanism becomes important when pH < 5.5. Testemale et al. (2009) confirmed that the dissolution rate constant of siderite at acid condition (pH < 4) can be expressed as:

$$k = k_H[\mathrm{H^+}] \tag{5-18}$$

with $k_H = 10^{-9.3}$ mol/cm^2/s ($k_H = 10^{-5.3}$ mol/m^2/s) which is close to the k_H given by Duckworth and Martin (2004). Testemale et al. (2009) compared their findings with other data (Braun, 1991; Golubev et al., in press) and concluded that published kinetic rates for siderite dissolution are generally in good agreement. Duckworth and Martin (2004) also mentioned that the dissolution of siderite is retarded under oxic conditions, due to armoring by Fe (hydr)oxides. At the ZERT site, the proximity of the water table to ground surface and presence of secondary ferric oxy-hydroxides suggest oxic to suboxic conditions may prevail, at least during rainfall events. Therefore, the siderite dissolution rate adopted for the model could be underestimated.

The initial water is supersaturated with respect to green rust (SI ≈ 0.3, normalized to 1 Fe), although this mineral readily dissolves upon pH decrease. Its dissolution rate is taken from Williams and Scherer (2001) with $k_n = 10^{-8.82}$ mol/m^2/s and $k_H = 10^{-2.6}$ mol/m^2/s (Equation 5-16).

Table 5.14. *Equilibrium constants for minerals*[1]

Primary Mineral	log(*K*)	Primary Mineral	log(*K*)
Quartz	-3.75	Ferrihydrite	-63.24
K-feldspar	-22.91	Magnetite	-6.505
Oligoclase	-97.78	Goethite	-8.12
Smectite	-39.51	Siderite	-0.251
Dolomite	2.524	Calcite	1.85
Fougerite	24.24		

[1] *For dissolution in terms of species shown in Table 5.9*

Table 5.15. *Initial volume fraction and kinetic parameters for minerals considered in the model*[1]

Mineral	Volume fraction	A (cm^2/g)	Parameters for Kinetic Rate Law				
			Neutral Mechanism	Acid Mechanism		Base Mechanism	
			k_{25} ($mol/m^2/s$)	k_{25} ($mol/m^2/s$)	$n(H^+)$	k_{25} ($mol/m^2/s$)	$n(H^+)$
Quartz	0.45	9.8	1.023×10^{-14}	–	–	–	–
K-feldspar	0.1	9.8	3.89×10^{-13}	8.71×10^{-11}	0.5	6.31×10^{-12}	-0.823
Oligoclase	0.338	9.8	1.44×10^{-12}	2.13×10^{-10}	0.457	–	–
Smectite	0.01	151.6	1.66×10^{-13}	1.05×10^{-11}	0.34	3.02×10^{-17}	-0.4
Dolomite	0.02	9.8	2.95×10^{-8}	6.46×10^{-4}	0.5	–	–
Ferrihydrite	0.01	12.9		2.34×10^{-7}	1	–	–
Magnetite	0.02	9.8	4.57×10^{-10}	4.17×10^{-7}	1	–	–
Goethite	0.001	12.9	2.52×10^{-12}	–	–	–	–
Siderite	0.001	22.3	2.24×10^{-9}	2.5×10^{-5}	0.75	–	–
Calcite	0.05	3.05	1.6×10^{-6}	–	–	–	–

1 Kinetic data from Xu et al. (2006), except for calcite (Kaufmann and Dreybrodt 2007) and siderite (Duckworth and Martin, 2004), see text.

5.3.2 Results and Discussion

Earlier generic studies of CO_2 leakage into potable groundwater aquifers (Birkholzer et al., 2008; Wang and Jaffe, 2004; Zheng et al., 2009b) indicated that the dissolution of carbonate minerals (mainly calcite) can significantly buffer the pH decrease accompanying the dissolution of CO_2 in water (from the dissociation of carbonic acid). Clay ion exchangers, when present in significant amounts in an aquifer host rock or sediment, can also strongly buffer pH through exchange of H^+ with the groundwater (Bradbury and Baeyens, 1997; Samper et al., 2008; Zheng and Samper, 2009; Zheng et al., 2009c). In the present model, the dissolution of calcite, dolomite and siderite, and H^+ buffering through cation exchange and surface complexation could all contribute to buffering pH. Figure 5.6 shows the calculated pH by different combinations of these chemical equilibria. A simulation without carbonate minerals leads to a lower pH than the base case where the presence of carbonates is assumed, but is only marginally higher than the simulation without any buffering. This suggests that at the ZERT site, dissolution of carbonate minerals is the principal pH buffering process, whereas the H^+ exchange by clays does not affect pH significantly, because the shallow saturated zone at the ZERT site soil does not contain large amounts of clay minerals, and the pH decrease is only moderate.

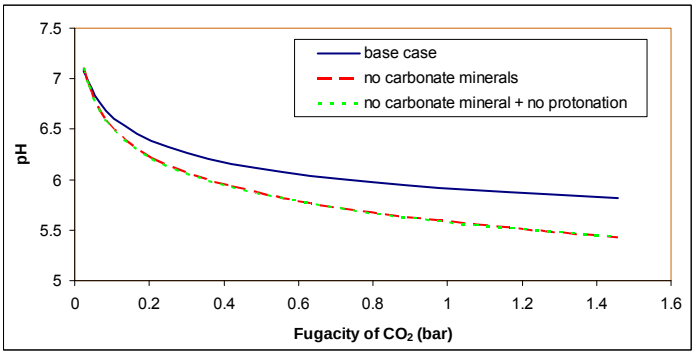

Figure 5.6. *Calculated pH with different combination of chemical reactions*

The groundwater at the ZERT site responds promptly to the release of CO_2. The pH falls within 1 or 2 days from the start of injection, and a significant increase in major cations and trace metals is observed before the first rainfall occurs, about 10 days later. In such a short-duration test, only the dissolution kinetic rates for rapidly dissolving minerals such as calcite are important. As noted earlier, the dissolution rate of calcite is critical, because the resulting increase of Ca^{+2} induces cation exchange, which may be responsible for the increases in major cations and most trace metals except for Fe and possibly Mn and Co. The value adopted in this study falls within the lower range of published values (Section 5.3.1) and yields results consistent with measured changes in calcium concentration observed in the field (Figure 5.7). If a higher calcite dissolution rate is used, such as that given by Gledhill and Morse (2006), i.e., 2.2×10^{-5} mol/m^2/s, the computed calcium concentration overestimates the measured data (Figure 5.7).

As pH decreases, calcite dissolves and releases Ca^{+2} into the aqueous phase. Aqueous Ca^{+2} in turn exchanges with the exchangeable cations on the cation exchanger, tentatively assumed to be smectite. As a result, the concentrations of all the major cations increase in solution. Figures 5.8–5.10 show the calculated sodium, potassium, and magnesium concentration versus pH. The close agreement between calculated and measured concentrations supports the hypothesis that cation exchange may indeed dominate the evolution of major cations in response to the CO_2 injection at the ZERT site.

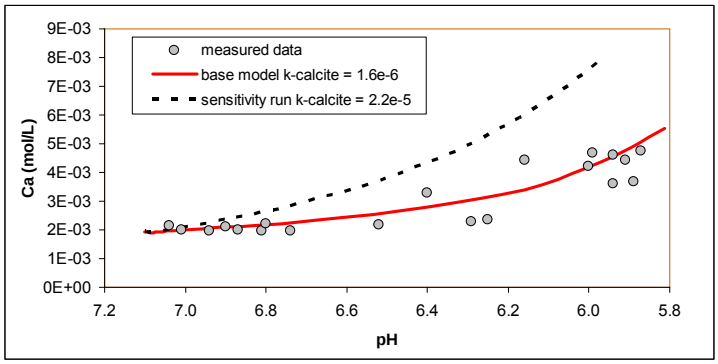

Figure 5.7. *Calculated calcium concentration vs pH with different calcite dissolution rate.*

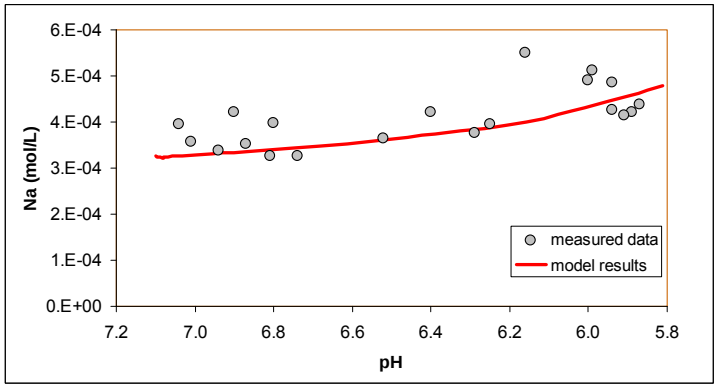

Figure 5.8. *Calculated sodium concentration vs pH.*

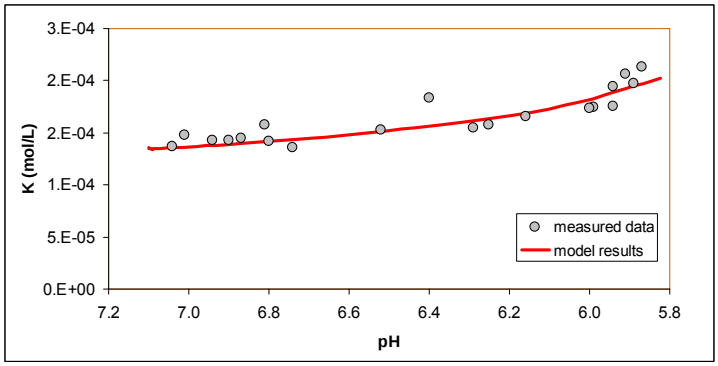

Figure 5.9. *Calculated potassium concentration vs pH.*

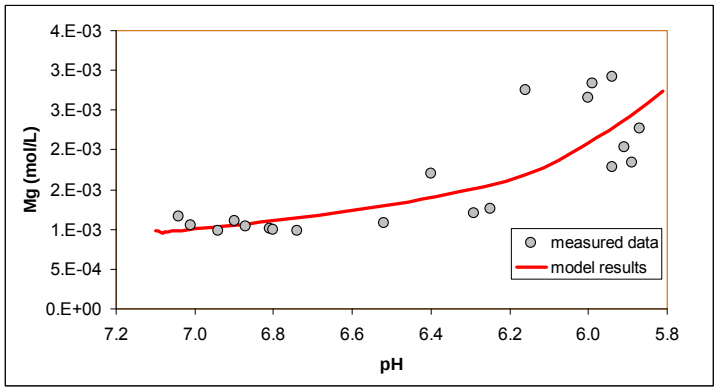

Figure 5.10. *Calculated magnesium concentration vs pH.*

Figures 5.11-5.14 show the calculated trace metal concentrations for lead, cadmium, copper, and zinc. With the exception of Zn, which PCA shows to behave anomalously, reasonable matches between calculated and measured concentrations again suggest that the calcium-driven cation exchange could explain the observed trace metal response to CO_2 injection.

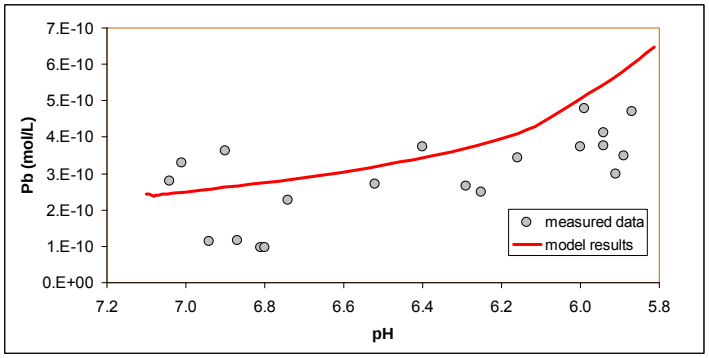

Figure 5.11. *Calculated lead concentration vs pH*

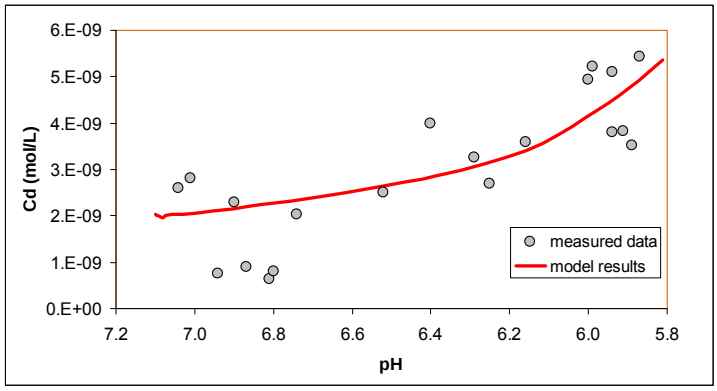

Figure 5.12. *Calculated cadmium concentration vs pH*

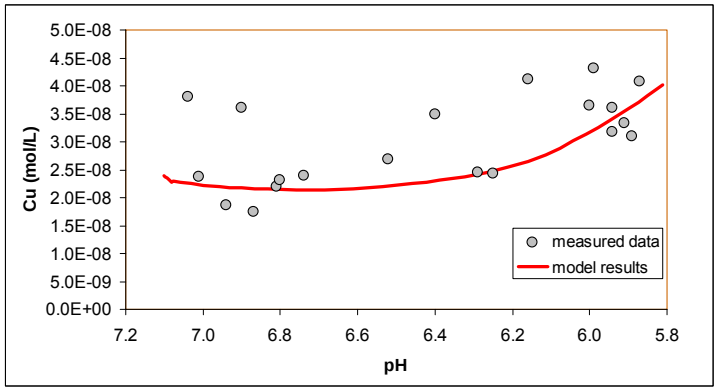

Figure 5.13. *Calculated copper concentration vs pH*

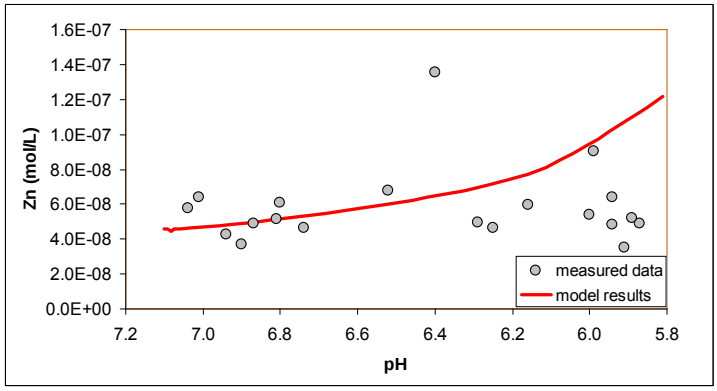

Figure 5.14. *Calculated zinc concentration vs pH*

The baseline model, which considers only cation exchange for iron, leads to a significant underestimation of measured iron concentrations (see Figure 5.15). This finding is consistent with the PCA, which indicates that its behavior is not identified with the component associated with ion exchange. If siderite dissolution is assumed to contribute to the increase in aqueous iron concentration, a better fit is obtained, although the predicted iron concentrations are still lower than

those actually measured. Note that the calculated iron concentration is highly sensitive to the rate of siderite dissolution.

Another hypothesis that has been tested to explain the behavior of iron is the dissolution of Fougerite (green rust, $Fe_{6.7}Mg_{5.3}O_{34}H_{26.7}C_3$) (see Section 5.2.2). The dissolution of green rust leads to a better match between computed and measured iron concentration, although this process is highly redox dependent, and it must be remembered that a large uncertainty exists regarding the iron data and redox conditions at the site. Further determinations of the redox condition of groundwater at the ZERT site would be useful to validate the hypothesis that dissolution green rust controls the evolution of iron.

It should be noted that the desorption of Fe^{+2} sorbed onto HFO (which is known to take place under suboxic but not necessarily strongly reducing conditions, e.g., Hiemstra and van Riemsdijk, 2007) could also contribute to increasing Fe concentrations in groundwater. Preliminary simulations including this process showed a larger than observed Fe concentration increase in groundwater upon pH decrease. Given the limited amount of field data and uncertainties regarding redox conditions at the site, further modeling work including this process was not attempted.

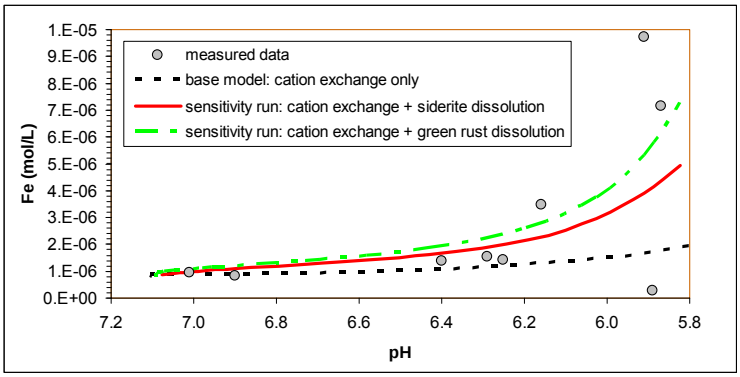

Figure 5.15. *Calculated iron concentration vs pH in the base model, in which only cation exchange is considered and a sensitivity run in which both cation exchange and siderite dissolution are considered*

Another effect from the dissolution of CO_2 in groundwater is the increase of aqueous bicarbonate (HCO_3^-) concentration (Figure 5.16). This increase modifies the distribution of adsorbed anionic species on HFO. Table 5.16 lists the adsorbed concentrations associated with those ions considered in the surface complexation reactions on HFO. Desorption and adsorption constitutes the net effects of decreasing and increasing the concentrations for all relevant surface complexes. For example, the desorption/adsorption of As(V) can be represented by all relevant surface complexes including HFO_sH_2AsO_4, HFO_wH_2AsO_4, HFO_s$HAsO_4^-$ and HFO_w$HAsO_4^-$ (see Table 5.13). The total adsorbed concentration (represented as s_ $H_2AsO_4^-$ in Table 5.16) is the summation of the concentrations for all four complexes. Table 5.16 shows the initial (C^i) and final (C^f) adsorbed concentrations and their difference $C^f - C^i$. Negative values of $C^f - C^i$ indicate desorption, while positive values indicate adsorption. Initially, adsorbed carbonate occupies a large portion of the sorption sites (about 55%). The increase in HCO_3^- due to the dissolution of CO_2 leads to increased adsorption of carbonate on the HFO surface. As a result, some anionic species are displaced into the aqueous phase.

Table 5.16. *Initial (C^i) and final (C^f) adsorbed concentration and their difference $C^f - C^i$*

Adsorbed species	C^i	C^f	$C^f - C^i$
s_H^+	1.7E-03	2.0E-03	3.0E-04
s_ SO_4^{-2}	5.2E-07	2.1E-07	-3.1E-07
s_$HSeO_3^-$	9.4E-07	5.2E-07	-4.2E-07
s_MoO_4^{-2}	1.7E-09	1.0E-09	-7.1E-10
S_HCO_3^-	2.3E-03	3.0E-03	7.2E-04
s_ $H_2AsO_4^-$	8.5E-08	6.7E-08	-1.9E-08
s_ HPO_4^-	2.3E-04	2.3E-04	7.4E-07

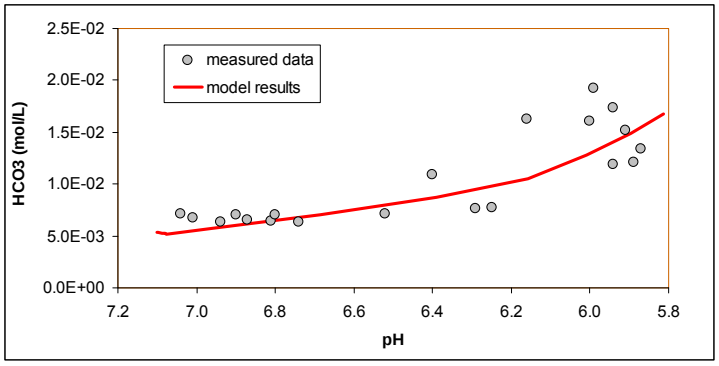

Figure 5.16. *Calculated bicarbonate concentration vs pH*

Figure 5.17 shows the aqueous concentration of arsenic. Even though scatter in the As data is large, the similarities between computed and measured As concentrations suggests carbonate-initiated desorption could be a controlling process for As, as observed in other systems (e.g., Appelo et al., 2002; Frau et al., 2008). It should be noted, however, that our model has ignored adsorption of As(III) species. This could affect model results. However, because As(III) does not sorb as much as As(V) and because significant As(III) is not expected in suboxic to oxic conditions at the site, it is unlikely that inclusion of As(III) in the system would significantly affect model results.

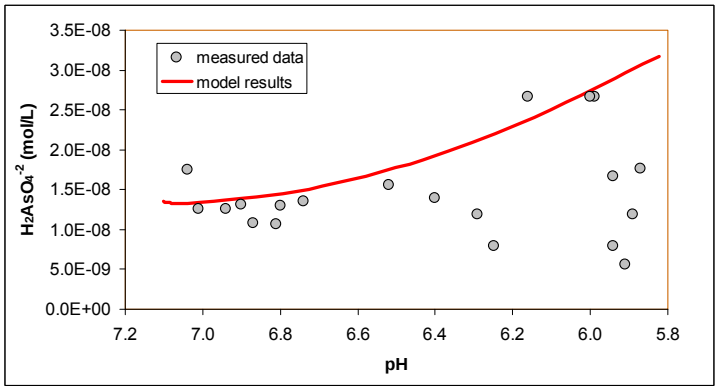

Figure 5.17 *Calculated arsenic concentration vs pH*

The computed aqueous concentrations of selenium overestimate the measured concentrations (Figure 5.18), possibly attributable either to uncertainties in the selenite surface-complexation constant, or to the omission of adsorbed selenate or selenide species. Preliminary EQ3 distribution of species modeling suggests that oligomeric neutral selenide complexes of Fe and Zn may predominate in solution, although such a distribution is highly dependent on a correct estimate of the redox state of the groundwater, and the unlikely assumption that homogeneous equilibrium with respect participating redox species has been attained. The concentration of aqueous phosphate (Figure 5.19) decreases with the decrease in pH, because anionic adsorption occurs. Although the concentrations of adsorbed HFO_sPO_4^{-2} and HFO_wPO_4^{-2} tend to decrease as carbonate species adsorb, the concentrations of HFO_sH_2PO_4 and HFO_wH_2PO_4 increase as the pH falls. This increase is greater than the decrease in HFO_sPO_4^{-2} and HFO_wPO_4^{-2}, thus the concentration of phosphate in the groundwater falls.

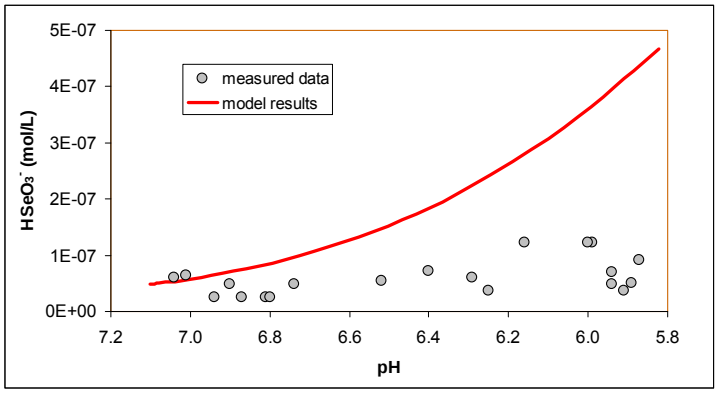

Figure 5.18 *Calculated selenium concentration vs pH*

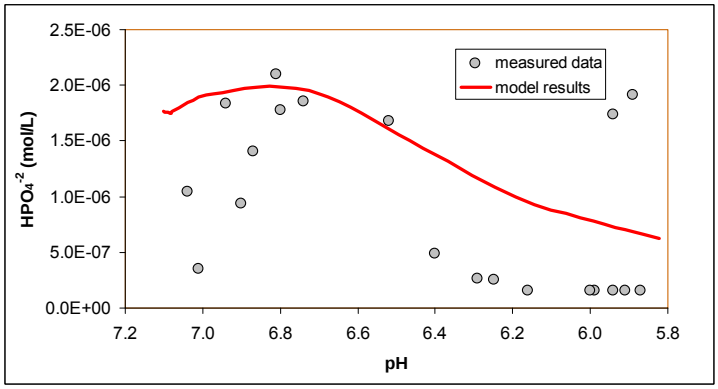

Figure 5.19 *Calculated phosphate concentration vs pH*

In summary, the concentration increase of major and trace elements in the groundwater at the MSU-ZERT field test has been interpreted with a batch geochemical model in which hypothesized reactive processes were tested, including the dissolution of calcite and Fe minerals, ion exchange, and sorption/desorption. These processes were presumed to take place on the basis of observed groundwater quality trends (Section 3) as well as statistical and thermodynamic evaluations

(Section 5.2). Only data before the first rainfall (after the start of the test) were used for comparing model results with observed trends, to avoid complexities resulting from the mixing of infiltrating rainwater with groundwater. Reasonable agreement between measured data and model results suggest that (1) calcite dissolution could be the primary process buffering pH, (2) the increase in the concentrations of major cations and trace metals except Fe could be explained by Ca^{+2}-driven exchange reactions, (3) the release of anions from adsorption sites due to competing adsorption of bicarbonate could explain the concentration trends of most anions and (4) the dissolution of reactive Fe minerals could explain the increase in total Fe concentration.

6. SUMMARY AND CONCLUDING REMARKS

The primary purpose of the MSU ZERT CO_2 release test conducted in summer 2008 was to allow controlled studies of near-surface CO_2 transport and detection technologies. However, this test also provided a unique opportunity to evaluate the effects of CO_2 release on the chemistry of ground-water at this site, which is the focus of this study.

When CO_2 dissolves in water, carbonic acid is produced, decreasing the pH and increasing the dissolved carbonate content of the water reacting with CO_2. These processes and their effects were monitored at the ZERT site, through geochemical investigations conducted prior to, during, and after the 2008 injection test. During this test, CO_2 was injected for 30 days into a shallow horizontal pipe installed at a depth near 1.8 m below ground surface, and about 0.5 m to 1 m below the water table. Groundwater chemistry was monitored from five locations, one upgradient and four downgradient of the injection pipe. Over 60 groundwater samples were collected. Most of these samples were obtained from shallow wells screened at depths close the soil-groundwater interface.

The samples showed a fast response to the CO_2 release, as early as a day after start of injection in nearby wells. The response was marked primarily by a pH decrease from ambient values ~ 7 to minimum values ~5.8 at wells closest to the injection well (within 1–2 m from it), and a significant increase in alkalinity and electrical conductivity. The concentrations of many dissolved species, including trace metals, also increased. Volatile organics were also detected in groundwater as the result of CO_2 injection, but were found to be linked to the CO_2 source and not to CO_2-sediment interactions. Concentrations of constituents listed on the EPA priority pollutant risks (US EPA, 2004), however, did not rise above their established maximum contaminant levels (MCL). Several samples were also collected from deeper wells screened at levels below the level of the injection pipe. These samples, however, have not been affected by the CO_2 release. Several rainfall events occurred during the test. Because of the thin vadose zone, water levels and water chemistry were quick to respond to rainfall (within a day or more). In particular, the concentrations of Fe and Mn in groundwater were observed to drop at the onset of rainfall, presumably as the result of groundwater mixing with more oxic recharge water. For these reasons, the interpretation of geochemical system response to CO_2 injection concentrated on the first week of CO_2 injection, during which time the test was not affected by rainfall.

Standard geochemical evaluations, statistical analyses, and geochemical modeling suggest that:

- CO_2 dissolution in the groundwater causes calcite to dissolve. Calculations of the calcite saturation index indicate increasing undersaturation with increasing CO_2 uptake, with slow calcite dissolution and incomplete resaturation during the first ten days of the test.

- Observed increases in the concentration of dissolved trace metals result likely from Ca^{+2}-driven ion exchange with clays (smectites) and sorption/desorption reactions likely involving Fe (hydr)oxides.
- Bicarbonate from CO_2 dissolution appears to compete for sorption with anionic species such as $HAsO_4^{-2}$, potentially increasing dissolved As levels in groundwater.

In particular, principal component analyses (PCA) for the first 10 days of the test, using the collected groundwater quality data show that:

- A strong correlation exists between alkali metals (Li, Na, K), alkali earths (Mg, Ca, Sr, Ba), B, Al, Cr, SiO_2(aq), Cd and Pb, and an inverse relationship to pH, suggesting ion exchange as a release mechanism for these cationic species.
- F, As, Se, and Mo are correlated, suggesting possible adsorption of these anionic species on secondary iron (hydr)oxides or anionic clays.
- PO_4 is negatively correlated with Mn, Fe, and Co, suggesting some precipitation/dissolution mechanism may be operative.
- Cl and SO_4^{-2} are correlated and suggest perturbation by earlier rainfall events, prior to monitoring.

Thermodynamic analyses indicate that:

- The initial groundwater is slightly undersaturated with respect to calcite, opal-CT and barite, suggesting dilution of the groundwater by rainwater prior to the test.
- The calculated redox potential is at pe ≈ +9 assuming fougerite-CO_3 and $Fe(OH)_3$ (ferrihydrite) as the controlling phases, and pe ≈ 2 if assuming goethite. There are indications that the system redox state may not be in equilibrium or spatially homogeneous.

Geochemical simulations were run to test whether ion exchange and sorption processes, together with dissolution of carbonates, could explain the water chemistry trends observed during the test. Results show reasonable agreement with field data, suggesting these processes were triggered by the CO_2 release. Because of the lack of site-specific data for key model parameters such as the cation exchange capacity, smectite and iron oxyhydroxide content, sorption data, mineral surface areas, and redox state, the simulations relied on assumed and/or typical but not site-specific values for these critical parameters. In addition, no unique solution may exist for a system as complex as at the ZERT site, for which multiple combinations of input parameters and modeled processes could yield similar results. Consequently, the modeling effort should be regarded as providing more qualitative than quantitative results.

It is evident that further detailed characterization of sediments and groundwater samples, including redox-sensitive sampling and analysis, would be required to test some of the hypotheses made in this study, and to provide a full understanding of metal behavior and speciation in this complex system. Such detailed analysis, however, is not within the scope of this study. Ongoing investigations, including the analyses of metals in sequential extractions of sediment samples, may prove quite useful to determine the association of metals with solid phases in the sediment. Such associations are critical as they are expected to dictate the magnitude and type (dissolution, desorption, exchange) of groundwater quality response to CO_2 injection.

It should be noted that this study was conducted in a shallow water-table aquifer under conditions that are not representative of deeper USDW. However, the collected geochemical data during this study were useful to evaluate key processes (dissolution, exchange, and sorption/desorption reactions) that would be expected to take place in any aquifer impacted by CO_2. It is anticipated that higher pressures in deep USDW would result in increased CO_2 dissolution in groundwater, relative to observations at the ZERT site, and thus could result in a more pronounced pH decrease and possibly a more significant release of contaminants. Such stronger response has indeed been observed during CO_2 injection tests in reservoirs at much greater depths, such at the Frio test site (Kharaka et al., 2009b). Furthermore, the controlled-release period of about four weeks may have been too short to test the importance of slower release mechanisms for trace metals, such as the dissolution minerals containing trace amounts of metals. We recommend conducting further controlled-release experiments to improve our understanding of possible groundwater contamination from CO_2 intrusion, ideally in deeper aquifers more representative of the majority of our groundwater resources, and with longer injection period to monitor contaminant release from short-term and long-term geochemical processes.

The possible impact of increased CO_2 dissolution in groundwaters at greater depth could be partly mitigated when impacted waters migrate upward from deeper formations, releasing CO_2 as the hydrostatic pressure decreases. It has long been known, for example, that the exsolution of CO_2 from naturally CO_2-rich and metal-rich thermal waters upon ascension to shallow depths is accompanied by a pH increase that causes the precipitation of calcite and other metal-bearing phases (e.g., Drummond and Ohmoto, 1985; Spycher and Reed, 1989). The effect of CO_2 exsolution along smaller temperature gradients but higher pressure gradients in the case of CCS (relative to thermal waters) has not been evaluated, but it would be anticipated to at least partly reverse the trends predicted in this study. Therefore, the full assessment of CCS impacts on the quality of a USDW may require assessing geochemical processes not only at the source of a CO_2 leak, but also along the path of impacted (carbonated) waters as they migrate towards potential receptors.

7. ACKNOWLEDGMENTS and Disclaimer

This work was conducted as part of the ZERT project, supported by the Assistant Secretary for Fossil Energy, Office of Sequestration, Hydrogen, and Clean Coal Fuels, through the National Energy Technology Laboratory, U.S. Department of Energy, under Contract No. DE-AC02-05CH11231. This research was conducted at the ZERT field facility directed by Lee Spangler and managed by Laura Dobeck, MSU, Bozeman, MT. http://www.montana.edu/zert. We thank the entire ZERT team and participating organizations for creating a supportive and exciting research environment, and gratefully acknowledge. This research was funded primarily by the Electric Power Research Institute, EPRI; additional funds were also obtained from EPA, DOE, LBNL, and USGS.

The USGS contributions to this report have not undergone formal internal review and approval for publication by the USGS; therefore, these contributions are subject to change and alternative interpretation.

8. REFERENCES

Abdelmoula, M, Trolard, F, Bourrié, G, and Génin, J-MR. (1998) Evidence for the Fe(II)-Fe(III) green rust "fougerite" mineral occurrence in a hydromorphic soil and its transformation with depth. Hyperfine Interactions 112, 235–238.

Appelo, CJA and Postma, D. (1994) Geochemistry, groundwater and pollution. A.A.Balkema, Rotterdam, Netherlands.

Appelo, CA, Venderwieden, MJJ, Tournassat, C and Charlet, L. (2002) Surface complexation of ferrous iron and carbonate on ferrihydrite and the mobilization of arsenic. Environ. Sci. Technol., 36, 3096-3103.

Baas Becking, LGM, Kaplan, LR and Moore, D. (1960) Limits of the natural environment in terms of pH and oxidation- reduction potentials. *J. Geol. 68*, 243–284.

Back, W, Hanshaw, BB, Plummer, LN, Rahn, PH, Rightmire, CT and Rubin, M. (1983) Process and rate of dedolomitization; mass transfer and 14 C dating in a regional carbonate aquifer. GSA Bulletin, 94(12), 1415–1429.

Bernal, JD, Dasgupta, DR and Mackay, AL. (1959) The oxides and hydroxides of iron and their structural interrelations. Clay Miner. Bull, 4, 15-30.

Birkholzer, J, Apps, JA, Zheng, L, Zhang, Y, Xu, T, and Tsang, C-F. (2008) Research project on CO_2 geological storage and groundwater resources: water quality effects caused by CO_2 intrusion into shallow groundwater. Lawrence Berkeley National Laboratory Technical Report, LBNL-1251E, 450 p., Available online at: http://www.osti.gov/bridge/product.biblio.jsp?query_id=0&page=0&osti_id=944435

Bourrie, G, Trolard, F, Genin, J-MR, Jaffrezic, A, Maître, V and Abdelmoula, M. (1999) Iron control by equilibria between hydroxygreen rusts and solutions in hydromorphic soils. Geochim. Cosmochim. Acta 63, 3417-3427.

Bourrie, G, Trolard, F, Refait, P and Feder, F. (2004) A solid solution model for Fe(II)-Fe(III)-Mg(II) green rusts and fougerite and estimation of their Gibbs free energies of formation. Clays and Clay Minerals 52, 383-395.

Bradbury, MH and Baeyens, B. (1997) A mechanistic description of Ni and Zn sorption on Na-montmorillonite, part II: modelling. *J. Contaminant Hydrology*, 27, 223-248.

Braun, RD. (1991) Solubility of iron(II) carbonate at temperature between 30 and 80^{o}, *Talanta,* 38(2), 205-211.

Busenberg, E and Plummer, LN. (1989) Thermodynamics of magnesian calcite solid-solutions at 25°C and 1 atm total pressure. Geochimica et Cosmochimica Acta Vol5. 3, pp. 1189-1208.

Charlet, L and Tournassat, C. (2005) Fe(II)–Na(I)–Ca(II) Cation Exchange on Montmorillonite in Chloride Medium: Evidence for Preferential Clay Adsorption of Chloride – Metal Ion Pairs in Seawater. Aquatic Geochemistry, 11, 115-137.

Christiansen, BC, Balic-Zunic, T, Petit, P-O, Frandsen, C, Mørup d, S, Geckeis, H, Katerinopoulou, A and Svane Stipp, SL. (2009) Composition and structure of an iron-bearing, layered double hydroxide (LDH) Green rust sodium sulphate. Geochimica et Cosmochimica Acta 73, 3579-3592.

Dasgupta, DR and Mackay, AL. (1959) β-ferric oxyhydroxide and green rust. Journal of the Physical Society of Japan 14, pp. 932-935.

Dobrzynski, D. (2007) Chemical diversity of groundwater in the Carboniferous–Permian aquifer in the UnisΠaw Âlàski – SokoΠowsko area (the Sudetes, Poland); a geochemical modelling approach. Acta Geologica Polonica, Vol. 57, No. 1, pp. 97-112.

Drissi, SH, Refait, Ph, Abdelmoula, M and Genin, J-MR. (1995) Preparation and thermo-dynamic properties of Fe(II)-Fe(III) hydroxide- carbonate (green rust one): Pourbaix diagram of iron in carbonate-containing aqueous media. Corrosion Science 37, 2025-2041.

Duckworth, OW and Martin, ST. (2004) Role of molecular oxygen in the dissolution of siderite and rhodochrosite. Geochimica et Cosmochimica Acta 68(3), 607-621.

Drummond, SE and Ohmoto, H. (1985) Chemical evolution and mineral deposition in boiling hydrothermal systems. Economic Geology, 80: 1427-1439.

Dzombak, DA and Morel, FMM. (1990) Surface complexation modeling-hydrous ferric oxide, John Wiley & sons, New York, 393 pp.

Edmunds, WM, Bath, AH and Miles, DL. (1982) Hydrochemical evolution of the East Midlands Triassic sandstone aquifer, England. Geochimica et Cosmochimica Acta 46, 2069–2081.

Feder, F, Trolard, F, Klingelhofer, G and Bourrie, G. (2005) In situ Mossbauer spectroscopy: Evidence for green rust (fougerite) in a gleysol and its mineralogical transformations with time and depth. Geochimica et Cosmochimica Acta, Vol. 69, No. 18, pp. 4463-4483.

Frau, F, Biddau, R and Fanfani, L. (2008) Effect of major anions on arsenate desorption from ferrihydrite-bearing natural samples. Applied Geochemistry 23, 1451–1466.

Freifeld, BM, Trautz, RC, Kharaka, YK, Phelps, TJ, Myer, LR, Hovorka, SD and Collins DJ. (2005) The U-tube: A novel system for acquiring borehole fluid samples from a deep geologic CO_2 sequestration experiment. J Geophy Res 110:B10203, doi: 10.1029/2005JB003735.

Genin, J-MR, Bourrie, G, Trolard, F, Abdelmoula, M, Jaffrezic, A, Refait, Ph, Maître, V, Humbert, B and Herbillon, AJ. (1998) Thermodynamic equilibria in aqueous suspensions of synthetic and natural Fe(II)-Fe(III) green rusts: occurrences of the mineral in hydromorphic soils. Environmental Science and Technology 32, 1058 -1068.

Genin, J-MR, Ruby, C and Upadhyay, C. (2006) Structure and thermodynamics of ferrous, stoichiometric and ferric oxyhydroxycarbonate green rusts; redox flexibility and fougerite mineral. Solid State Sciences 8, 1330-1343.

Genin, J-MR, Olowe, AA, Refait, P and Simon, L. (1996) On the stoichiometry and Pourbaix diagram of Fe(II) Fe(III) hydroxyl-sulphate or sulphate containing green rust 2: an electrochemical and spectroscopy study. Corros. Sci. 38, 1751-1762.

Gledhill, DK and Morse, JW. (2006) Calcite dissolution kinetics in Na–Ca–Mg–Cl brines. Geochimica et Cosmochimica Acta, 70: 5802-5813.

Golubev, SV, Bénézeth, P, Schott, J, Dandurand, J-L and Castillo, A. (in press) Siderite dissolution kinetics in acidic aqueous solutions from 25 to 100 °C and 0 to 50 atm P(CO_2). Chemical Geology, Special Issue on CO_2 geological sequestration.

Hem, JD. (1985) Study and interpretation of the chemical characteristics of natural water. U.S. Geological Survey Water-Supply Paper 2254, 264 pp.

Hiemstra, T and van Riemsdijk, WH. (2007) Adsorption and surface oxidation of Fe(II) on metal (hydr)oxides. Geochimica et Cosmochimica Acta, 71, 5913–5933.

Hopkins, J and Putnam, P. (2000) Fabric alteration and isotopic signature of carbonates in a recharge area of the Madison Aquifer, Montana, USA. Journal of Geochemical Exploration, 69–70, 235–238.

Hovorka, SD, Benson, SM, Doughty, CK, Freifeld, BM, Sakurai, S, Daley, TM, Kharaka, YK, Holtz, MH, Trautz, RC, Nance, HS, Myer, LR and Knauss, KG. (2006) Measuring permanence of CO_2 storage in saline formations – the Frio Experiment. Environmental Geosciences 13:105-121.

Intergovernmental Panel on Climate Change (IPCC). (2007) Working Group Assessment Report, URL http://www.ipcc.ch/(working groups I, II, III and Synthesis Reports.

James, NP, Bone, Y and Kyser, TK. (1993) Shallow burial dolomitization and dedolomitization of mid-Cenozoic, cool-water, calcitic, deep-self limestones, Southern Australia. Journal of Sedimentary Petrology, 63(3) (May), 528–538.

Jordan, G and Rammensee, W. (1998) Dissolution rates of calcite (1014) obtained by scanning force microscopy: Microtopography-based dissolution kinetics on surfaces with anisotropic step velocities. Geochimica et Cosmochimica Acta, 62, 941-947.

Kaufmann, G and Dreybrodt, W. (2007) Calcite dissolution kinetics in the system $CaCO_3$–H_2O–CO_2 at high undersaturation. Geochimica et Cosmochimica Acta, 71, 1398-1410.

Kendy, E. (2001) Magnitude, extent, and potential sources of nitrate in ground water in the Gallatin Local Water Quality District, Southwestern Montana, 1997-98. U.S. Geological Survey, Water-Resources Investigations Report 01-4037, 66 pp.

Kendy, E and Tresch, RE. (1996) Geographic, geologic and hydrologic summaries of intermontane basins of the Northern Rocky Mountains, Montana. U.S. Geological Survey Water-Resources Investigations Report 96-4025, 232 pp.

Kharaka, YK and Hanor, JS. (2007) Deep Fluids in the continents: I. Sedimentary Basins. In, J.I. Drever (ed.), Surface and Ground Water, Weathering and Soils, Treatise on Geochemistry, v. 5, p. 1-48.

Kharaka, YK, Gunter, WD, Aggarwal, PK, Perkins, EH and DeBraal, JD. (1988) SOLMINEQ.88: A computer program for geochemical modeling of water-rock interactions. U.S. Geological Survey Water Resources Invest. Rep. 88–4227.

Kharaka, YK, Cole, DR, Hovorka, SD, Gunter, WD, Knauss, KG and Freifeld, BM. (2006) Gas-Water-Rock Interactions in Frio Formation Following CO_2 Injection: Implications to the Storage of Greenhouse Gases in Sedimentary Basins. Geology 34:577-580.

Kharaka, YK, Thordsen, JJ, Kakouros, E, Ambats, G, Herkelrath, WN, Birkholzer, JT, Apps, JA, Spycher, NF, Zheng, L, Trautz, RC, Rauch, HW and Gullickson, K. (submitted 2009a) Changes in the Chemistry of Shallow Groundwater Related to the 2008 Injection of CO_2 at the ZERT Field Site, Bozeman, Montana, Environmental Earth Sciences.

Kharaka, YK, Thordsen, JJ, Hovorka, SD, Nance, HS, Cole, DR, Phelps, TJ and Knauss, KG. (2009b) Potential environmental issues of CO_2 storage in deep saline aquifers: Geochemical results from the Frio-I Brine Pilot test, Texas, USA. Applied Geochemistry 24:1106-1112.

Kwon, S-K, Kimijima, K, Kanie, K, Suzuki, S, Muramatsu, A, Saito, M, Shinoda, K and Waseda, Y. (2007) Influence of silicate ions on the formation of goethite from green rust in aqueous solution. Corrosion Science 49, 2946-2961.

Lasaga, AC, Soler, JM, Ganor, J, Burch, TE and Nagy, KL. (1994) Chemical weathering rate laws and global geochemical cycles. Geochimica et Cosmochimica Acta, 58, 2361-2368.

Lewicki, J, Oldenburg, C, et al. (2007) Surface CO_2 leakage during the first shallow subsurface CO_2 release experiment. Geophys Res Lett 34:L24402.

Lewicki, JL, Hilley, GE, Dobeck, L and Spangler, L. (2009) Dynamics of CO_2 fluxes and concentrations during a shallow subsurface CO_2 release, Environmental Earth Sciences, submitted.

Lindberg, RD and Runnels, DD. (1984) Ground water redox reactions: An analysis of equilibrium state applied to Eh measurements and geochemical modeling. Science, 225, 925–927.

Lonn, JD and English, AR. (2002) Preliminary geologic map of the eastern part of the Gallatin Valley, Montana. Montana Bureau of Mines and Geology Open File Report 457, 20 pp.

Majzlan, J, Navrotsky, A and Schwertmann, U. (2004) Thermodynamics of Fe oxides: Part III. Enthalpies of formation and stability of ferrihydrite (~Fe(OH)3), schwertmannite (~FeO(OH)3/4(SO4)1/8), and e-Fe2O3. Geochimica et Cosmochimica Acta, 68(5), 1049–1059.

Muller, B and Sigg, L. (1991) Adsorption of lead(ll) on the goethite surface: voltammetric evaluation of surface complexation parameters. Journal of Colloid and Interface Science, 148(2), 517-532.

Oldenburg, CM, Lewicki, JL, Dobeck, L and Spangler, L. (2009) Modeling Gas Transport in the Shallow Subsurface During the ZERT CO_2 Release Test. Transport in Porous Media, doi: 10.1007/s11242-009-9361-x.

Olowe, AA and Genin, J-MR. (1991) The mechanism of oxidation of Fe(II) hydroxide in sulphated aqueous media: importance of the initial ratio of the reactants. Corros. Sci. 32, 965-984.

Pacheco, FAL and Szocs, T. (2006) "Dedolomitization reactions" driven by anthropogenic activity on loessy sediments, SW Hungary. Applied Geochemistry 21, 614–631.

Parkhurst, DL and Appelo, CAJ. (1999) User's guide to PHREEQC (version 2)—A computer program for speciation, batch-reaction, one-dimensional transport, and inverse geochemical calculations. U.S. Geological Survey Water-Resources Investigations Report 99-4259, Denver, CO, Http://Wwwbrr.Cr.Usgs.Gov/Projects/GWC_Coupled/Phreeqc/Html/Final.Html

Pokrovsky, OS, Golubev, SV and Schott, J. (2005) Dissolution kinetics of calcite, dolomite and magnesite at 25 ^{o}C and 0 to 50 atm P(CO_2). Chemical Geology, 217, 239-255.

Preis, W and Gamsjager, H. (2002) Critical evaluation of solubility data: enthalpy of formation of siderite. Phys. Chem. Chem. Phys., 4, 4014-4019.

Refait P and Genin J. (1993) The oxidation of Fe(II) hydroxide in chloride-containing aqueous media and Pourbaix diagrams of green rust one. Corrosion Science 34, 797-819.

Rock, P.A., G.K. Mandell, W.H. Casey, and E.M. Walling (2001), Gibbs energy of formation of dolomite from electrochemical cell measurements and theoretical calculations. *Am. J. Sci., 301*, 103–111.

Ruby, C, Upadhyay, C, Gehin A, Ona-Nguema, G and Genin, J-MR. (2006) In Situ Redox Flexibility of FeII-III Oxyhydroxycarbonate Green Rust and Fougerite. Environ. Sci. Technol., 40, 4696-4702.

Samper, J, Zheng, L, Fernández, AM, and Montenegro, L. (2008) Inverse modeling of multicomponent reactive transport through single and dual porosity media. Journal of Contaminant Hydrology, 98(3-4), 115-127.

Schwab, RG, Pimpl, TH, Schukow, H and Breitinger, DK. (2000) Compounds of the crandallite type; Material from the earth on its way to technical application. Earth Science Frontiers (China University of Geosciences, Beijing), 7(2), 485-497.

Schwertmann, U and Fechter, H. (1994) The formation of green rust and its transformation to lepidocrocite. Clay Minerals 29, 87-92.

Shlens, J. (2009) A Tutorial on Principal Component Analysis. Version 3.01, April 22, 2009, 12 p. Published by the Center for Neural Science, New York University, New York City, NY 10003-6603. (Available for downloading from the Web.)

Sileo, EE, Alvarez, M, Rueda, EH. (2001) Structural studies on the manganese for iron substitution in the synthetic goethite–jacobsite system. International Journal of Inorganic Materials 3, 271–279.

Spangler, LH, Dobeck, LM, Nehrir, A, Humphries, S, Barr, J, Keith, C, Dhaw, J, Rouse, J, Cunningham, A, Benson, S, Oldenburg, C, Lewicki, J, Wells, A, Diehl, R, Strazisar, B, Fessenden, J, Rahn, T, Amonette, J, Barr, J, Pickles, W, Jacobson, J, Silver, E, Male, E, Rauch,

H, Gullickson, K, Trautz, R, Kharaka, Y, Birkholzer, J and Wielopolski, L. (submitted 2009) A controlled field pilot in Bozeman, Montana, USA, for testing near surface CO_2 detection techniques and transport models. Environmental Earth Sciences.

Spycher, NF and Reed, MH. (1989) Evolution of a Broadlands-type epithermal ore fluid along alternative P-T paths: implications for the transport and deposition of base, precious and volatile metals. Economic Geology 84: 328-359.

Steefel, CI, Carroll, S, Zhao, P and Roberts, S. (2003) Cesium migration in Hanford sediment: a multisite cation exchange model based on laboratory transport experiments, Journal of Contaminant Hydrology, 67(1-4), 219-246.

Steefel, CI and Lasaga, AC. (1994) A coupled model for transport of multiple chemical species and kinetic precipitation/dissolution reactions with applications to reactive flow in single phase hydrothermal system. Am. J. Sci, 294, 529–592.

Stefansson, A, Arnorsson, S and Sveinbjornsdottir, AE. (2005) Redox reactions and potentials in natural waters at disequilibrium. *Chemical Geology, 221*, 289–311.

Strazisar, BR. (2009) Personal Communication.

Strazisar, BR, Wells, AW, Diehl, JR, Hammack, RW and Veloski, GA. (2009) Near-surface monitoring for the ZERT shallow CO_2 injection project. Int. J. Greenhouse Gas Control, doi:10.1016/j.ijggc.2009.07.005.

Svensson, U and Dreybrodt, W. (1992) Dissolution kinetics of natural calcite minerals in CO_2-water systems approaching calcite equilibrium. Chemical Geology, 100, 129-145.

Testemale, D, Dufaud, F, Martinez, I, Bénézeth, P, Hazemann, J-L, Schott, J and Guyot, F. (2009) An X-ray absorption study of the dissolution of siderite at 300 bar between 50 °C and 100 °C. Chemical Geology, 259, 8-16.

Thordsen, JK. (2009) ZERT Well 8 (&8B) Summary of Mineralogy. Internal memorandum dated 2-12-09, United States Geological Survey.

Trolard, F, Abdelmoula, M, Bourrié, G, Humbert, B and Génin, J-MR. (1996) Mise en évidence d'un constituant de type rouilles vertes" dans les sols hydromorphes. Proposition de l'existence d'un nouveau minéral: la "fougérite". Comptes Rendus de l'Académie des Sciences 323, 1015–1022.

U.S. Environmental Protection Agency. (2003) Purge-and-Trap for Aqueous Samples, Method 5030C at: http://www.epa.gov/osw/hazard/testmethods/sw846/new_meth.htm#5030C

U.S. Environmental Protection Agency. (2004) 2004 edition of the drinking water standards and health advisories. EPA 822-R-04-005.

U.S. United States Environmental Protection Agency. (2008) Federal Requirements under the Underground Injection Control (UIC) Program for Carbon Dioxide (CO_2) Geologic Sequestration (GS) Wells, Proposed Rule, 40 CFR Parts 144 and 146, EPA-HQ-OW-2008-0390. Available online at http://www.epa.gov/fedrgstr/EPA-WATER/2008/July/Day-25/w16626.htm.

Villinski, JE, O'Day, PA, Barger, JR and Conklin, MH. (2000) Reductive dissolution of MnO2 by Fe(II): Effects of chemical gradients and intermediate phase structural information. In Chemical

Speciation and Reactivity in Water Chemistry and water Technology: A Symposium in Honor of James J. Morgan (J. Hering and J.L. Schnoor, Organizers). Preprints of extended Abstracts, Vol 40, No. 2, p. 630-633. Presented before the Division of Environmental Chemistry, American Chemical Society, Washington, D.C.

Wang, S and Jaffe, PR. (2004) Dissolution of trace metals in potable aquifers due to CO_2 releases from deep formations. Energy Conversion and Management 45:2833–2848.

Washington, JW, Endale, DM, Samarkina, LP and Chappell, KE. (2004) Kinetic control of oxidation state at thermodynamically buffered potentials in subsurface waters. Geochim. et Cosmochim. Acta 68(23), 4831–4842.

Williams, AGB and Scherer, M. (2001) Kinetics of Cr(VI) reduction by carbonate green rust. Environmental Science and Technology, vol. 35, n°17, pp. 3488-3494.

Wolery, TJ. (1992) EQ3NR, A computer program for geochemical aqueous speciation-solubility calculations: Theoretical manual, user's guide, and related documentation (Version 7.0). Lawrence Livermore National Lab. UCRL-MA-110662 PT III.

Wolery, TJ. (1993) EQ3/6, A software package for geochemical modelling of aqueous systems (Version 7.2). Lawrence Livermore Nat. Lab. UCRL-MA 110662.

Wolery, TJ and Jareck, RL. (2003) EQ3/6, Version 8.0, Software's user manual. Software identification number: 10813-UM-8.0-00, U.S. Department of Energy, Office of Civilian Radioactive Waste Management, Office of Repository Development, 1261 Town Center Drive, Las Vegas, NV, 89144.

Wolery, TJ and Jove-Colon, C. (2007) Qualification of Thermodynamic Data for Geochemical Modeling of Mineral-Water Interactions in Dilute Systems. ANL-WIS-GS-000003 REV 01. Las Vegas, Nevada: Sandia National Laboratories. ACC: DOC.20070619.0007.

Xu, T, Sonnenthal, E, Spycher, N, Pruess, K. (2006) TOUGHREACT: A simulation program for non-isothermal multiphase reactive geochemical transport in variably saturated geologic media. Computers and Geosciences 32:145-165.

Zheng, L, Apps, J, Spycher, N, Birkholzer, J, Kharaka, YK, Thordsen, J, Kakouros, E, Trautz, R, Rauch, H and Gullickson, K. (2009a) Changes in shallow groundwater chemistry at the 2008 ZERT CO_2 injection experiment: II- Modeling analysis. Abstract, Eight Carbon Capture and Sequestration Conference. Pittsburgh, PA.

Zheng, L, Apps, JA, Zhang, Y, Xu, T and Birkholzer, JT. (2009b) On mobilization of lead and arsenic in groundwater in response to CO_2 leakage from deep geological storage. Chemical Geology, DOI: 10.1016/j.chemgeo.2009.09.007.

Zheng, L, Samper, J, Montenegro L and Fernández, AM. (2009c) A coupled THMC model of a heating and hydration laboratory experiment in unsaturated compacted FEBEX bentonite, Journal of Hydrology.

Zheng, L and Samper, J. (2009) A coupled THMC model of FEBEX mock-up test. Physics and Chemistry of the Earth, 33, S486-S498, submitted.

Zhu, C, Veblen, DR, Blum, AE, Chipera, SJ. (2006) Naturally weathered feldspar surfaces in the Navajo Sandstone aquifer, Black Mesa, Arizona: Electron microscopic characterization. Geochimica et Cosmochimica Acta 70, 4600–4616.

APPENDIX A

Table A1 *Chemical composition of water samples from ZERT monitoring wells*

MW1

						Major Solutes (mg/L)																Trace Solutes (µg/L)												
SAMPLE	DATE	time	EC	pH	T	HCO_3	Na	K	Mg	Ca	Sr	Ba	Mn	Fe	F	Cl	Br	NO_3	PO_4	SO_4	SiO_2	TDS	Al	As	B	Cd	Co	Cr	Cu	Li	Mo	Pb	Se	U	Zn
08ZERT-**103**	7/7/08	17:00		6.8	10	432	9.2	5.5	24	95	0.31	0.12	0.001	<0.01	0.10	3.7	0.042	0.79	0.17	5.8	27	37	2	1.0	0.009	0.09	0.3	0.4	1.5	0.003	0.3	<0.02	<2	4.9	4.0

MW2

						Major Solutes (mg/L)																Trace Solutes (µg/L)												
SAMPLE	DATE	time	EC	pH	T	HCO_3	Na	K	Mg	Ca	Sr	Ba	Mn	Fe	F	Cl	Br	NO_3	PO_4	SO_4	SiO_2	TDS	Al	As	B	Cd	Co	Cr	Cu	Li	Mo	Pb	Se	U	Zn
08ZERT-**102**	7/7/08	15:30		6.8	10	396	7.5	6.2	24	85	0.27	0.13	0.002	<0.01	0.09	6.5	0.051	0.12	0.20	8.3	27	42	2	0.8	0.012	0.07	<0.2	<0.4	1.4	0.003	0.4	<0.02	<2	4.3	3.4

1A

						Major Solutes (mg/L)																Trace Solutes (µg/L)												
SAMPLE	DATE	time	EC	pH	T	HCO_3	Na	K	Mg	Ca	Sr	Ba	Mn	Fe	F	Cl	Br	NO_3	PO_4	SO_4	SiO_2	TDS	Al	As	B	Cd	Co	Cr	Cu	Li	Mo	Pb	Se	U	Zn
08ZERT-**105**	7/8/08	9:15	588	6.9	8	386	7.8	5.6	23	84	0.27	0.11	0.001	<0.01	0.10	4.7	0.040	0.55	0.17	7.5	26	39	2	0.9	0.012	0.08	<0.2	<0.4	1.2	0.003	0.4	0.02	<2	4.0	2.8

1B

						Major Solutes (mg/L)																Trace Solutes (µg/L)												
SAMPLE	DATE	time	EC	pH	T	HCO_3	Na	K	Mg	Ca	Sr	Ba	Mn	Fe	F	Cl	Br	NO_3	PO_4	SO_4	SiO_2	TDS	Al	As	B	Cd	Co	Cr	Cu	Li	Mo	Pb	Se	U	Zn
08ZERT-**112**	7/10/08	15:15	650	6.5	13	438	8.4	6.0	26	94	0.29	0.11	0.003	<0.01	0.14	4.9	0.049	0.33	0.16	7.1	34	46	3	1.2	0.018	0.28	0.3	15	1.7	0.006	0.4	0.06	5	4.2	4
08ZERT-**117**	7/12/08	9:15	847	5.7	9	551	9.4	6.8	34	124	0.39	0.15	0.003	<0.01	0.09	5.0	0.046	<0.01	0.14	7.3	37	49	4	1.2	0.022	0.38	0.3	30	1.9	0.007	0.4	0.06	5	4.0	3.6
08ZERT-**127**	7/15/08	10:00	1015	5.9	9	724	9.8	7.6	43	155	0.49	0.19	0.005	<0.013	0.11	5.2	0.046	0.31	0.17	7.7	41	54	5	1.3	0.021	0.43	0.4	51	2.1	0.008	1.0	0.08	6	4.6	3.2
08ZERT-**131**	7/17/08	10:30	1041	5.9	9	735	9.7	7.7	44	159	0.51	0.20	0.006	0.014	0.11	5.3	0.048	0.28	0.18	7.9	35	48	4	0.9	0.023	0.40	0.4	13	2.0	0.007	0.6	0.07	4	4.8	3.5
08ZERT-**135**	7/19/08	10:15	1124	6.1	10	821	9.9	8.1	46	174	0.55	0.22	0.017	0.017	0.12	5.5	0.055	0.26	0.19	8.1	37	51	4	1.2	0.017	0.21	0.5	5	2.1	0.005	0.3	0.05	3	5.0	2.6
08ZERT-**139**	7/21/08	9:50	1181	6.0	21	1000	9.4	7.7	44	173	0.53	0.21	0.021	<0.025	0.15	5.6	0.046	0.23	0.18	8.4	36	50	5	1.1	0.016	0.33	<0.25	18	2.2	0.007	0.4	0.06	<3	5.2	2.6
08ZERT-**144**	7/23/08	11:45	908	6.0	15	861	8.7	7.7	40	158	0.49	0.19	0.012	<0.013	0.12	5.6	0.052	0.23	0.17	8.4	34	49	3	1.0	0.013	0.20	0.4	2	2.2	0.005	0.4	0.05	3	4.8	4.0
08ZERT-**147**	7/26/08	9:30	667	5.9	13	565	7.6	6.2	26	109	0.33	0.12	0.005	<0.01	0.13	5.6	0.046	0.23	0.17	7.7	28	41	2	1.0	0.011	0.11	0.2	<0.4	1.9	0.004	0.5	0.05	<2	4.3	3.4
08ZERT-**151**	7/29/08	9:00	646	5.7	15	480	8.2	6.1	25	99	0.31	0.11	0.008	0.014	0.15	5.6	0.047	0.26	0.19	7.6	27	41	2	0.9	0.011	0.11	0.2	<0.4	1.5	0.004	0.3	0.03	<2	4.2	2.9
08ZERT-**160**	8/4/08	11:15	961	5.9	15	693	9.3	7.5	38	147	0.46	0.18	0.006	0.018	0.13	5.6	0.050	0.38	0.19	8.0	33	47	4	0.9	0.021	0.33	0.3	<0.5	1.9	0.006	0.4	0.06	4	3.9	2.6
08ZERT-**163**	8/7/08	9:00	984	5.9	15	702	9.2	7.7	38	149	0.47	0.19	0.006	0.04	0.10	5.6	0.056	0.48	0.20	8.1	38	52	3	1.1	0.017	0.15	0.3	0.9	1.8	0.005	0.3	0.03	3	4.0	2.5
08ZERT-**167**	8/8/08	9:00	954	5.8	13	668	9.0	7.7	36	147	0.46	0.18	0.006	0.030	0.11	5.6	0.059	0.50	0.20	8.0	38	52	4	1.0	0.019	0.20	0.3	16	1.8	0.006	0.3	0.04	<3	4.0	2.2
08ZERT-**171**	8/11/08	9:40	705	6.0	13	529	7.9	6.8	29	118	0.36	0.14	0.004	<0.01	0.11	5.8	0.062	0.51	0.18	8.0	34	48	3	0.8	0.016	0.19	0.3	12	1.9	0.006	0.3	0.04	<2	3.7	2.1
08ZERT-**176**	8/13/08	11:20	625	6.4	26	402	7.4	6.1	21	91	0.28	0.11	0.002	<0.006	0.12	5.9	0.062	0.68	0.20	7.8	30	45	3	1.0	0.016	0.19	0.2	7	1.7	0.005	0.5	0.02	3	4.1	1.6

2A

						Major Solutes (mg/L)																Trace Solutes (µg/L)												
SAMPLE	DATE	time	EC	pH	T	HCO_3	Na	K	Mg	Ca	Sr	Ba	Mn	Fe	F	Cl	Br	NO_3	PO_4	SO_4	SiO_2	TDS	Al	As	B	Cd	Co	Cr	Cu	Li	Mo	Pb	Se	U	Zn
08ZERT-**107**	7/8/08	11:45	585	6.7	8	387	7.5	5.3	24	84	0.26	0.11	0.001	<0.01	0.12	4.8	0.042	0.60	0.18	7.4	32	45	3	1.0	0.018	0.23	0.2	12	1.6	0.005	0.4	0.05	<4	4.1	3.1

2B

						Major Solutes (mg/L)																Trace Solutes (µg/L)												
SAMPLE	DATE	time	EC	pH	T	HCO_3	Na	K	Mg	Ca	Sr	Ba	Mn	Fe	F	Cl	Br	NO_3	PO_4	SO_4	SiO_2	TDS	Al	As	B	Cd	Co	Cr	Cu	Li	Mo	Pb	Se	U	Zn
08ZERT-**109**	7/9/08	9:00	651	7.0	12	434	9.1	5.4	28	92	0.30	0.10	0.028	<0.01	0.17	5.4	0.099	0.26	0.10	7.2	32	45	3	1.3	0.017	0.29	0.4	12	2.5	0.007	0.7	0.06	5	4.3	3.8
08ZERT-**118**	7/12/08	10:00	952	6.4	9	664	9.7	7.1	41	142	0.45	0.19	0.19	0.08	0.14	5.3	0.048	0.12	0.05	7.4	40	53	5	1.0	0.022	0.45	1.2	54	2.3	0.008	0.5	0.08	6	3.8	9.0
08ZERT-**128**	7/15/08	11:00	1270	5.9	9	816	10.1	8.3	54	204	0.63	0.27	0.13	0.39	0.07	5.5	0.049	0.20	0.02	7.7	44	57	7	1.3	0.024	0.61	1.2	72	2.6	0.010	0.5	0.10	7	4.5	3.2
08ZERT-**132**	7/17/08	11:15	1193	5.9	9	924	9.5	8.0	49	191	0.57	0.26	0.14	0.53	0.06	5.6	0.049	0.20	<0.015	7.8	37	51	6	0.4	0.020	0.43	1.2	21	2.2	0.007	0.5	0.06	<3	4.3	2.3
08ZERT-**136**	7/19/08	11:15	1342	6.0	10	1115	9.9	7.4	55	223	0.69	0.23	0.011	<0.025	0.05	5.5	0.056	0.25	0.24	8.4	38	52	6	0.9	0.017	0.22	0.5	7	2.4	0.007	<0.5	0.05	3	4.1	2.8
08ZERT-**140**	7/21/08	10:10	1335	6.0	16	1127	9.6	6.9	51	227	0.67	0.21	0.008	<0.025	0.09	5.5	0.047	0.30	0.26	8.4	37	51	8	1.1	0.021	0.40	<0.25	26	2.4	0.008	0.4	0.07	3	4.4	3.7
08ZERT-**146**	7/23/08	13:15	1424	6.0	15	1147	10.2	7.4	55	239	0.73	0.24	0.014	<0.025	0.13	5.6	0.051	0.35	0.26	8.6	39	54	8	1.6	0.018	0.22	0.6	1	2.4	0.007	0.7	0.06	4	4.4	3.5
08ZERT-**150**	7/26/08	11:35	1339	5.9	13	1054	9.6	7.1	47	241	0.68	0.22	0.015	<0.025	<0.05	5.6	0.047	0.41	0.02	8.5	30	45	7	1.5	<0.015	0.19	<0.5	<1.0	2.0	0.007	<0.75	<0.05	<5	4.0	4.0
08ZERT-**154**	7/29/08	13:45	1235	5.8	21	967	8.8	7.6	40	216	0.58	0.25	0.13	0.78	0.06	5.7	0.055	0.46	<0.015	8.0	29	44	5	1.2	<0.015	0.18	1.2	<1	1.5	0.006	0.2	<0.05	<5	4.0	4.4
08ZERT-**161**	8/4/08	12:15	1195	5.8	19	916	8.5	7.7	36	219	0.52	0.27	0.19	1.1	0.10	5.8	0.052	0.64	<0.015	7.8	38	53	10	0.4	0.020	0.32	1.3	41	1.9	0.006	0.4	<0.05	<3	4.0	3.5
08ZERT-**165**	8/7/08	10:45	1201	5.7	22	884	8.8	7.7	35	212	0.50	0.26	0.21	1.19	0.07	6.1	0.062	0.77	<0.015	8.0	38	53	8	0.5	0.016	0.23	1.5	7	2.0	0.005	0.3	0.03	3	4.1	4.2
08ZERT-**169**	8/8/08	11:25	732	6.0	21	511	7.1	5.9	20	125	0.29	0.15	0.13	0.87	0.18	6.3	0.065	1.0	<0.015	8.0	31	46	4	0.4	0.018	0.19	0.8	12	1.6	0.005	0.6	0.03	<2	4.1	2.8
08ZERT-**172**	8/11/08	10:20	615	5.8	14	451	7.2	5.4	17	106	0.25	0.12	0.090	0.35	0.24	6.5	0.070	1.1	0.023	7.9	29	45	3	0.5	0.014	0.14	0.6	13	1.7	0.004	0.5	0.02	<2	4.4	2.5
08ZERT-**177**	8/13/08	12:30	606	6.4	25	389	7.8	5.2	16	94	0.23	0.10	0.052	0.15	0.27	6.9	0.073	1.4	0.06	7.8	29	46	2	0.7	0.017	0.15	0.5	7	1.6	0.005	0.7	0.04	3	4.3	5.9

3B

						Major Solutes (mg/L)																Trace Solutes (µg/L)												
SAMPLE	DATE	time	EC	pH	T	HCO_3	Na	K	Mg	Ca	Sr	Ba	Mn	Fe	F	Cl	Br	NO_3	PO_4	SO_4	SiO_2	TDS	Al	As	B	Cd	Co	Cr	Cu	Li	Mo	Pb	Se	U	Zn
08ZERT-**174**	8/11/08	11:30	1430	6.2	16	1069	11.3	9.1	63	224	0.75	0.31	0.21	<0.025	<0.05	6.3	0.063	0.72	0.07	9.9	43	60	6	1.4	0.024	0.61	0.5	47	2.8	0.010	0.8	0.09	6	5.4	4.6

4A

						Major Solutes (mg/L)																Trace Solutes (µg/L)												
SAMPLE	DATE	time	EC	pH	T	HCO_3	Na	K	Mg	Ca	Sr	Ba	Mn	Fe	F	Cl	Br	NO_3	PO_4	SO_4	SiO_2	TDS	Al	As	B	Cd	Co	Cr	Cu	Li	Mo	Pb	Se	U	Zn
08ZERT-**106**	7/8/08	10:00	609	6.9	8	398	8.1	5.6	25	86	0.28	0.10	0.31	<0.01	0.11	5.1	0.044	0.19	0.13	7.4	26	39	2	0.8	0.013	0.10	0.6	<0.4	1.1	0.004	0.3	0.02	<2	4.0	3.2

4B

						Major Solutes (mg/L)																Trace Solutes (µg/L)												
SAMPLE	DATE	time	EC	pH	T	HCO_3	Na	K	Mg	Ca	Sr	Ba	Mn	Fe	F	Cl	Br	NO_3	PO_4	SO_4	SiO_2	TDS	Al	As	B	Cd	Co	Cr	Cu	Li	Mo	Pb	Se	U	Zn
08ZERT-**104**	7/7/08	17:40	644	6.9	15	431	9.7	5.6	27	90	0.30	0.10	0.11	0.05	0.17	5.3	0.046	0.10	0.09	7.3	33	46	3	1.0	0.017	0.26	0.8	10	2.4	0.006	1.3	0.08	<4	4.5	2.4
08ZERT-**119**	7/12/08	11:00	624	7.0	9	410	8.2	5.8	25	87	0.28	0.12	1.02	0.05	0.14	5.4	0.044	<0.01	0.03	7.6	31	44	3	0.9	0.019	0.32	1.8	15	1.5	0.006	0.7	0.07	5	4.1	4.2
08ZERT-**126**	7/15/08	9:15	706	6.3	9	468	8.7	6.0	29	99	0.33	0.14	1.2	0.08	0.13	5.4	0.045	<0.01	0.02	7.4	34	47	3	0.9	0.019	0.37	2.0	28	1.6	0.006	0.6	0.06	5	4.4	3.3
08ZERT-**130**	7/17/08	9:30	720	6.3	9	475	9.1	6.1	30	101	0.33	0.15	1.2	0.08	0.11	5.4	0.045	<0.01	0.024	7.5	32	45	3	0.6	0.021	0.30	2.0	7	1.6	0.005	0.5	0.05	3	4.0	3.1
08ZERT-**134**	7/19/08	9:00	848	6.5	10	533	10.3	6.7	35	123	0.41	0.16	0.51	0.030	0.13	5.4	0.050	0.07	0.05	7.7	34	48	3	0.6	0.019	0.18	1.2	3	2.0	0.004	0.6	0.04	2	4.6	2.2
08ZERT-**141**	7/21/08	11:30	882	6.6	15	589	10.3	6.6	37	130	0.42	0.16	0.37	<0.013	0.13	5.5	0.046	0.10	0.05	7.9	33	47	4	0.6	0.022	0.35	0.7	13	2.1	0.006	0.5	0.05	3	4.2	2.5
08ZERT-**143**	7/23/08	11:00	997	6.2	16	708	11.6	7.0	42	143	0.49	0.17	0.28	0.034	0.12	5.4	0.054	0.14	0.05	8.2	37	51	3	0.6	0.018	0.19	0.8	4	2.3	0.006	0.5	0.04	2	4.8	4.4
08ZERT-**148**	7/26/08	10:15	1085	6.4	14	742	12.1	7.6	47	163	0.55	0.19	0.34	0.020	0.11	5.5	0.049	0.20	0.04	8.5	30	45	3	0.7	0.014	0.18	0.8	<0.5	2.0	0.005	0.4	0.04	<3	5.0	2.8
08ZERT-**152**	7/29/08	9:50	941	6.4	14	641	10.7	7.4	41	141	0.48	0.19	1.00	0.11	0.11	5.6	0.054	0.13	0.02	8.2	32	46	2	0.8	0.013	0.19	1.6	<0.5	1.4	0.005	0.4	0.16	<3	4.5	3.0
08ZERT-**159**	8/4/08	10:00	807	6.1	14	528	9.1	7.0	33	115	0.38	0.18	1.44	0.21	0.09	6.1	0.060	0.13	<0.015	8.0	35	49	4	0.7	0.022	0.44	2.5	20	1.7	0.006	0.6	0.06	4	3.8	2.9
08ZERT-**166**	8/7/08	12:15	786	6.2	16	542	9.1	7.0	33	111	0.38	0.17	1.4	0.14	0.09	6.3	0.066	0.21	<0.015	8.0	36	51	3	0.6	0.015	0.23	2.5	5	1.6	0.005	0.5	0.03	3	4.0	6.1
08ZERT-**168**	8/8/08	9:45	794	6.3	15	546	9.1	7.0	33	113	0.38	0.18	1.41	0.18	0.09	6.4	0.068	0.24	<0.015	8.0	35	50	3	0.5	0.019	0.27	2.5	10	1.6	0.006	0.5	0.04	<2	4.0	2.3
08ZERT-**173**	8/11/08	11:05	702	6.3	16	581	9.5	7.0	35	122	0.41	0.17	0.65	0.068	0.11	6.7	0.074	0.66	0.016	8.3	35	51	3	0.5	0.020	0.26	1.2	11	1.8	0.007	0.5	0.04	<2	4.1	2.2
08ZERT-**178**	8/13/08	13:50	727	6.5	24	484	8.5	6.6	29	100	0.35	0.14	0.77	0.089	0.13	7.0	0.076	0.87	0.020	8.2	33	49	3	0.7	0.016	0.22	1.4	5	1.7	0.006	0.6	0.03	4	4.1	2.8

5B

						Major Solutes (mg/L)																Trace Solutes (µg/L)											
SAMPLE	DATE	time	EC	pH	T	HCO_3	Na	K	Mg	Ca	Sr	Ba	Mn	Fe	F	Cl	Br	NO_3	PO_4	SO_4	SiO_2	TDS	Al	As	B	Cd	Co	Cr	Cu	Li	Mo	Pb	Se	U	Zn
08ZERT-**116**	7/11/08	14:45	1257	6.2	9	994	12.7	6.5	66	190	0.67	0.25	0.046	0.19	0.15	5.3	0.051	<0.01	<0.015	8.1	46	60	8	<2	0.026	0.41	1.0	46	2.7	0.011	1.0	0.07	<10	4.7	3.9
08ZERT-**124**	7/14/08	13:15	1287	6.0	9	1174	11.7	6.8	68	201	0.71	0.27	0.14	0.63	0.14	5.4	0.054	0.018	<0.015	8.5	50	64	8	<2	0.028	0.59	2.5	87	2.8	0.013	0.8	0.10	<10	4.9	5.9
08ZERT-**129**	7/15/08	12:30	1264	6.0	10	982	11.3	6.8	64	181	0.63	0.26	0.17	0.93	0.06	5.4	0.053	0.049	<0.015	8.3	47	61	7	<2	0.024	0.56	3.1	76	2.4	0.012	0.7	0.08	<10	4.7	3.6
08ZERT-**133**	7/17/08	12:00	1321	5.9	9	1060	11.2	6.8	70	199	0.71	0.27	0.19	0.72	0.09	5.5	0.052	0.028	<0.015	8.7	41	55	7	0.6	0.025	0.58	2.4	20	2.3	0.010	0.7	0.09	4	5.2	4.2
08ZERT-**137**	7/19/08	13:00	1434	6.0	10	1152	10.9	6.8	70	227	0.83	0.29	0.15	0.06	0.06	5.5	0.056	0.05	0.07	9.1	42	57	5	0.6	0.019	0.31	1.0	8	2.9	0.008	0.9	0.07	3	5.7	3.9
08ZERT-**142**	7/21/08	11:50	1415	6.0	23	1081	10.5	6.6	66	228	0.80	0.28	0.10	<0.025	0.05	5.6	0.051	0.14	0.07	9.5	39	55	7	0.6	0.026	0.55	0.8	27	3.0	0.010	1.0	0.07	4	5.9	5.4
08ZERT-**145**	7/23/08	12:40	1495	5.9	15	1136	11.4	6.9	68	233	0.83	0.29	0.11	0.026	0.10	5.6	0.055	0.32	0.09	10.2	42	58	5	1.1	0.016	0.32	1.1	9	3.5	0.009	0.7	0.07	4	6.2	6.6
08ZERT-**149**	7/26/08	11:00	1285	6.0	15	1023	9.9	6.4	55	213	0.74	0.25	0.058	<0.025	<0.05	5.6	0.048	0.55	0.08	9.4	29	44	4	1.1	<0.015	0.21	<0.5	<1.0	2.9	0.007	<0.75	<0.05	<5	4.6	4.8
08ZERT-**153**	7/29/08	11:15	1111	6.0	17	881	9.2	6.0	46	185	0.62	0.22	0.083	0.10	0.16	5.6	0.052	0.34	0.03	8.5	29	44	3	0.8	<0.012	0.20	0.8	<0.8	1.9	0.007	<0.6	<0.04	<4	4.1	4.4
08ZERT-**162**	8/4/08	13:00	1113	5.9	17	843	9.5	6.5	48	187	0.63	0.24	0.14	0.31	0.13	5.9	0.056	0.50	<0.015	8.5	38	53	5	0.5	0.021	0.54	1.4	40	2.0	0.007	0.7	0.06	5	4.2	2.9
08ZERT-**164**	8/7/08	10:00		6.0		761	9.4	6.5	44	160	0.55	0.21	0.20	0.85	0.15	6.2	0.068	0.68	<0.015	8.5	39	55	4	0.6	0.017	0.27	2.1	8	1.8	0.006	0.5	0.03	3	4.2	3.0
08ZERT-**170**	8/8/08	12:30	1130	6.1	20	832	9.5	6.8	47	176	0.62	0.24	0.23	0.77	0.15	6.4	0.069	0.54	<0.015	8.7	37	53	5	<0.5	0.021	0.41	2.3	12	1.8	0.009	0.7	0.05	<3	4.2	4.3
08ZERT-**175**	8/11/08	12:45	1037	6.1	16	727	8.4	6.0	38	167	0.55	0.21	0.072	0.055	0.11	6.7	0.075	1.5	0.019	9.2	34	52	4	<0.5	0.017	0.35	0.7	14	2.5	0.008	0.6	0.04	<3	4.1	2.8
08ZERT-**179**	8/13/08	15:04	759	6.2	20	506	7.0	5.2	25	114	0.38	0.14	0.033	0.071	0.16	7.0	0.082	1.9	0.018	8.9	29	46	3	0.8	0.013	0.22	0.5	1	2.2	0.006	0.8	0.03	4	3.5	2.9

APPENDIX B

Table B1 *Well log for well 6*

Well 6 Log Date 4/29/09 - 4/30/09						
Core (ft)	**(cm)**	**% recovery**	**Depth (cm)**	**Notes**	**BTEX**	**Description**
0-3.5'	107	60%	0-5cm			grass and air
			5-30cm			dark brown, clay rich, plastic soil with roots througout. Slightly fizzes with HCl
				11-15cm		large rock most likely broken by geoprobe
			30-39cm			plastic clay grading from dk brown to lt brown indicating a gradation into caliche
			39-57cm		46-48.5cm	10YR 5/4. Caliche zone. Highly reactive with HCl, very fine grained and plastic with some roots. Few larger, rounded grains between 1-3cm.
			57-64cm			Sandy gravels (with some caliche smearing on kevlar sleeve).
3.5-8'	137	55%	0-15cm	11-15cm		Slough? with a large grain cored through by the geoprobe at 11-15cm.
			15-76cm	30cm	54-58cm	10YR 3/3 dark brown. Coarse sandy gravel, possibly higher percentage of gravels than other cores. Grains as large as 4cm. Gravels appear to have been rounded then broken, possible geoprobe damage? Saturated below 30cm. Lightly fizzes with acid throug
8-10'	61.0	67%	0-41cm		33-37cm	10YR 3/3 dark brown. Coarse sandy gravel, few fines. Grains up to 4cm, possibly damaged by geoprobe. Some plastic from a broken core catcher is present. Few orange clay streaks near 37cm.

APPENDIX C

Estimation of the Solubility Product of Fougerite

Over the past twenty years, considerable study has been devoted to the characterization of metastable minerals that form in soil zones at or near the water table, and where the redox state is affected by decomposition of organic matter derived from vegetative cover. In particular, much attention has been paid to the formation of so called ”green rusts”, which consist of stacked positively charged tri-octahedral sheets of ferrous hydroxide in which some of the Fe(II) has been oxidized to Fe(III). The octahedral sheets are separated by interlayers containing water and charge-balancing anions (see Genin et al., 2006, and references cited therein). At the time of their initial characterization (Bernal et al., 1959; Dasgupta and Mackay, 1959), it was found that green rusts could be characterized by two distinct structures; (1) a rhombohedral form designated as GR-I, which contained simple charge-balancing anions such as OH^- or Cl^-, or planar oxy-anionic charge balancing species such as HCO_3^- and/or CO_3^{-2}, (2) a hexagonal form containing large oxy-anionic species such as SO_4^{-2} and SeO_4^{-2}.

Earlier work concluded that green rusts occupy a stability field in Eh-pH space defined by neutral to weakly acid pH and moderately reducing (anoxic) conditions (Refait and Genin, 1993; Drissi et al., 1995; Genin et al., 1996, 1998; Ruby et al., 2006). Other minerals that might also be associated with green rusts, depending on the concentration of Fe(T) and SO_4^{-2} in the system, and fluctuations in oxidations state include hydroxy-magnetite or magnetite (Olowe and Genin, 1991), schwertmannite and ferrihydrite (Majzlan et al., 2004), these latter phases principally occupying stability fields at higher Eh, and where the phase boundary between schwertmannite and ferrihydrite falls within a pH range close to 7.0. Ruby et al. (2006) also noted that the initial oxidation of green rust causes a characteristic color change from blue-green to orange-yellow while preserving the original tri-octahedral structure. It is noteworthy that some of the recovered fine material from cores taken at the ZERT site also contained unspecified iron oxides characterized as “powdery orange blebs” (Thordsen, 2009), lending credence to the belief that green rust may actually form in shallow groundwater at the ZERT site. Green rust decomposes exceedingly rapidly upon exposure to air, and therefore it would not be expected to survive coring and recovery at the ZERT site unless extreme precautions had been taken. Elsewhere (Schwertmann and Fechter, 1994) has observed that green rust eventually transforms to lepidocrocite under oxidizing conditions. However, whether or not green rust transforms to ferrihydrite as an intermediate step before recrystallization to lepidocrocite is not clear from the literature, although the following thermodynamic analysis suggests that this could be the case at the ZERT site.

Characterization of green rusts in a gleysol horizon at Fougeres in Normandy, France (Trolard et al., 1996; Abdelmoula et al., 1998) lead to its recognition as a mineral species; fougerite, and furthermore revealed that the tri-octahedral sheets are in fact a mixture of Fe(II), Fe(III) and Mg(II). Bourrie et al. (2004) created a solid solution model of the hydroxide form of fougerite in which Fe(II)-Mg(II) substitution was treated as an ideal solution, whereas Fe(II)-Fe(III) substitution was treated as a regular solution with the constraint that adjacent Fe(III) sites are prohibited. Information on the thermodynamic properties of the end member binary solid solutions in the three-component system was obtained from prior solubility and calorimetric studies reported in the literature. This model was subsequently expanded by Feder et al. (2005) to consider anion occupancies by (HCO_3^- + CO_3^{-2}), Cl^- and SO_4^{-2} in place of OH^- in the interlayer positions, without, however, taking into

account interlayer ion exchange. Recently, Christiansen et al. (2009) found that at least some green rusts also contain interlayer cations in addition to anions. Therefore, a complete characterization of green rust thermodynamic properties must await further study. Feder et al. (2005) also examined the possibility that these forms of fougerite might achieve thermodynamic equilibrium in the saturated soil zone at Fougeres. They found that saturation was achieved with respect to certain carbonate and sulfate fougerite compositions, but that chloride forms would always be undersaturated, whereas the hydroxide forms would always be grossly supersaturated.

A preliminary comparison of groundwater compositions at Fougeres (Feder et al., 2005) with those at the ZERT site indicated that although temperature and pH were comparable, Mg^{+2}, Fe(T), Cl^{-} and SO_4^{-2} concentrations were lower, and the alkalinity (as HCO_3^{-}) was higher. These observations suggest that a carbonate form of fougerite might be stable at the ZERT site.

The solubility products of all forms of fougerite were calculated assuming the stoichiometry to be $([2/9Fe^{II}(OH)_2.1/3Fe^{III}(OH)_2.4/9Mg(OH)_2]^{+1/3}[1/3A]^{-1/3})$, where A = OH-, Cl-, $(2/3HCO_3^{-}.1/6CO_3^{-2})$, or $1/2SO_4^{-2}$. The solubility products were determined by direct comparison with the reported field saturation states at Fougeres, rather than by calculating the solubility products from the reported thermodynamic data given by Bourrie et al. (2003) and Feder et al. (2005), as the reference states used in their derivations differed from those we currently use in EQ3/6. Incorporation of the solubility products of the fougerite forms in the EQ3/6 thermodynamic database and testing using the baseline groundwater composition before CO_2 injection indicated that the carbonate form of fougerite could be stable at the ZERT site, depending on the oxidation state of the system.

APPENDIX D

The Saturation State of Redox-Sensitive Chromium, Copper, and Selenium Minerals as Function of pe.

In this appendix, we pick up on Section 5.2.2, which considers potential solid phase redox buffers that might influence the redox state, or be influenced by the redox state, in the coexisting groundwater in a shallow unconfined aquifer such as that represented by the ZERT site. We start with a discussion of the stabilities of a suite of chromium oxide minerals, most of which are spinels.

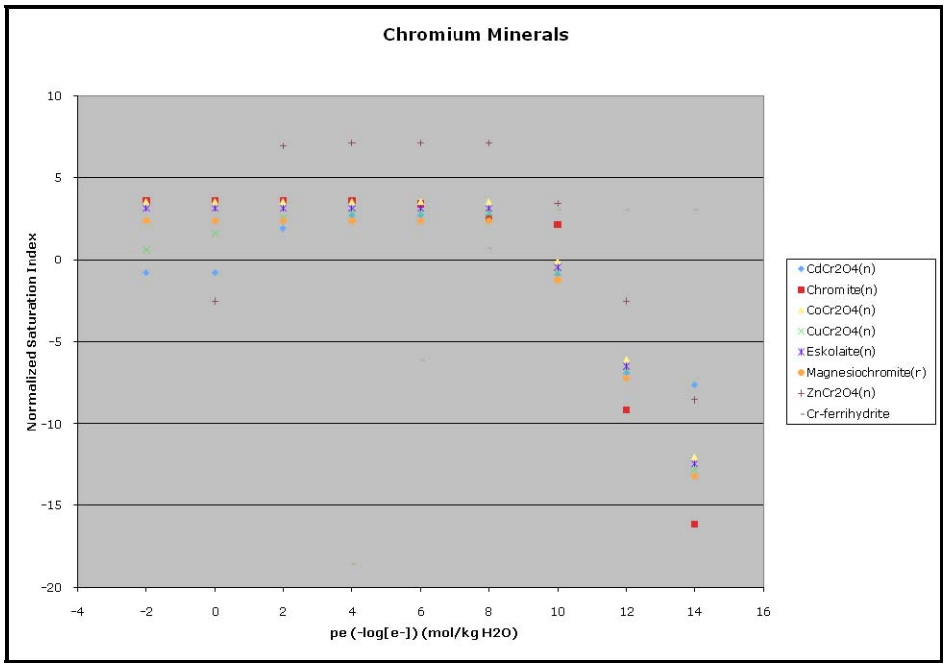

Figure D.1. *Normalized saturation indices of chromite, magnesiochromite, and the chromium spinels of Cd, Co, Cu and Zn, Eskolaite and Cr-ferrihydrite, plotted as a function of pe.*

The phase behavior of these chromium oxide minerals as a function of pe is displayed in Figure D.1. The saturation indices of chromium spinels, MCr_2O_4, where M = Mg(II), Fe(II), Cu(II), Co(II) and Zn(II), and eskolaite (Cr_2O_3) varies systematically with pe, and at intermediate pe values, i.e., pe +2 - +8, are, with the exception of the Zn spinel, closely correlated. The phase boundary between Cr-ferrihydrite ($Fe_4(CrO_4)(OH)_{10}$), and chromite ($FeCr_2O_4$) occurs at pe ≈ +8.7 at SI ≈ +2, where the pe value is similar to that between fougerite-CO_3 and $Fe(OH)_3$. The significance of this correlation is not clear. It is probable that Cr(III) substitutes as a minor component in these phases at the ZERT site. However, this substitution is constrained at higher redox potentials by the oxidation of Cr(III) to Cr(VI) in solution with concomitant destabilization of chromium spinels, as is evident in the figure. The close correlation between the saturation indices of the chromium spinels between pe +2 - +8, invites speculation that the concentrations of Mg(II), Fe(II), Cu(II), and Co(II) in solution might be determined by solid solution equilibrium with respect to some common iron, or Fe(II)/Mg(II) oxide mineral in the system at the ZERT site. However, the principal component analysis is equivocal on this point. Further study of the behavior of Cr in shallow

groundwater systems is certainly merited, and the thermodynamic properties of the participating minerals should be verified.

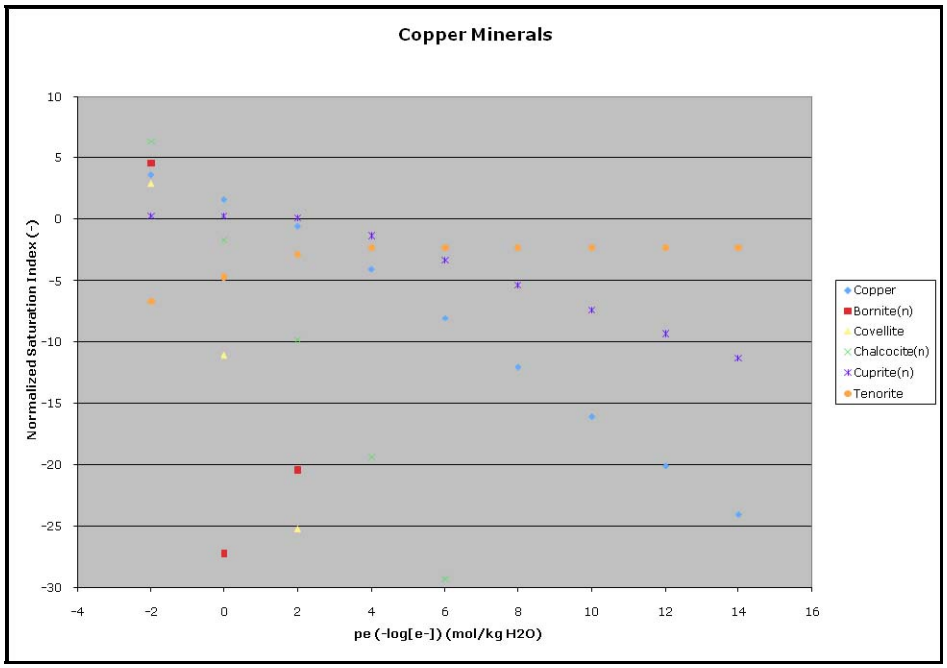

Figure D.2. *Normalized saturation indices of copper, bornite, covellite, chalcocite, cuprite and tenorite, plotted as a function of pe.*

The normalized saturation indices of various copper minerals as a function of pe are plotted in Figure D.2. The redox behavior of copper is of interest because phase relations between tenorite (CuO) and cuprite (Cu_2O) marks the redox transition between the Cu(II) and Cu(I) oxidation states, which occurs under moderately reducing conditions. The concentration of Cu in solution at the ZERT site is insufficient to cause saturation with respect to tenorite. However, both native copper and cuprite would achieve saturation at pe ≈ +1.5, whereas the chalcocite and cuprite phase boundary is intersected at pe ≈ -0.5.

It is interesting to note that at pe ≤ +2, cuprite remains close to saturation, i.e., SI ≈ 0. A possible explanation is that the redox pair Cu^{+2}/Cu^{+} forms one of the cluster of redox pairs in local partial equilibrium with respect to organic matter, as observed by Washington et al. (2004). However, the average crustal abundance of Cu is such that this redox pair is unlikely to exert any redox control over the system. Similar control by organic matter on the SO_4^{-2}/HS^{-} redox pair might be responsible for saturation with respect to chalcocite.

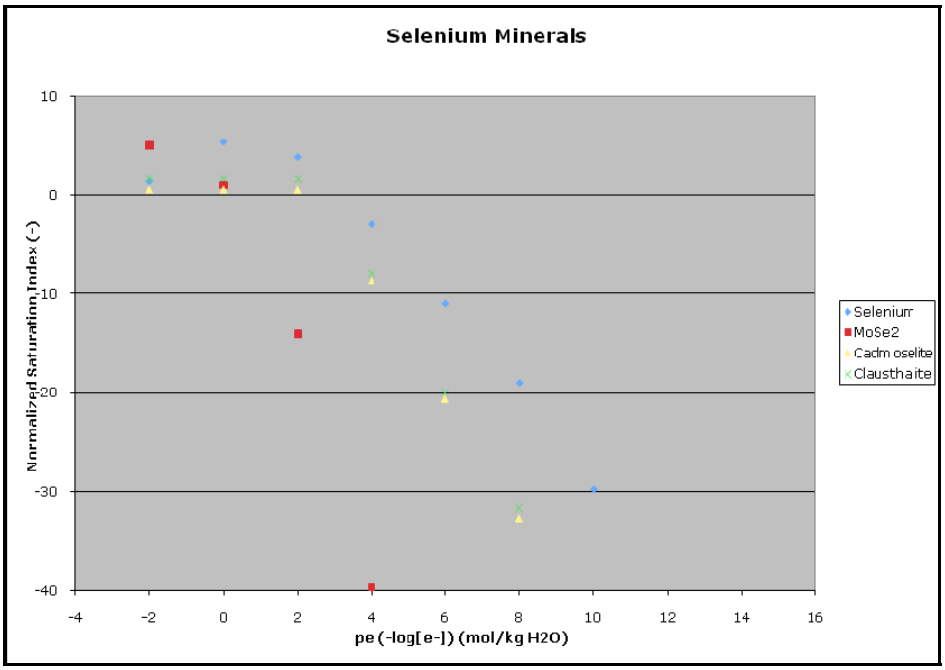

Figure D.3. *Normalized saturation indices of selenium, molybdenum selenide, cadmoselite and clausthalite, plotted as a function of pe.*

Figure D.3 illustrates the behavior of the saturation indices of selenium minerals with variation in pe. Saturation is achieved with respect to native selenium at pe ≈ +2.7, and with respect to cadmoselite and clausthalite at about +2.4. $MoSe_2$, a phase that has not been identified in nature, would saturate at pe ≈ 0. Given that the participating trace elements Cd, Mo, Pb and Se are all present in exceedingly low concentrations, none of the saturating phases are likely to exert a significant redox buffering capacity on the system. However, as noted with respect to the potential saturation of cuprite and chalcocite in the copper system, the concentrations of Cd and Pb could be controlled by saturation with respect to their selenides or sulfides as a result of reduction of Se(IV) to Se(0) and Se(-II), and S(VI) to S(-II) by organic matter.

Both Cu and Se are trace element with very low natural crustal abundance, and it is therefore unlikely that either play a significant role in controlling the oxidation state of the system. However, the impact of organic matter in exercising local partial equilibrium control over some redox pairs cannot be discounted, especially in relation to Se, S and possibly U. This would imply that, although the redox state of MSU-ZERT groundwaters are controlled primarily by iron minerals and their interaction with infiltrating nitrate, organic matter could also be playing a role with respect to some species. In other words, the MSU-ZERT groundwaters are behaving in a manner similar to shallow groundwaters investigated by Washington et al. (2004) with formation of two redox cluster in local partial equilibrium, one dominated by nitrate and the other dominated by organic matter.

An intriguing possibility, which merits further study, is that a redox potential gradient exists at the site, with more reducing conditions at greater depth, where transient ingress of infiltrating oxidizing groundwater is less likely to have an impact. The more reducing conditions induce local saturation with respect to Cu(I) mineral such as cuprite or chalcocite, and control the activity of copper in

solution, which is established in the overlying oxidizing horizons through diffusive transport. Similar behavior is observed with respect to the selenides cadmoselite (CdSe) and clausthalite (PbSe) with respect to selenium minerals. The foregoing statement is highly speculative and requires further study before it can be advanced as a serious hypothesis.